
Proceedings, 5th Chaotic Modeling and Simulation International Conference, 12 – 15 June 2012, Athens Greece

Ideal Chaotic Pattern Recognition Using the Modified Adachi Neural Network

Ke Qin[1] and B. J. Oommen[2,3]

[1] University of Electronic Science & Technology of China, Chengdu, China. 611731
(E-mail: thinker_qk@hotmail.com)
[2] Carleton University, Ottawa, ON, Canada. K1S 5B6
[3] University of Agder, Postboks 509, 4898 Grimstad, Norway.
(E-mail: oommen@scs.carleton.ca)

Abstract. The benchmark of a chaotic Pattern Recognition (PR) system is the following: First of all, one must be able to train the system with a set of "training" patterns. Subsequently, as long as there is no testing pattern, the system must be chaotic. However, if the system is, thereafter, presented with an unknown testing pattern, the behavior must ideally be as follows. If the testing pattern is not one of the trained patterns, the system must continue to be chaotic. As opposed to this, if the testing pattern is truly one of the trained patterns (or a noisy version of a trained pattern), the system must switch to being *periodic*, with the specific trained pattern appearing periodically at the output. This is truly an ambitious goal, with the requirement of switching from chaos to periodicity being the most demanding. The Adachi Neural Network (AdNN) [1–5] has properties which are *pseudo*-chaotic, but it also possesses *limited* PR characteristics. As opposed to this, the Modified Adachi Neural Network (M-AdNN) proposed by Calitoiu *et al* [7], is a fascinating NN which has been shown to possess the required periodicity property desirable for PR applications. In this paper, we shall tune the parameters of the M-AdNN for its weights, steepness and external inputs, to yield a new NN, which we shall refer to as the Ideal-M-AdNN. Using a rigorous Lyapunov analysis, we shall analyze the chaotic properties of the Ideal-M-AdNN, and demonstrate its chaotic characteristics. Thereafter, we shall verify that the system is also truly chaotic for untrained patterns. But most importantly, we demonstrate that it is able to *switch to being periodic* whenever it encounters patterns with which it was trained. Apart from being quite fascinating, as far as we know, the theoretical and experimental results presented here are both unreported and novel. Indeed, we are not aware of any NN that possesses these properties!

Keywords: Chaotic Neural Networks, Chaotic Pattern Recognition.

1 Introduction

Pattern Recognition (PR) has numerous well-established sub-areas such as statistical, syntactic, structural and neural. The field of *Chaotic* PR is, however, relatively new and is founded on the principles of chaos theory. It is also

based on a distinct phenomenon, namely that of *switching* from *chaos* to *periodicity*. Indeed, Freeman's clinical work has clearly demonstrated that the brain, at the individual neural level and at the global level, possesses chaotic properties. He showed that the quiescent state of the brain is chaos. However, during perception, when attention is focused on any sensory stimulus, the brain activity becomes more periodic [10].

If the brain is capable of displaying both chaotic and periodic behavior, the premise of this paper is that it is expedient to devise artificial Neural Network (NN) systems that can display these properties too. Thus, the primary goal of *chaotic* PR is to develop a system which mimics the brain to achieve chaos and PR, and to consequently develop a new PR paradigm.

Historically, the initial and pioneering results concerning these CNNs were presented in [1–5]. Subsequently, the author of [11] proposed two methods of controlling chaos by introducing a small perturbation in continuous time, i.e., by invoking a combined feedback with the use of a specially-designed external oscillator or by a delayed self-controlling feedback without the use of any external force. The reason for the introduction of this perturbation was to stabilize the unstable periodic orbit of the chaotic system. Thereafter, motivated by the work of Adachi, Aihara and Pyragas, various types of CNNs have been proposed to solve a number of optimization problems (such as the Traveling Salesman Problem, (TSP)), or to obtain Associative Memory (AM) and/or PR properties. An interesting step in this regard was the work in [15], where the authors utilized the delayed feedback and the Ikeda map to design a CNN to mimic the biological phenomena observed by Freeman [10].

More recently, based on the AdNN, Calitoiu and his co-authors made some interesting modifications to the basic network connections so as to obtain PR properties and "blurring". In [8], they showed that by binding the state variables to those associated with *certain* states, one could obtain PR phenomena. However, by modifying the manner in which the state variables were bound, they designed a newly-created machine, the so-called Mb-AdNN, which was also capable of justifying "blurring" from a NN perspective. While all of the above are both novel and interesting, since most of these CNNs are *completely*-connected graphs, the computational burden is rather intensive. Aiming to reduce the computational cost, in our previous paper [12], we proposed a mechanism (the Linearized AdNN (L-AdNN)) to reduce the computational load of the AdNN. To complete this historical overview, we mention that in [12], we showed that the AdNN goes through a spectrum of characteristics (i.e., AM, *quasi*-chaotic, and PR) as one of its crucial parameters, α, changes. It can even recognize masked or occluded patterns!

Although it was initially claimed that the AdNN and M-AdNN possessed "pure" (i.e., periodic) PR properties, in actuality, this claim is not as precise as the authors claimed – the output can be periodic for both trained and untrained input patterns – which is where our present paper is relevant. The primary aim of this paper is to show that the M-AdNN, when tuned

appropriately, is capable of demonstrating ideal PR capabilities. Thus, the primary contributions of this paper are:

1. We formalize the requirements of a PR system which is founded on the theory of chaotic NNs.
2. We enhance the M-AdNN to yield the Ideal-M-AdNN, so that it does, indeed, possess *Chaotic* PR properties.
3. We show that the Ideal-M-AdNN does switch from chaos to periodicity when it encounters a trained pattern, but that it is truly chaotic for all other input patterns.
4. We present results concerning the stability of the network and its transient and dynamic retrieval characteristics. This analysis is achieved using eigenvalue considerations, and the Lyapunov exponents.
5. We provide explicit experimental results to justify our claims.

In the interest of brevity and space, the details of the theoretical results reported here are not included. They are found in the unabridged version of the paper [13].

2 The Ideal-M-AdNN

The goal of the field of Chaotic PR systems can be expressed as follows: We do not intend a chaotic PR system to report the identity of a testing pattern with a class "proclamation" as in a traditional PR system. Rather, what we want to achieve for a the chaotic PR system are the following phenomena:

- The system must yield a strong *periodic* signal when a trained pattern, which is to be recognized, is presented.
- Further, between two consecutive recognized patterns, none of the trained patterns must be recalled.
- On the other hand, and most importantly, if an untrained pattern is presented, the system must give a chaotic signal.

Calitoiu *et al* were the first researchers who recorded the potential of chaotic NNs to achieve PR. But unfortunately, their model, as presented in [7], named the M-AdNN, was not capable of demonstrating *all* the PR properties mentioned above.

The topology of the Ideal-M-AdNN is exactly the same as that of the M-AdNN. Structurally, it is also composed of N neurons, topologically arranged as a completely connected graph. Each neuron has two internal states $\eta_i(t)$ and $\xi_i(t)$, and an output $x_i(t)$. Just like the M-AdNN, the Present-State/Next-State equations of the Ideal-M-AdNN are defined in terms of only a *single* global neuron (and its corresponding two global states), which, in turn, is used for the state updating criterion for *all* the neurons. Thus,

$$\eta_i(t+1) = k_f \eta_m(t) + \sum_{j=1}^{N} w_{ij} x_j(t),$$

$$\xi_i(t+1) = k_r \xi_m(t) - \alpha x_i(t) + a_i,$$

$$x_i(t+1) = f(\eta_i(t+1) + \xi_i(t+1)),$$

where m is the index of this so-called "global" neuron.

We shall now concentrate on the differences between the two models, which are the parameters: $\{w_{ij}\}$, ε and a_i, which were previously set arbitrarily. Rather, we shall address the issue of how these parameters must be assigned their respective values so as to yield pure *Chaotic* PR properties.

2.1 The Weights of The Ideal-M-AdNN

The M-AdNN uses a form of the Hebbian Rule to determine the weights of the connections in the network. This rule is defined by the following equation:

$$w_{ij} = \frac{1}{p} \sum_{s=1}^{p} P_i^s P_j^s, \tag{1}$$

where $\{P\}$ are the training patterns, P_i^s denotes the i^{th} neuron of the s^{th} pattern P^s, and where p is the number of known training patterns. This rule is founded on two fundamental premises, namely:

1. Each element of the learning vectors should be either 1 or -1;
2. Any pair of learning vectors, P and Q, must be orthogonal.

In this regard, we note that:

1. In [7], the elements of the corresponding learning vectors are restricted to be either 0 and 1, which implies that the connection between any two neurons, say, A and B, will be increased only if they are both positive. Further, the connection weights are not changed otherwise.
2. The formal rationale for orthogonality is explained in [13]. Although it is not so stringent, when the number of neurons is much larger than the number of patterns, and the learning vectors are randomly chosen from a large sample set, the probability of having the learning vectors to be orthogonal is very high. Consequently, generally speaking, the Hebbian rule is true, albeit in a probabilistic sense.

Based on the above observations, we conclude that for the M-AdNN, we should not use the Hebbian rule as dictated by the form given in Equation (1), since the data sets used by both Adachi *et al* and Calitoiu *et al* are defined on $\{0,1\}^N$, and the output is further restricted to be in $[0,1]$ by virtue of the logistic function. In fact, this is why Adachi and Aihara computed the weights by scaling all the patterns to be in -1 and 1 using the formula given by Equation (2) instead of Equation (1):

$$w_{ij} = \frac{1}{p} \sum_{s=1}^{p} (2P_i^s - 1)(2P_j^s - 1). \tag{2}$$

By virtue of this argument, in this paper, we advocate the use of this formula, i.e., Equation (2), to determine the connection weights of the network.

It is pertinent to mention that since the patterns $\{P\}$ are scaled to be in the range between -1 and 1, it *does* change the corresponding property of orthogonality. This is clearly demonstrated in [13], but omitted here in the interest of space.

2.2 The Steepness, Refractory and Stimulus Parameters

Significance of ε for the AdNN: The next issue that we need to consider concerns the value of the steepness parameter, ε, of the output function. As explained earlier, we see that the output function is defined by the Logistic function $f(x) = \frac{1}{1+e^{-x/\varepsilon}}$, which is a typical sigmoid function.

One can see that ε controls the steepness of the output. If $\varepsilon = 0.01$, then $f(x)$ is a normal sigmoid function. If ε is two small, for example, 0.0001, the Logistic function almost degrades to become a unit step function, as shown in [13]. The question is one of knowing how to set the "optimal" value for ε.

To provide a rationale for determining the best value of ε, we concentrate on the Adachi's neural model [2] defined by:

$$y(t+1) = ky(t) - \alpha f(y(t)) + a, \tag{3}$$

where $f(\cdot)$ is a continuous differentiable function, which as per Adachi *et al* [2], is the Logistic function.

The properties of Equation (3) greatly depend on the parameters k, α, a and $f(\cdot)$. In order to obtain the full spectrum of the properties represented by Equation (3), it is beneficial for us to first consider $f(\cdot)$ in terms of a unit step function, and to work with a fixed point analysis. In [13] this analysis has been in great detail for the case of: (a) a single fixed point, (b) period-2 fixed points, and (c) period-n orbits. By a lengthy argument, we have explained *how* the parameter ε should be set.

In our experiment, indeed, if the parameters are set to be $\alpha = 1$ and $k = 0.5$, the "tipping point" for ε is $1/6 \approx 0.1667$. As shown in [13] if $\varepsilon = 0.18 > 0.1667$, all of the fixed points are stable. Otherwise, if $\varepsilon = 0.15 < 0.1667$, there exist period-doubling bifurcations As ε is further decreased, one can observe chaotic windows.

We conclude this section by emphasizing that ε cannot be too small, for if it were, the Adachi neural model would degrade to the Nagumo-Sato model, which does not demonstrate any chaotic behavior. This is also clearly demonstrated in the figures shown in [13].

Our arguments show that the value of ε as set in [8] to be $\varepsilon = 0.00015$, is not appropriate. Rather, to develop the Ideal-M-AdNN, , we have opted to use a value of ε which is *two* orders of magnitude larger, i.e., $\varepsilon = 0.015$.

3 Lyapunov Exponents Analysis of the Ideal-M-AdNN

We shall do a Lyapunov Exponents (LE) analysis of the Ideal-M-AdNN, both from the perspective of a *single* neuron and of the network in its entirety.

As is well known, the LEs describe the behavior of a dynamical system. There are many ways, both numerically and analytically, to compute the LEs of a dynamical system. Generally, for systems with a small dimension, the best way is to analytically compute it using its formal definition. As opposed to this, for systems with a high dimension, it is usually not easy to obtain the entire LE spectrum in an analytic manner. In this case, we have several other alternatives to judge whether a system is chaotic. One of these is to merely determine the largest LE (instead of computing the entire spectrum) since the existence of a single positive LE indicates chaotic behavior. Algorithmically, the basic idea is to follow two orbits that are close to each other, and to calculate their average logarithmic rate of separation [9,16].

In practice, this algorithm is both simple and convenient if we have the right to access the equations that govern the system. Furthermore, if it is easy to obtain the partial derivatives of the system, we can also calculate the LE spectrum by QR decomposition [9,14,16].

The unabridged version of the paper [13] also contains a detailed analysis for obtaining the LE spectrum using the QR decomposition. It is omitted here due to the space limitations.

We have also, in [13], undertaken a Lyapunov Analysis of the Ideal-M-AdNN. Indeed, it can be easily proven that a single neuron is chaotic when the parameters are properly set.

Also, for the Ideal-M-AdNN (i.e., the entire network), we can show [13] that the Lyapunov Exponents are: $\lambda_1 = \cdots \lambda_{N-1} = -\infty$, $\lambda_N = \log N + \log k_f > 0$, $\lambda_{N+1} = \cdots \lambda_{2N-1} = -\infty$, $\lambda_{2N} = \log N + \log k_r > 0$. In conclusion, the Ideal-M-AdNN has two positive LEs, which indicates that the network is truly a chaotic network!

It's very interesting to compare this result with the one presented for the AdNN. Indeed, as we can see from [6], the AdNN has two different LEs: $\log k_f$ and $\log k_r$. The difference is that by binding the states of all the neurons to a single "*global*" neuron, we force the Ideal-M-AdNN to have two positive LEs. The LE spectrum of the two networks are compared in [13].

4 Chaotic and PR Properties of the Ideal-M-AdNN

We shall now report the properties of the Ideal-M-AdNN. These properties have been gleaned as a result of examining the Hamming distance between the input pattern and the patterns that appear at the output. In this regard, we mention that the experiments were conducted using two data sets, namely the figures used by Adachi *et al* given in Figure 1 (a), and the numeral data sets used by Calitoiu *et al* [7,8] give in Figure 1 (b). In both the cases, the

patterns were described by 10×10 pixel images, and the networks thus had 100 neurons.

Before we proceed, we remark that although the experiments were conducted for a variety of scenarios, in the interest of brevity, we present here only a few typical sets of results – essentially, to catalogue the overall conclusions of the investigation.

(a) (b)

Fig. 1. The 10×10 patterns used by Adachi *et al* (on the left) and Calitoiu *et al* (on the right). In both figures (a) and (b), the first four patterns are used to train the network. The fifth patterns are obtained from the corresponding fourth patterns by including 15% noise in (a) and (b) respectively. In each case, the sixth patterns are the untrained patterns.

We discuss the properties of the Ideal-M-AdNN in three different settings. In all of the three cases, the parameters were set to be $k_f = 0.2$, $k_r = 0.9$, and $\varepsilon = 0.015$, and all the internal states, $\eta_i(0)$ and $\xi_i(0)$, start from 0.

AM Properties: We now examine whether the Ideal-M-AdNN possesses any AM-related properties for certain scenarios, i.e., if we fix the external input $a_i = 2$ for all neurons. The observation that we report is that during the first 1,000 iterations (due to the limitations of the file size, we present here only the first 36 images), the network only repeats black and white images. This can be seen in Figure 2. The reason for this phenomenon is explained in detail in [13].

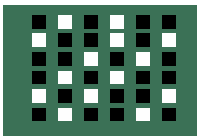

Fig. 2. The visualization of the output of the Ideal-M-AdNN under the external input $a_i = 2$. We see that the output switches between images which are entirely only black or only white.

PR Properties: The PR properties of the Ideal-M-AdNN are the main concern of this paper. As illustrated in Section 2, the goal of a chaotic PR system is the following: The system should respond periodically to trained input patterns, while it should respond chaotically (with chaotic outputs) to untrained input patterns. We now confirm that the Ideal-M-AdNN does, indeed, possess such phenomena. We present an in-depth report of the PR properties of the Ideal-M-AdNN's by using a Hamming distance-based analysis. The parameters that we used were: $k_f = 0.2$, $k_r = 0.9$, $\varepsilon = 0.015$ and

$a_i = 2 + 6x_i$. The PR-related results of the Ideal-M-AdNN are reported for the three scenarios, i.e., for trained inputs, for noisy inputs, and for untrained (unknown) inputs respectively.

1. The external input of the network corresponds to a known pattern, P4. To report the results for this scenario, we request the reader to observe Figure 3 (a), where we can find that P4 is retrieved periodically as a response to the input pattern. This occurs 391 times in the first 500 iterations. On the other hand, the other three patterns never appear in the output sequence. The phase diagrams of the internal states that correspond to Figure 3 (a) are shown in [13], whence we verify that the periodicity is 14, because all the phase plots have exactly 14 points.

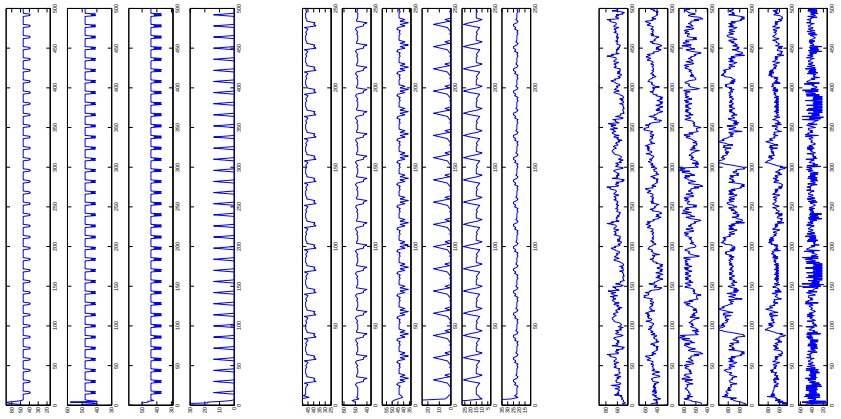

(a) (b) (c)

Fig. 3. PR properties: The Hamming distance between the output and the trained patterns. The input was the pattern P4, P5 and P6 in (a), (b) and (c) respectively. Note that P4 appears periodically in Case (a). Also, note that P4 (not P5) appears periodically in Case (b). Finally, note that *none* of the trained patterns appear at the output in Case (c).

2. The external input of the network corresponds to a noisy pattern, in this case P5, which is a noisy version of P4.
   Even when the external stimulus is a garbled version of a known pattern (in this case P5 which contains 15% noise), it is interesting to see that *only* the original pattern P4 is recalled periodically. In contrast, the others three known patterns are *never* recalled. This phenomenon can be seen from the Figure 3 (b). By comparing Figures 3 (a) and (b), we can draw the conclusion that the Ideal-M-AdNN can achieve chaotic PR even in the presence of noise and distortion. As in the previous case, the phase diagrams of the internal states that correspond to Figure 3 (a) are shown in [13], whence we again verify that the periodicity is 14, because

all the phase plots have exactly 14 points. Indeed, even if the external stimulus contains some noise, the Ideal-M-AdNN is still able to recognize it correctly, by resonating periodically!

3. The external input corresponds to an unknown pattern, P6.
   In this case we investigate whether the Ideal-M-AdNN is capable of distinguishing between known and unknown patterns. Thus, we attempt to stimulate the network with a completely unknown pattern. In our experiments, we used the pattern P6 of Figure 1 (a) initially used by Adachi *et al.* From Figure 3 (c) we see that neither those known patterns nor the presented unknown pattern appear at the output. As in the previous two cases, the phase diagrams of the internal states that correspond to Figure 3 (c) are shown in [13], whence, the lack of periodicity can be observed since the plots themselves are dense.
   In other words, the Ideal-M-AdNN responds intelligently to the various inputs with correspondingly different outputs, each resonating with the input that excites it – which is the crucial golden hallmark characteristic of a *Chaotic* PR system. Indeed, the switch between "order" (resonance) and "disorder" (chaos) seems to be consistent with Freeman's biological results – which, we believe, is quite fascinating!

5 Conclusions

In this paper we have concentrated on the field of Chaotic Pattern Recognition (PR), which is a relatively new sub-field of PR. Such systems, which have only recently been investigated, demonstrate chaotic behavior under normal conditions, and "resonate" (i.e., by presenting at the output a specific pattern frequently) when it is presented with a pattern that it is trained with. This ambitious goal, with the requirement of switching from chaos to periodicity is, indeed, most demanding, and has been achieved by the design of the so-called Ideal-M-AdNN.

Using a rigorous Lyapunov analysis, we have shown the chaotic properties of the Ideal-M-AdNN, and demonstrated its chaotic characteristics. We have also verified that the system is truly chaotic for untrained patterns. But most importantly, we have shown that it is able to *switch to being periodic* whenever it encounters patterns with which it was trained (or noisy versions of the latter).

Apart from being quite fascinating, as far as we know, the theoretical and experimental results presented here are both unreported and novel.

6 Acknowledgements

The work of this paper was supported by the Science Ministry of Sichuan Province of China (2011HH0037), and NSERC, the Natural Sciences and Engineering Research Council of Canada.

References

1. K. Adachi, M. Aihara and M. Kotani. An analysis of associative dynamics in a chaotic neural network with external stimulation. In *Proceedings of the 1993 International Joint Conference on Neural Networks, Nagoya, Japan*, volume 1, pages 409–412, 1993.
2. M. Adachi and K. Aihara. Associative dynamics in a chaotic neural network. *Neural Networks*, 10(1):83–98, 1997.
3. M. Adachi and K. Aihara. Characteristics of associative chaotic neural networks with weighted pattern storage-a pattern is stored stronger than others. In *Proceedings Of The 6th International Conference On Neural Information, Perth Australia*, volume 3, pages 1028–1032, 1999.
4. M. Adachi, K. Aihara, and M. Kotani. Pattern dynamics of chaotic neural networks with nearest-neighbor couplings. In *Proceedings of the 1991 IEEE International Sympoisum on Circuits and Systems, Westin Stanford and Westin Plaza, Singapore*, volume 2, pages 1180–1183, 1991.
5. K. Aihara, T. Takabe, and M. Toyoda. Chaotic neural networks. *Physics Letters A*, 144(6-7):333–340, 1990.
6. M. Adachi and K. Aihara. An analysis on instantaneous stability of an associative chaotic neural network. *International Journal of Bifurcation and Chaos*, 9(11):2157–2163, 1999.
7. D. Calitoiu, B. J. Oommen, and D. Nussbaum. Periodicity and stability issues of a chaotic pattern recognition neural network. *Pattern Analysis and Applications*, 10(3):175–188, 2007.
8. D. Calitoiu, B. J. Oommen, and D. Nussbaum. Desynchronzing of chaotic pattern recognition neural network to model inaccurate parception. *IEEE Transaction on Systems, Man, and Cybernetics-part B:Cybernetics*, 37(3):692–704, 2007.
9. J. P. Eckmann and D. Rulle. Ergodic theory of chaos and strange attractors. *Reviews of Modern Physics*, 57(3):617–656, 1985.
10. W. J. Freeman. Tutorial on neurobiology: from single neurons to brain chaos. *International Journal of Bifurcation and Chaos in Applied Sciences and Engineering*, 2:451–482, 1992.
11. K. Pyragas. Continuous control of chaos by self-controlling feedback. *Physics Letters A*, 170(6):421–428, 1992.
12. K. Qin and B. J. Oommen. Chaotic pattern recognition: The spectrum of properties of the Adachi Neural Network. *Lecuture Notes in Computer Science*, 5342:540–550, 2008.
13. K. Qin and B. J. Oommen. *Ideal* Chaotic pattern recognition is achievable: The Ideal-M-AdNN - Its design and properties. *In Preparation*.
14. M. Sandri. Numerical calculation of Lyapunov exponents. *The Mathematica Journal*, pages 78–84, 1996.
15. A. P. Tsui and A. J. Jones. Periodic response to external stimulation of a chaotic neural network with delayed feedback. *International Journal of Bifurcation and Chaos*, 9(4):713–722, 1999.
16. A. Wolf, B. J. Swift, L. H. Swinney, and A. J. Vastano. Determining lyapunov exponent from a time series. *Physica*, 16D:285–317, 1985.

Proceedings, 5th Chaotic Modeling and Simulation International Conference, 12 – 15 June 2012, Athens Greece

Robustness and Bit Error Rate Performance of Qi Hyper Chaos Based Encryption

Guoyuan Qi
Department of Electrical Engineering
Tshwane University of Technology, Pretoria, South Africa
E-mail: qig@tut.ac.za

Dennis Luke Owuor
Department of Electrical Engineering
Tshwane University of Technology, Pretoria, South Africa
E-mail: dennisluke11@yahoo.com

André E. Botha
Department of Physics
University of South Africa, Pretoria, South Africa
E-mail: bothaae@unisa.ac.za

Abstract. Recently, in the field of telecommunication, chaotic encryption has drawn much attention because of its ease in design and implementation over conventional encryption methods. In this paper, chaos shift keying (CSK) models are designed based on Qi hyper-chaos. The efficiency and effectiveness of the developed models are evaluated using the bit error rate. By using power spectrum analysis and low pass filtering techniques, the robustness of CSK based on Qi hyper-chaos over CSK based on the Lorenz chaotic system is verified. The results show that the robustness and bit error rate performance of encryption based on Qi hyper-chaos is much better than that based on Lorenz chaos.
Keywords: Chaos, Encryption, Hyper-chaos, BER, CSK.

1. Introduction

Telecommunication as a field has tremendously grown in the last decade. Associated with this growth, is the requirement for efficient and effective secure communication methods [1]. One method of making data secure is through encryption and decryption. Over the past few years, methods of chaotic encryption have developed enormously, and several chaotic systems, such as the Lorenz, Chen and Rössler systems, have been proposed [2-5]. These systems have been employed for encryption and decryption of message signal, image and video during communication. In this context there are a number of different chaotic encryption methods that have been employed for encryption and decryption, for example, chaos synchronization, chaos shift keying and chaotic masking.

Traditional encryption schemes based on integer number theory have been studies for a long time and are considered to be reliable. In contrast, the security of chaotic communication schemes often relies on a mixture of analytic methods and intuition. Encryption and cryptanalysis using chaotic dynamics is a

relatively new field that has only been intensively researched on for less than a decade.

This paper aims to demonstrate the robustness and bit error rate performance of digital message signal encryption based on Qi hyper-chaos systems compared to message signal encryption based on Lorenz chaotic system.

2. Comparison between the Qi hyper-chaotic system and the Lorenz chaotic system

Many proposed chaos-based secure encryption have been totally or partially broken by different attacks [6, 7]. This section provides a detailed comparison between Qi hyper-chaos and the Lorenz chaotic system in terms of their randomness and disorder.
The nonlinear dynamic model representing Qi hyper-chaos is given by [8, 9]:

$$\begin{aligned} \dot{x}_1 &= a(x_2 - x_1) + x_2 x_3 \\ \dot{x}_2 &= b(x_1 + x_2) - x_1 x_3 \\ \dot{x}_3 &= -cx_2 - ex_4 + x_1 x_2 \\ \dot{x}_4 &= -dx_4 + fx_3 + x_1 x_2 \end{aligned} \tag{1}$$

Here $x_i \ (i = 1, 2, 3, 4)$ are the state variables and a, b, c, d, e, f are positive constant parameters. The well-known Lorenz system is given in Ref. [10].
The basic comparisons of the dynamic property between Qi hyper-chaos and Lorenz chaotic system are summarized in the next paragraph [8].

The attractor of Qi hyper-chaotic system exhibits a very irregular and disordered form unlike the butterfly shape produced by the Lorenz chaotic system. The Stochastic distribution of Qi hyper chaos is very similar to that of Gaussian white noise but that of Lorenz has three peaks at its trajectory is unlike Gaussian white noise. Qi hyper-chaotic signal is much more sensitive to initial condition than the Lorenz chaos and other hyper-chaos. With these rich advantages of Qi hyper chaos over Lorenz chaotic system, as demonstrated in [8], there is a need to explore the effects implementing the system for encryption of messages.

3. Qi-Hyper-Chaos-Shift Keying Encryption

3.1 Method 1: Non-Coherent Decryption Based on Bit-Energy Estimation

In this encryption scheme two hyper-chaotic signals are used to encrypt the message signal at the sending end and decryption is done at the receiving end based on energy bit estimation [11, 12].

Two chaos generators produce signals $c_1(t)$ and $c_2(t)$, respectively. During the bit duration, i.e. $[((l-1)T_b),\ lT_b]$, if a binary "+1" is about to be sent, $c_1(t)$ is transmitted, and if "−1" is about to be sent, $c_2(t)$ is transmitted.

The encrypted signal $r(t)$ is then sent through a channel of communication. Thus

$$r(t) = s(t) + \xi(t) \tag{2}$$

where $\xi(t)$ is the noise signal added to the sent signal during communication.

The decryption method used is called non-coherent demodulation based on an energy bit estimator. Decryption is done based on some distinguished characteristics of the signal transmitted. The property used in this paper is the bit energy, which is deliberately made different for different symbols in the encryption process.

A Qi hyper-chaos generator is used to produce two chaotic signals; the first chaotic system is assigned different value, i.e. $c_1(t) + M$, where M is the value assigned to separate with $c_2(t)$. At the receiving end the bit energy can be estimated by a square and integration process.

Let energy per bit be $y(lT_b)$. When the energy bit $y(lT_b) > T_h$ then binary "+1" was send, otherwise binary "−1" was send, where $T_h > 0$ is threshold value.

The simulation results of non-coherent demodulation based on bit-energy estimation are shown in Fig. 1, which demonstrates successful performance of encryption and decryption.

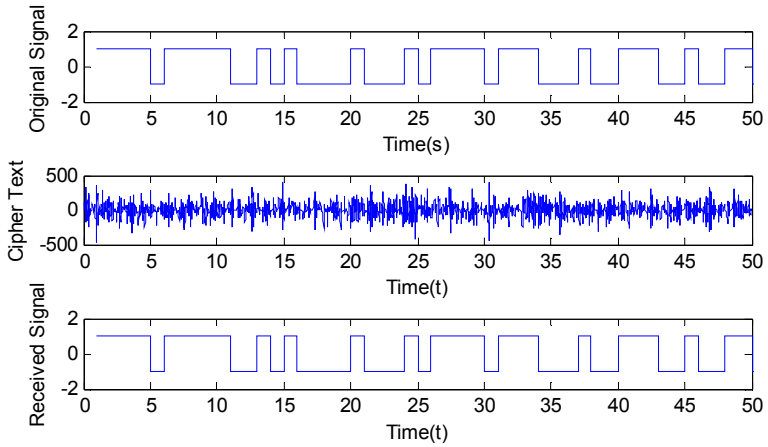

Fig. 1. Qi-Hyper-Chaos-Shift Keying Encryption and decryption

3.2 Method 2: Coherent Demodulation Based on Correlation

The process of correlation is where the "likeness" between two chaotic signals is evaluated. In this method two correlators are employed to evaluate the correlations between the received signal and the two recovered chaotic signals. The outputs of the correlators for the *l*th bit are given by

$$y_1(lT_b) = \int_{(l-1)T_b}^{lT_b} r(t)c_1'(t)\,dt \tag{3}$$

$$y_2(lT_b) = \int_{(l-1)T_b}^{lT_b} r(t)c_2'(t)\,dt \tag{4}$$

where $c_1'(t)$ and $c_2'(t)$ are synchronizations of $c_1(t)$ and $c_2(t)$, respectively.

The following equation is used to determine the output to the threshold detector.

$$y_0(lT_b) = y_1(lT_b) - y_2(lT_b) \tag{5}$$

If the output $y_o(lT_b)$ is greater than T_h then +1 was sent, otherwise -1 was sent.

The process of encryption is the same as that of Method 1, but the decryption process takes place with the aid of synchronizations. The decryption proceed by evaluating the correlation of the transmitted signal and the regenerated chaotic carrier as in Eq. (3) and eq. (4), and followed by energy bit calculation then compared in Eq. (5). If the output is greater than the value specified at the threshold then "+1" is decoded otherwise "−1" is decoded.

The simulation results of correlation-type coherent decryption for CSK with two Qi hyper chaos generators are shown in Fig. 2.

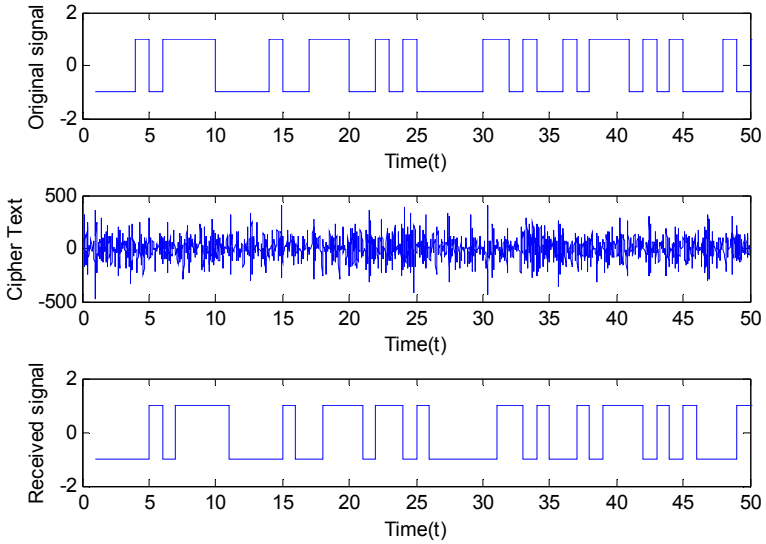

Fig. 2. Comparison between sent and received signal

4. BER Performance of CSK Based on Qi Hyper Chaos Compared to Lorenz Based CSK

Bit Error Rate (BER) is a performance measurement that specifies the number of bit corrupted or destroyed as they are transmitted from its source to its destination [13, 14].
BER measurements compare digital input and output signals to access what fractions of the bit are received incorrectly. It is defined as:

$$\mathrm{BER} = \frac{N_e}{N_t} \tag{6}$$

Where N_e is the number of error bits received over time t, and N_t is the total number of bits transmitted. Signal to Noise Ratio (SNR) is defined as the ratio of a signal power to noise power and it is normally expressed in decibel (dB). The mathematical expression of SNR is:

$$\mathrm{SNR} = 10\log_{10}\left(\frac{\mathrm{SignalPower}}{\mathrm{NoisePower}}\right)\mathrm{dB} \tag{7}$$

Relationship between the system's SNR and BER is that the higher the SNR, The lower would be the corresponding BER

$$\mathrm{BER} = \left(1/\mathrm{SNR}\right)^k \tag{8}$$

where k is a specific subcarrier index.
In this paper simulation of BER is done using Bertool tool in Matlab\Simulink.

Fig. 3 shows the comparison of the BER performance between chaos based CSK using energy bit estimation method for decryption (Simulation 0) and Qi hyper chaos CSK based using correlation method for decryption (Simulation 1).

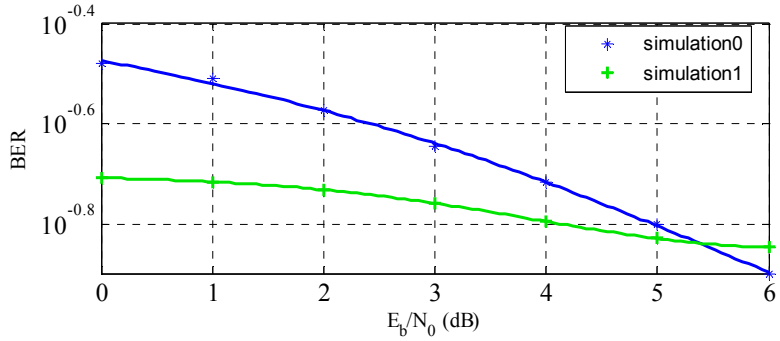

Fig 3: Comparing the BER performance between Qi hyper-chaos based CSK using energy bit estimation method for decryption and using correlation method for decryption.

The BER performance of the latter is seen to be much lower than the former; hence, the correlation method for decryption is more efficient compared the energy bit estimation method for decryption.

Qi hyper-chaos CSK based on correlation method has better performance because with the aid of synchronization the low frequency noise and high frequency noise can be easily eliminated.

5. Power Spectrum and Low Pass Filter Methods of Attacking Chaos Based Secure Communication

Security during communication is fundamental since it is one of the components that add up to effective and efficient communication. There are varieties of methods that have been proposed to attack chaos-based secure communication schemes. In different cases in literature [14] they have indicated successfully breaking of chaos encryption without knowing the secrete key or the parameters used during encryption. This kind of attack is only possible if the received message m (t) is a periodic signal or if m (t) consists of periodic frames within a given duration. The attack can be accomplished using two methods power spectrum analysis and low pass filter technique and return map analysis.
Power spectrum and low pass filter technique are very powerful schemes that can be used to break chaotic communication without knowing the parameters or the initial components used during encryption.These two methods are implemented in this paper to determine how robust CSK based on Qi hyper is.The message signal encrypted by Lorenz chaotic system hereby successfully extracted by the filter and decision circuit as shown Fig. 4

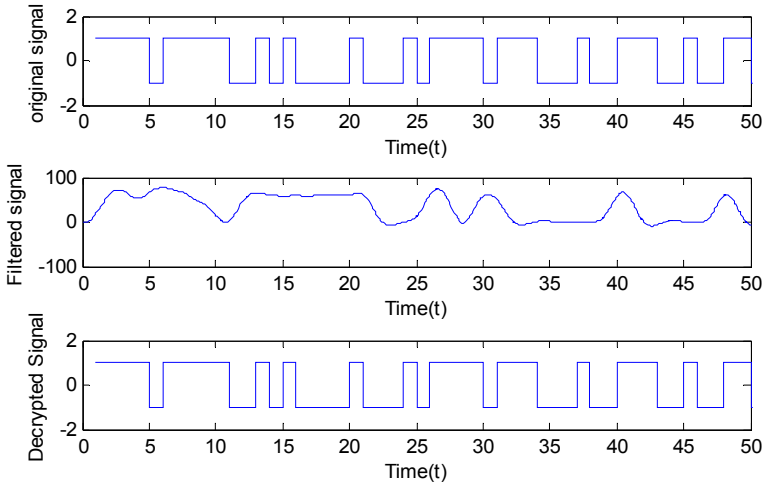

Fig. 4. Attacking Lorenz Chaos through power spectrum and low pass filter

The attempt to attack message signal encrypted based on Qi hyper-chaotic system was unsuccessfully as shown Fig. 5

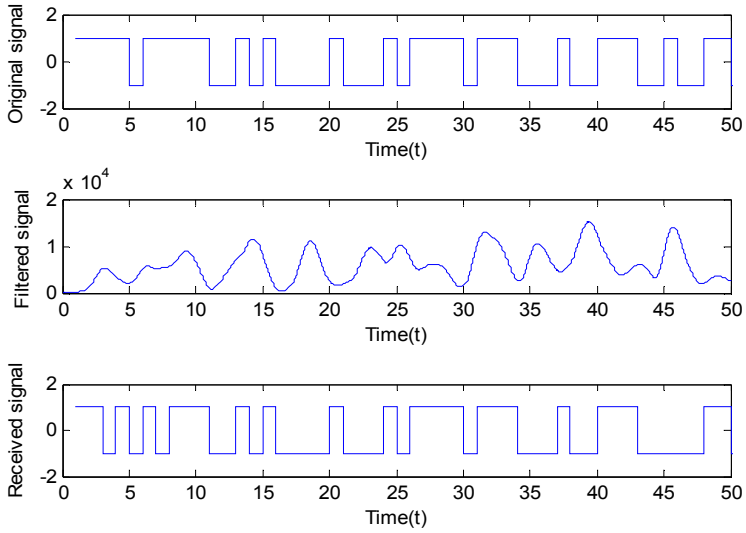

Fig. 5. Attacking Qi hyper-chaos through power spectrum and low pass filter, The simulation results in Fig. 5 indicates that it is not easy to attack digital message signal encryption based on Qi hyper-chaos. The difficulty in attacking message signal based on Qi hyper-chaos can be attributed to the rich properties of Qi hyper-chaos.

6. Conclusion

In this paper message signal based on Qi hyper-chaos has been implemented. The BER performance comparison between Qi hyper-chaos and Lorenz chaos shows that Qi hyper-chaos based CSK has better performance compared to Lorenz based CSK. The rich properties of Qi hyper chaos such us high frequency spectrum, high level of disorder, etc. have made it very cumbersome for low pass-filter and power spectrum analysis method to be successful in attacking and decrypting the encrypted message signal sent.

References

1. C. I. Rincu and A. Serbanescu. Chaos-Based Cryptography. A Possible Solution For Information Security, *Bulletin of the Transilvania University of Brasov*, vol. 2,51, 2009.
2. M. Baptista. Cryptography with chaos, *Physics Letters A*, vol. 240: 50-54, 1998.
3. L. M. Pecora and T. L. Carroll. Synchronization in chaotic systems, *Physical review letters*, vol 64: 821-824, 1990.
4. T. L. Carroll and L. M. Pecora. Synchronizing chaotic circuits, *Circuits and Systems, IEEE Transactions*, vol. 38: 453-456, 1991.
5. J. Lü and G. Chen. A new chaotic attractor coined, *Int. J. Bifurc. Chaos,* vol. 12: 659–661, 2002.
6. G. Álvarez, S. Li. Comput, *Commun*, vol. 27, 2004.
7. G. Hu, Z. Feng, R. Meng, *IEEE Trans. Circuits Syst.* 50-275, 2003.
8. G. Qi, et al. On a new hyperchaotic system, *Physics Letters A,* vol. 372:124-136, 2008.
9. G. Qi, et al. "A new hyperchaotic system and its circuit implementation, *Chaos, Solitons & Fractals,* vol. 40:2544-2549, 2009.
10. E. N. Lorenz. Deterministic nonperiodic flow, *J. Atmospheric Sc.,* vol. 20: 130-141, 1963.
11. C. Tse and F. Lau. Chaos-based digital communication systems, *Operating Principles, Analysis Methods and Performance Evaluation (Springer Verlag, Berlin)* 2004.
12. M. P. Kennedy and G. Kolumbán. *Digital communications using chaos*, *Signal processing*, vol. 80: 1307-1320, 2000.
13. W. M. Tam, et al. An approach to calculating the bit-error rate of a coherent chaos-shift-keying digital communication system under a noisy multiuser environment, Circuits and *Systems: Fundamental Theory and Applications, IEEE Transactions*, vol. 49:210-223, 2002.
14. M. Sushchik, et al. Performance analysis of correlation-based communication schemes utilizing chaos, Circuits *and Systems I: Fundamental Theory and Applications, IEEE Transactions*, vol. 47:1684-1691, 2000.

Proceedings, 5th Chaotic Modeling and Simulation International Conference, 12 – 15 June 2012, Athens Greece

Noise and nonlinear transport treatment by Monte Carlo method in n-type GaAs crystal *

Raguotis Romas

Centre of Physical Sciences and Technology, Seiconductor Physics Institute
Vilnius, Lithuania, e-mail: romasr@pfi.lt

Abstract: Monte Carlo "combine-scattering-rate" technique is used for the investigation of the noise and nonlinear transport phenomena in *n*-type GaAs crystal at *T* = 78 and 300 K. This technique avoids the short-time-step procedure inherent to conventional ensemble Monte Carlo method. Quantitative agreement with the available experimental data on the noise spectral density is achieved. Electron collisions with phonons, impurities and among themselves are taken into account. The time-dependent drift-to-drift velocity electron correlation function is demonstrated. The nonzero equal-time cross-correlation function is calculated in moderate electric fields.
Keywords: Monte Carlo, Electron-electron collisions, Drift velocity fluctuations, Spectral density.

1. Introduction

Fluctuation phenomena in semiconductors have been intensively investigated during the last three decades [1-3]. Fluctuation effects have been conventionally examined without an account on the Coulomb pair electron-electron (ee) scattering. However, at sufficiently high electron densities it is necessary to take into account ee scattering contribution to the distribution function and related correlators. In the presented report the 'combined scattering' (CSR) Monte Carlo (MC) method [4] is used to interpret the results of microwave noise in n-type GaAs crystal.

The important role of e-e collisions is demonstrated, and drift-velocity to drift

* Paper included in *Chaotic Systems: Theory and Applications*, C.H. Skiadas and I. Dimotikalis, Eds, World Scientific, pp 302—308, 2010.

velocity correlation function under non-e1uilibrium conditions is discribed. The response of electron ensemble to the switched on electric field is also simulated.

2. Results and discussion

It has been shown [4] that the "time of free flight" for independent scattering events of the N electron system with $\mathbf{k}_i$ wave-vectors is defined by the combined scattering rate:

$$\lambda_{comb}(\mathbf{k}_1,\mathbf{k}_2,...,\mathbf{k}_N)=\sum_{i=1}^{N}\lambda_i(\mathbf{k}_i)+\frac{1}{N-1}\sum_{i=1}^{N-1}\sum_{j=i+1}^{N}\lambda_{ij}^{ee}(\mathbf{k}_i,\mathbf{k}_j)\,, \qquad (1)$$

where $\lambda_i(\mathbf{k}_i)$ and $\lambda_{ij}^{ee}(\mathbf{k}_i,\mathbf{k}_j)$ are conventional integral rates of scattering of the i^{th} electron by the thermal bath and by the j^{th} electron respectively [5]. Equation (1) reduces to that written down in [6] for N=2. All N electrons move without scattering for the "time of free flight of the ensemble" between two successive events of an electron scattering by the thermal bath, or mutual collision between two electrons occurs. The "time of free flight" is defined from the sum of the each electon scattering rate on the thermal bath and on the all remaining electrons. CSR technique avoids the short-time step procedure and a large electron number inherent to conventional ensemble EMC simulation. This technique allows to simulate the dynamic of electron ensemble. Evidently, Eq. (1) can be modified to consider collisions of different quasiparticles: electron and holes, light anh heavy holes, Γ and X electronc, etc.
The time-displaced drift-velocity correlation function is

$$\Phi_{total}(t)=N\overline{\delta v_d(t_1+t)\delta v_d(t_1)}=\Phi_{auto}(t)+\Phi_{cross}(t)\,, \qquad (2)$$

where the auto- and cross-correlation functions are defined as:

$$\Phi_{auto}(t)=\overline{\frac{1}{N}\sum_i \delta v_i(t_1+t)\delta v_i(t_1)},\quad \Phi_{cross}(t)=\overline{\frac{1}{N}\sum_{i\neq j}\delta v_i(t_1+t)\delta v_j(t_1)}\,. \qquad (3)$$

The main features of the velocity time-displaced correlation in the presence of e-e collisions can be illustrated for the case when the relaxation time of the ee interaction τ_{ee} is shorter than that of the electron momentum relaxation time τ_p. In this case the autocorrelation function, starting from the its equal-time value

$$\Phi_{auto}(0)=\overline{v_i^2}=kT/m \qquad (4)$$

decreases with t due to the ee collisions mainly, and the shortest time constant τ_{ee} dominates on the decay of the $\Phi_{auto}(t)$ in a short time scale.

In equilibrium state there is no equal-time cross correlation $\Phi_{cross}(0) = 0$. The theory of kinetic correlations [1] predicts the equal-time cross correlation to appear in the non-equilibrium system in which ee collisions are essential.

In order to demonstrate the effect of ee collisions on fluctuations the calculated velocity correlation functions in heating electric field is shown in figure 1 for a model corresponding to n-type GaAs with the impurity scattering neglected.

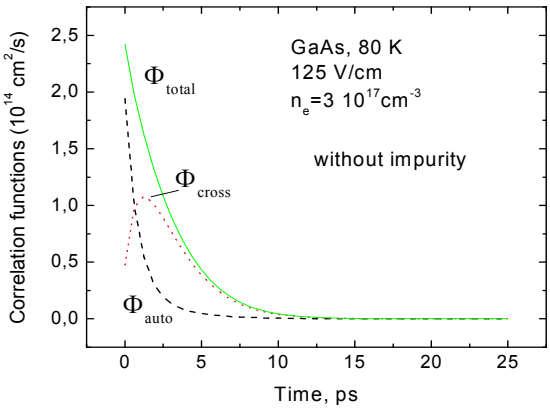

Fig. 1. Time-displaced electron velocity correlation function. Drift-velocity correlation function - total line, autocorrelation – dashed line, cross correlation– dotted line. Phonon and ee scattering mechanism are taken into account, impurity scattering is neglected.

Well defined nonzero $\Phi_{cross}(0)$ reveals. Inter-electron collisions, conserving energy and momentum, cause the correlations between electrons involved. Therefore, for small t, $\Phi_{cross}(t)$ grows proportionally to t [1]. The opposite tendencies in the evolution of $\Phi_{auto}(t)$ and $\Phi_{cross}(t)$ counterbalance each other [4,,7,8]. $\Phi_{total}(t)$ decay is caused mainly by the interaction of electrons with the thermal bath.

The electron system tends to conserve the electronic noise and redistribute it between the electrons in such a manner that the decay of the autocorrelation function accompanied by the emergence of the cross correlation.

The dependence of the equal-time $\Phi_{cross}(0)$ on electric field is demostrated in Figure 2.

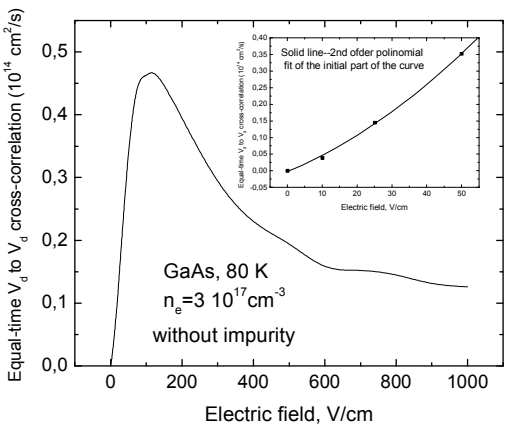

Fig. 2. Egual-time cross-correlation function versus electric field.

$\Phi_{cross}(0)$ increases from zero at zero field, then approached maximum value and decrease with E The fluctuation effects are symmetric with respect of electric field direction. It is clearly seen in the figure 2 insert, where the calculated MC points well coincide with the 2nd order polynomial fit Next the nonlinear effects manifest, and Φ_{cross} increases. The Coulomb scattering mechanisms gradually switches off with an increase of electron energy, therefore, $\Phi_{cross}(0)$ reaches the maximum value and then monotonically decreases with E.

Knowledge of the correlation functions makes the simulation straightforward of the spectral of electron velocity fluctuations for a realistic model of electron gas. The results of calculation are presented in figure 3 and are compared with the experimential values.

The results on the spectral density of drift velocity fluctuations at 80 K were also published in [4]. The degree of compensation has been estimated fitting low-field mobility to the experimental data.

The spectral density of velocity fluctuations at 80 K remains nearly constant up to fields 200 V/cm. (Fig. 2, open and closed squares). This behavior can be explained by enhanced energy loss by electrons on optical phonons in the presence of ee scattering [9].

The spectral density of velocity fluctuations at 300 K weakly depends on ee scattering. At T=300 K the mean electron energy fourfold times exceeds the one at T=80 K, and ee scattering is of less important. Nevertheless slightly better coincidence is achieved with experimental data when ee scattering is included.

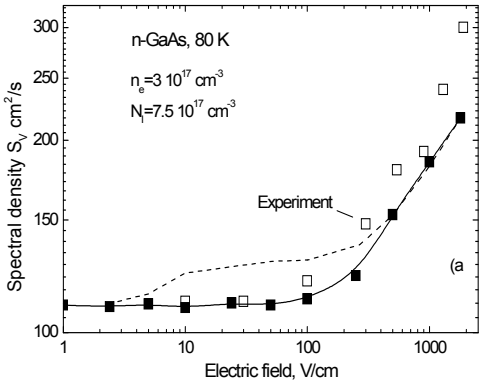

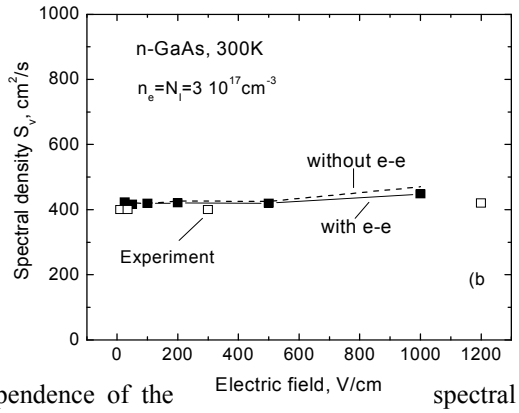

Fig. 3. The dependence of the spectral density of electron drift-velocity fluctuations for n-type GaAs at 80 (a) and 300 K (b) versus electric field. Monte Carlo simulation with phonon, impurity, and ee scattering taken into account (closed squares), without ee scattering (dots). Experimental data─open squares.

The time-response of electron kinetic characteristics on the switched on electric field was also calculated. The results are presented in Figure 4. It is seen that ee scattering reduced electron drift velocity and especially there energy.

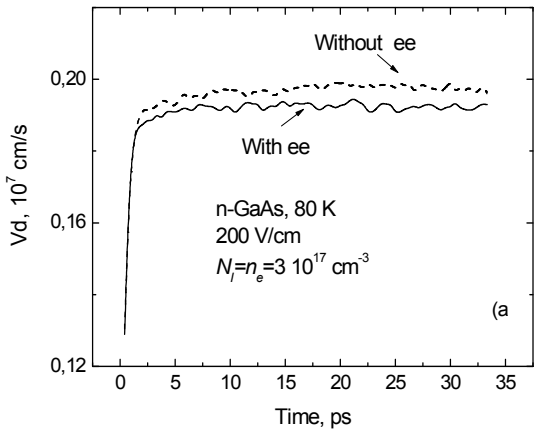

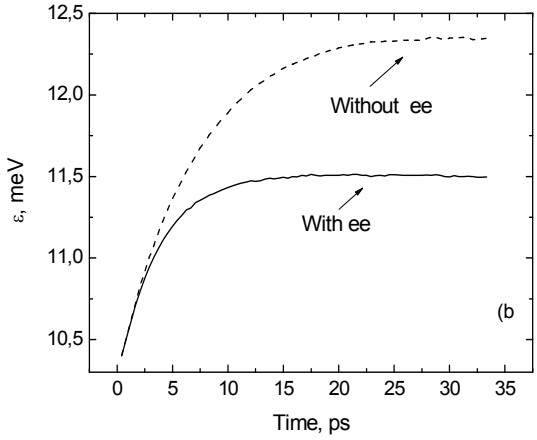

Fig. 4. The response of electron drift velocity (a) and mean energy (b) in n-type GaAs at 80 K versus time. Sharply switched on electric field E=200 V/cm.

Conclusions

The results of the Monte Carlo calculations of drift velocity to drift velocity fluctuations and the time-response of the electron drift-velocity and mean energy to the instantaneously switched electric field is presented. Electron system behaves as whole unit seeking to conserve so inherent characteristics as their drift velocity and the mean energy. This can be clearly observed in the fluctuations treatment. When autocorrelation decreases, the crosscorrelation appears in the presence of electron-electron pair collisions. The thermostat and internal forces contrary tends to destroy the order of the system. Electron-electron scattering also indirectly influences kinetic characteristics. It reduce the spectral noise of the system, and effectively influence kinetic values,

diminishing as electron velocity as the mean energy.

Acknowledgment

I am grateful for prof. R. Katilius for helpful discussion.

Reference

1. S. V. Gantsevich, V.L.Gurevich, Katilius. R. *Riv. Nuovo Cimento* 2: 1-87, 1979.
2. Sh. Kogan. *Electronic Noise and Fluctuations in Solids.*Cambridge University Press, Cambrige, Ghap. 3, 1996.
3. H. L. Hartnagel, R. Katilius and A. Matulionis. *Microwave noise in Semiconductor Devices*, Wiley & Sons, New York, 2001.
4. A. Matulionis, R. Raguotis, and R. Katilius. *Phys. Rev. B 56*: 2052–2057, 1997.

5. C. Jacoboni and P. Lugli. *The Monte Carlo method for SemiconductorDevice Simulation.* (Springel-Verlag, Wien,) 1989.

6. A. Hasegawa, K. Miyatsuji, K. Tanaguchi, and C. Hamaguhi. *Solid-State Electron.* 31: 547-550, 1988.

7. R. Raguotis. *J. Phys. Condens. Matter*. 16: 3973-3670, 2004.

8. R. Raguotis. *Chaotic Modeling and Simulation 1:199-205, 2011*

9. I. B. Levinson and G. E. Mazhuolyte, Zn. Eksp. Teor. Fiz. **50**, 1048 (1966) [Sov. Phys. JETP **23**, 697 (1966)].


Proceedings, 5th Chaotic Modeling and Simulation International Conference, 12 – 15 June 2012, Athens Greece

Analysis of 1-D Linear Piecewise-smooth Discontinuous Map

Bhooshan Rajpathak[1], Harish Pillai[1], and Santanu Bandyopadhyay[1]

Indian Institute of Technology Bombay, Mumbai, India
(E-mail: bhooshanar@iitb.ac.in)
(E-mail: hp@iitb.ac.in)
(E-mail: santanu@iitb.ac.in)

Abstract. In this paper we analyze the stable periodic orbits existing in the 1-D linear piecewise-smooth discontinuous map with respect to variations in the parameters of the map. We analytically show how to calculate the range of parameter μ such that the orbits of specific periodicity can exist. Moreover, for a given period, the relation between the probability of occurrence of orbits of that period and the corresponding length of range of μ is established. Further, we show that this probability can be maximized by varying the parameter of the map. We prove that there exist a unique value of this parameter such that this probability is maximum. We provide diagrams generated by numerical simulations to illustrate these results and to depict the effects of variations in the parameters of the map on the ranges of existence of orbits.
Keywords: Border collision bifurcation, piecewise-smooth, discontinuous map, periodic orbit.

1 Introduction

Piecewise-smooth dynamical systems are being extensively studied over the last decade because of their applications in various fields like electrical engineering, physics, economics etc. Examples are DC-DC converters in discontinuous mode [1,2], impact oscillators [3], economic models [4] etc. One of the major reasons for interest in piecewise-smooth systems is the existence of a phenomenon, unique to such systems, called *border collision bifurcation*. Though this term was coined by Nusse [5] in 1992, the phenomenon was earlier reported by Feigin [6] in 70's.

The 1-D linear piecewise-smooth discontinuous map is defined as [7]:

$$x_{n+1} = f(x_n, a, b, \mu, l) = \begin{cases} ax_n + \mu & \text{for } x_n \leqslant 0 \\ bx_n + \mu + l & \text{for } x_n > 0 \end{cases} \tag{1}$$

Over the last decade, several authors have published the analytical as well as numerical work which analyzes the 1-D piecewise-smooth discontinuous map in detail [8–11]. Recently in [12] it was shown that exactly $\phi(n)$ stable periodic orbits exist in the map given by Equation (1) when $a, b \in (0, 1)$, $l = -1$ and $\mu \in (0, 1)$; where n is the period and ϕ is Euler's number. In this paper we extend this analysis to investigate the effect of variation in parameters a, b and n on the range of existence of periodic orbits.

1.1 Notation

Let $\mathcal{L} := (-\infty, 0]$ (the closed left half plane) and $\mathcal{R} := (0, \infty)$ (the open right half plane). Given a particular sequence of points $\{x_n\}_{n\geqslant 0}$ through which the system evolves, one can convert this sequence into a sequence of $\mathcal{L}s$ and $\mathcal{R}s$ by indicating which of the two sets ($\mathcal{L}$ or $\mathcal{R}$) the corresponding point belongs to. Since a periodic orbit has a string of $\mathcal{L}s$ and $\mathcal{R}s$ that keeps repeating, we call this repeating string, a *pattern* and denote it by σ. The length of the string σ is denoted by $|\sigma|$ and gives the number of symbols in the pattern i.e., the period of the orbit. The range of existence of this pattern σ is denoted by $\mathcal{P}_\sigma = (p_1, p_0 2]$ where p_2 and p_1 are the upper and the lower limits respectively. The sum of geometric series $1 + k + k^2 + \cdots + k^n$ is denoted by S_n^k.

1.2 Preliminaries

Definition 1. A pattern σ is termed *admissible* if $\mathcal{P}_\sigma \neq \varnothing$.

Definition 2. If a pattern consists of a single chain of consecutive $\mathcal{L}s$ followed by a singleton $\mathcal{R}$ then it called an $\mathcal{L}$-prime pattern. Similarly, if a pattern consists of a single chain of consecutive $\mathcal{R}s$ followed by a singleton $\mathcal{L}$ then it called an $\mathcal{R}$-prime pattern. Together, we call them *prime patterns*.

Example 1. $\mathcal{L}^{\mathrm{n}}\mathcal{R}$ is a $\mathcal{L}$-prime pattern and $\mathcal{L}\mathcal{R}^{\mathrm{n}}$ is a $\mathcal{R}$-prime pattern. $\mathcal{L}\mathcal{R}$ is both $\mathcal{L}$-prime as well as $\mathcal{R}$-prime.

Definition 3. A pattern made up of two or more prime patterns is called a composite pattern.

Example 2. $\mathcal{L}\mathcal{L}\mathcal{L}\mathcal{R}\mathcal{L}\mathcal{L}\mathcal{R}$ is a composite pattern as it is made of two prime patterns namely $\mathcal{L}\mathcal{L}\mathcal{L}\mathcal{R}$ and $\mathcal{L}\mathcal{L}\mathcal{R}$.

Remark 1. Some authors use the term *maximal* or *principal* to describe prime pattern [13].

Recall that the range of existence of an orbit is denoted by $\mathcal{P}_\sigma$. We illustrate with an example how to calculate $\mathcal{P}_\sigma$.

Example 3. Consider a pattern $\mathcal{L}\mathcal{L}\mathcal{R}$ which means: $x_0, x_1 \leqslant 0, x_1 > 0$ and $x_3 = x_0$. Using Equation (1) these inequalities can be rewritten as:

$$
\begin{aligned}
&x_0 \leqslant 0,\\
&x_1 = ax_0 + \mu \leqslant 0,\\
&x_2 = a^2x_0 + (a+1)\mu > 0,\\
&x_3 = x_0 = a^2bx_0 + (ab+b+1)\mu - 1 \Rightarrow x_0 = \frac{(ab+b+1)\mu - 1}{1 - a^2b}.
\end{aligned}
$$

Substituting the value of x_0 in x_1 and x_2 we get:

$$x_1 = a\Big(\frac{(ab+b+1)\mu - 1}{1-a^2b}\Big) + \mu \leqslant 0,$$
$$x_2 = a^2\Big(\frac{(ab+b+1)\mu - 1}{1-a^2b}\Big) + (a+1)\mu > 0.$$

After simplification we get:

$$\mu > \frac{a^2}{a^2+a+1},$$
$$\mu \leqslant \frac{a}{ab+a+1}.$$

Hence, $\mathcal{P}_{\mathcal{LLR}} = \Big(\frac{a^2}{a^2+a+1}, \frac{a}{ab+a+1}\Big]$.

In a similar way we can find the range of existence ($\mathcal{P}_\sigma$) for the prime patterns $\mathcal{L}^n\mathcal{R}$ and $\mathcal{L}\mathcal{R}^n$ for any $n \geqslant 2$. The method is explained in detail in [12]. We directly use the formulas from [12] here:

$$\mathcal{P}_{\mathcal{L}^n\mathcal{R}} = \left(\frac{\boldsymbol{a^n}}{\boldsymbol{S_n^a}}, \quad \frac{\boldsymbol{a^{n-1}}}{\boldsymbol{a^{n-1}b + S_{n-1}^a}}\right] \tag{2}$$

and

$$\mathcal{P}_{\mathcal{L}\mathcal{R}^n} = \left(\frac{\boldsymbol{ab^{n-1} + S_{n-2}^b}}{\boldsymbol{ab^{n-1} + S_{n-1}^b}}, \quad \frac{\boldsymbol{S_{n-1}^b}}{\boldsymbol{S_n^b}}\right]. \tag{3}$$

1.3 Characterization of Patterns

We have seen earlier that the prime patterns are admissible and the range of existence of prime patterns is given by Equations (2) and (3). The immediate question is other than prime patterns, which type of patterns are admissible? It is shown in [12] that only specific type of patterns are admissible. For example, it is shown that admissible patterns can not contain consecutive chain of $\mathcal{L}$s and $\mathcal{R}$s simultaneously. Moreover, admissible composite patterns are always made up of exactly two prime patterns of successive lengths. Further, it is shown that these results lead to the final conclusion that exactly $\phi(n)$ number of distinct patterns are admissible for a given n.

For a given n, the algorithm to generate the $\phi(n)$ patterns and to calculate the range of existence of these patterns is discussed in detail in [12]. We now extend this analysis to find out the effects of variations in parameters on the range of existence of patterns.

2 Effects of Variations in Parameters on The Range of Existence of Patterns

In this section we analyze the effects of variations in parameters a, b and n on the range of existence of patterns. Recall that the range of existence of pattern σ is expressed as $\mathcal{P}_\sigma = (p_1, p_2]$. Let the length occupied on the parameter line μ corresponding to the i^{th} pattern of length n is denoted by Γ_i^n. That is, $\Gamma_i^n = p_2 - p_1$. Let the total length occupied corresponding to all the patterns of length n is denoted by Γ^n. That is, $\Gamma^n = \sum_{i=1}^{\phi(n)} \Gamma_i^n$. We now find out the expression for Γ^n. In this paper we consider the case of $a = b$.

Consider the pattern of length $N = n + 1$. We substitute $a = b$ in Equations (2) and (3) to get:

$$\mathcal{P}_{\mathcal{L}^n\mathcal{R}} = \left(\frac{a^n}{S_n^a}, \frac{a^{n-1}}{S_n^a}\right] \text{ and } \mathcal{P}_{\mathcal{L}\mathcal{R}^n} = \left(\frac{a^n + S_{n-2}^a}{S_n^a}, \frac{S_{n-1}^a}{S_n^a}\right].$$

Note that $\Gamma^N_{\mathcal{P}_{\mathcal{L}^n\mathcal{R}}} = \Gamma^N_{\mathcal{P}_{\mathcal{L}\mathcal{R}^n}} = \frac{a^{n-1}(1-a)}{S_n^a}$. We denote it by γ^N. Since, for $a = b$ the map becomes symmetric, all the patterns of length N have $\Gamma_i^N = \gamma^N$. This gives $\Gamma^N = \sum_{i=1}^{\phi(N)} \Gamma_i^N = \phi(N)\gamma^N$. Substituting for γ^N and N we get $\Gamma^{n+1} = \phi(n+1)\frac{a^{n-1}(1-a)}{S_n^a} = \phi(n+1)\frac{a^{n-1}(1-a)^2}{1-a^{n+1}}$. For consistency, we use the formula for n which is:

$$\Gamma^n = \phi(n)\gamma^n = \phi(n)\frac{a^{n-2}(1-a)^2}{1-a^n}. \tag{4}$$

From the above equation it is clear that Γ^n depends on the parameters a and n. Recall that Γ^n is the length of range of existence of patterns as defined earlier. Hence, any change in Γ^n due to the variations in a and n can be interpreted as the effect on the range of existence of patterns.

2.1 Probability of Occurrence of a Pattern

We have seen that the total length occupied on the parameter line μ corresponding to all the patterns of length n is expressed by Γ^n. We know $\mu \in (0, 1)$. This leads us to the question: for a randomly selected μ from the set $(0, 1)$, what is the probability that it corresponds to a pattern of length n? Since $\mu \in (0, 1)$, the total length of the parameter line is unity and Γ^n is the total length occupied on parameter line μ corresponding to all the patterns of length n. Hence, the probability of occurrence of a pattern of length n is Γ^n. The Equation (4) gives the formula for this probability in terms of a and n.

2.2 Maximizing the Probability of Occurrence of a Pattern

For $n = 2$, $\Gamma^2 = \frac{1-a}{1+a}$ and $a \in (0, 1)$. Clearly, it is a monotonically decreasing function. Hence, the suprimum is achieved at $a = 0$. For all $n > 2$, Γ_n is not monotonic. With bit more analysis we can show that Γ^n attains maxima for a particular value of $a \in (0, 1)$. This can be calculated by differentiating Γ^n with respect to a.

$$\frac{d}{da}(\Gamma^n) = \frac{d}{da}(\phi(n)\gamma^n) = \phi(n)\left(a^n - \frac{n}{2}a + \frac{n}{2} - 1\right). \tag{5}$$

We check that the expression $a^n - \frac{n}{2}a + \frac{n}{2} - 1$ has only one real root in $(0, 1)$. At that root, $\frac{d^2}{da^2}(\Gamma^n) = a^{n-1} - \frac{1}{2}$ is negative. Hence, for a given n, there is an unique value of a such that Γ_n is maximum.

Example 4. We plot Γ^n versus n for different values of a. In these plots, n is varied from 2 to 14. These graphs (see Figure 1a to Figure 1e) show that as n increases, the position of maxima for Γ_n increases too. This means, higher the value of a, greater is the probability of occurrence of high period orbits. For the same values of a, figures 1b to 1f shows the bifurcation diagrams. We note that above results are validated by the bifurcation diagrams.

The graphs of Γ^n versus a, for different values of n, are plotted in figures from 1g to 1i. In these plots, a is varied from 0.01 to 0.99. From these plots we can see that Γ^2 is indeed a monotonically decreasing function. For vary small values of a, Γ_2 almost completely occupies the parameter line. For example, when $a = 0.1$, $\Gamma^2 = 0.818$. For all $n > 2$ is clear from the graphs that Γ^n is not monotonic and the maxima attained varies as n changes.

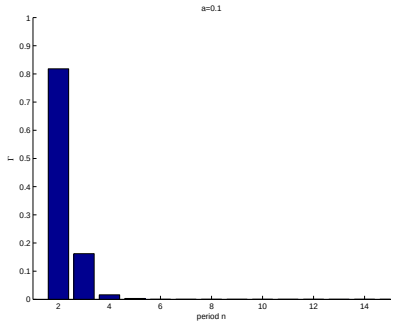

Fig. 1a. Graph showing Γ^n for different values of n. $a = 0.1$

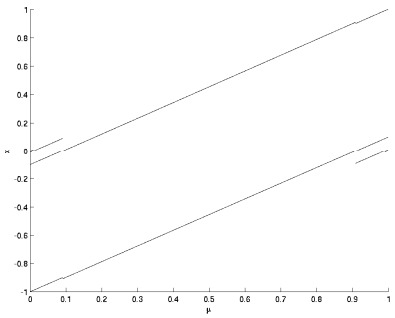

Fig. 1b. Bifurcation Diagram for $a = b = 0.1$

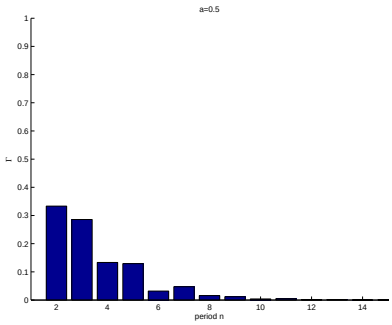

Fig. 1c. Graph showing Γ^n for different values of n. $a = 0.5$

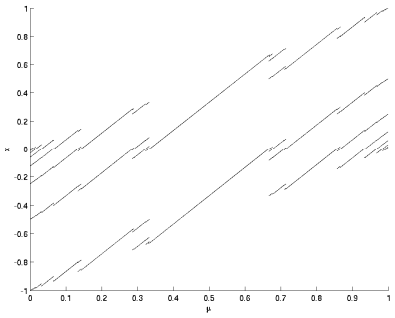

Fig. 1d. Bifurcation Diagram for $a = b = 0.5$

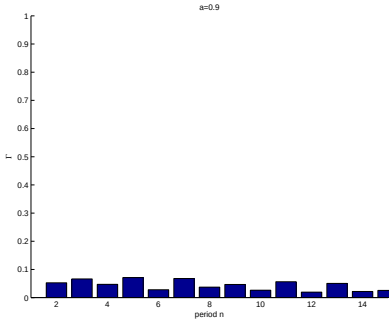

Fig. 1e. Graph showing Γ^n for different values of n. $a = 0.9$

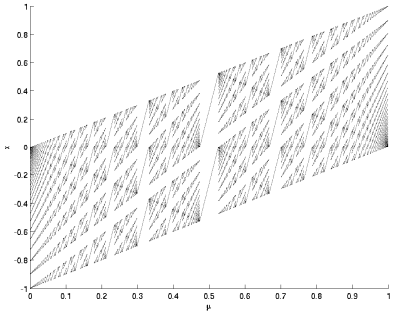

Fig. 1f. Bifurcation Diagram for $a = b = 0.9$

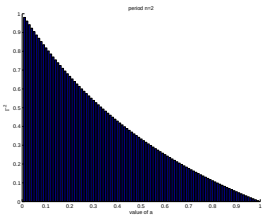

Fig. 1g. Graph showing Γ^n for different values of a. $n = 2$

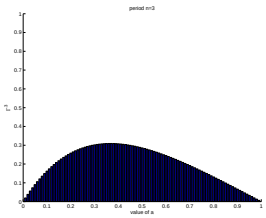

Fig. 1h. Graph showing Γ^n for different values of a. $n = 3$

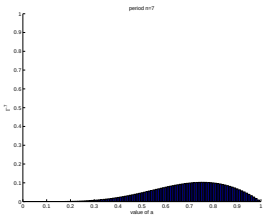

Fig. 1i. Graph showing Γ^n for different values of a. $n = 7$

2.3 Patterns Completely Span The Parameter Line μ

We know that Γ^n gives the total length occupied on the parameter line μ corresponding to all the patterns of length n. We have shown that for $a = b$, Γ^n can be maximized by appropriately choosing the value of a. Now let the total length occupied on the parameter line μ corresponding to all the possible patterns be denoted by Γ. That is, $\Gamma = \sum_{n=2}^{\infty} \Gamma^n$. The following lemma proves that $\Gamma = 1$ and it completely spans the parameter line μ.

Lemma 1. *For every $\mu \in (0, 1)$, there exists a pattern.*

Proof. We know that $\mathcal{P}_{\mathcal{L}^n\mathcal{R}} = (\sigma_1, \sigma_2] = \left(\frac{a^n}{S_n^a}, \quad \frac{a^{n-1}}{a^{n-1}b+S_{n-1}^a}\right]$ and $\mathcal{P}_{\mathcal{L}^{n-1}\mathcal{R}} = (\sigma_1', \sigma_2'] = \left(\frac{a^{n-1}}{S_{n-1}^a}, \quad \frac{a^{n-2}}{a^{n-2}b+S_{n-2}^a}\right]$. Hence, for any arbitrarily given $\mu \in (0, 1)$ we can find an 'n' such that
Step 1: either $\mu \in \mathcal{P}_{\mathcal{L}^n\mathcal{R}}$or $\mu \in \mathcal{P}_{\mathcal{L}^{n-1}\mathcal{R}}$or $\sigma_2 < \mu < \sigma_1'$.
For the first two cases the pattern exists as μ belongs to the range of existence of a pattern. For the last case we proceed further by calculating $\mathcal{P}_{\mathcal{L}^n\mathcal{R}\mathcal{L}^{n-1}\mathcal{R}} = (\sigma_1'', \sigma_2'']$. Now again we have three cases:
Step 2: either $\mu \in \mathcal{P}_{\mathcal{L}^n\mathcal{R}\mathcal{L}^{n-1}\mathcal{R}}$ or $\sigma_2 < \mu < \sigma_1''$ or $\sigma_2'' < \mu < \sigma_1'$.
For the first case the pattern exists as μ belongs to the range of existence of a pattern. For the second case we again go to Step 1 but this time with $\mathcal{P}_{\mathcal{L}^n\mathcal{R}}$ and $\mathcal{P}_{\mathcal{L}^n\mathcal{R}\mathcal{L}^{n-1}\mathcal{R}}$. Similarly for the third case we go to Step 1 with $\mathcal{P}_{\mathcal{L}^n\mathcal{R}\mathcal{L}^{n-1}\mathcal{R}}$ and $\mathcal{P}_{\mathcal{L}^{n-1}\mathcal{R}}$. Without the loss of generality we assume the second case to be true i.e. μ always lay in the left side partition or nearer to $\mathcal{P}_{\mathcal{L}^n\mathcal{R}}$. Then, before every time we take Step 2, we construct the new pattern of form $(\mathcal{L}^n\mathcal{R})^k\mathcal{L}^{n-1}\mathcal{R}$ with $k = 2, 3, 4\ldots$ With the help of generalized map method explained in [12] this pattern can be written as $\mathcal{L}'^k\mathcal{R}'$ where, $\mathcal{L}' = \mathcal{L}^n\mathcal{R}$ and $\mathcal{R}' = \mathcal{L}^{n-1}\mathcal{R}$.

This process is nothing but constructing a series of intervals $\mathcal{P}_{\mathcal{L}'^k\mathcal{R}'}$. This series of intervals must converge at σ_2. This is because, if it converges at some other point (say $\tilde{\sigma_1}$) then we get a finite length subinterval $(\sigma_2, \tilde{\sigma_1}]$. We arbitrarily select any point from this interval (say $\tilde{\mu}$). Now as we argued for the case of $\mathcal{P}_{\mathcal{L}^n\mathcal{R}}$, similar arguments can be made here i.e. we can select a large enough k (since limits of $\mathcal{P}_{\mathcal{L}'^k\mathcal{R}'}$ involve a and b with k in power) such that $\mathcal{P}_{\mathcal{L}'^k\mathcal{R}'}$ lies to the left of $\tilde{\mu}$. This is contradiction to the earlier assumption that series converges to $\tilde{\sigma}$. Hence, the series must converge to σ_2.

3 Conclusions

In this paper we have analyzed the stable periodic orbits of the 1-D linear piecewise-smooth discontinuous map with respect to change in the parameters. We have analytically calculated the range of parameters for which period-n orbits exist. The length of this range is considered as the probability of occurrence of period-n orbit. Further, we have shown that this probability

can be maximized by varying the parameter of the map and we prove that there exist an unique value of this parameter such that this probability is maximum.

References

1.J. H. B. Deane and D. C. Hamill, "Instability, subharmonics and chaos in power electronics circuits," in *Power Electronics Specialists Conference*, vol. 1. IEEE, June 1990, pp. 34–42.
2.C. K. Tse, "Flip bifurcation and chaos in three-state boost switching regulators," *IEEE Transactions on Circuits and Systems I: Fundamental Theory and Applications*, vol. 41, no. 1, pp. 16–23, Jan 1994.
3.E. Pavlovskaia, M. Wiercigroch, and C. Grebogi, "Two-dimensional map for impact oscillator with drift," *Physical Review E*, vol. 70, no. 3, pp. 362 011–362 019, September 2004.
4.F. Tramontana, L. Gardini, and F. Westerhoff, "Heterogeneous speculators and asset price dynamics: Further results from a one-dimensional discontinuous piecewise-linear map," *Computational Economics*, vol. 38, no. 3, pp. 329–347, October 2011.
5.H. Nusse and J. Yorke, "Border-collision bifurcations including period two to period three for piecewise smooth systems," *Physica D: Nonlinear Phenomena*, vol. 57, no. 1, pp. 39–57, June 1992.
6.M. Feigin, "Doubling of the oscillation period with c-bifurcations in piecewise-continuous systems," *Journal of Applied Mathematics and Mechanics*, vol. 34, pp. 861–869, 1970.
7.P. Jain and S. Banerjee, "Border collision bifurcation in one-dimensional discontinuous maps," *International Journal of Bifurcation and Chaos*, vol. 13, no. 11, pp. 3341–3351, November 2003.
8.S. Hogan, L. Higham, and T. Griffin, "Dynamics of a piecewise linear map with a gap," *Proceedings of the Royal Society A: Mathematical, Physical and Engineering Sciences*, vol. 463, no. 2077, pp. 49–65, January 2006.
9.V. Avrutin, A. Granados, and M. Schanz, "Sufficient conditions for a period incrementing big bang bifurcation in one-dimensional maps," *Nonlinearity*, vol. 24, no. 9, pp. 22 475–2598, September 2011.
10.V. Avrutin, M. Schanz, and B. Schenke, "Coexistence of the bandcount-adding and bandcount-increment scenario," *Discrete Dynamics in Nature and Society*, vol. 2011, no. 681565, pp. 1–30, January 2011.
11.L. Gardini and F. Tramontana, "Border collision bifurcation curves and their classification in a family of 1d discontinuous maps," *Chaos, Solitons & Fractals*, vol. 44, no. 4-5, pp. 248–259, May 2011.
12.B. Rajpathak, H. Pillai, and S. Bandyopadhyay, "Analysis of stable periodic orbits in the 1-d linear piecewise-smooth discontinuous map," arxiv:1203.5897 [math.DS].
13.V. Avrutin and M. Schanz, "On multi-parametric bifurcation in a scalar piecewise-linear map," *Nonlinearity*, vol. 19, no. 3, pp. 531–552, March 2006.

Proceedings, 5th Chaotic Modeling and Simulation International Conference, 12 – 15 June 2012, Athens Greece

Spatiotemporal chaos due to spiral waves core expansion

H. Sabbagh

American University of Iraq
E-mail: leosabbagh@excite.com

Abstract: In the framework of the Fitzhugh Nagumo kinetics and the oscillatory recovery in excitable media, we present a new type of meandering of the spiral waves, which leads to spiral break up and spatiotemporal chaos. The tip of the spiral follows an outward spiral-like trajectory and the spiral core expands in time. This type of destabilization of simple rotation is attributed to the effects of curvature and the wave-fronts interactions in the case of oscillatory damped recovery to the rest state. This model offers a new route to and caricature for cardiac fibrillation.

Keywords: Spiral break up, spatiotemporal chaos.

1. Introduction

Rotating spiral waves are ubiquitous in excitable media. They have been observed in chemical reactive solutions [1, 2], in slime-mold aggregates [3] and most importantly in cardiac muscle [4].Such wave patterns have been studied using reaction-diffusion equations models. For some values of the system control parameters, they undergo simple rigid rotation around a circular core. However, as the control parameter is varied, the spiral tip deviates from circular trajectories [5-11]. This non-steady rotation is known as meandering and it has been observed essentially in chemical systems such as in the Belouzov-Zhabotinsky (BZ) reaction [12]. Experiments with this reaction have also demonstrated spiral breakup [13, 14]. This later is of interest in cardiology since it is the prelude to cardiac fibrillation, the commonest cause of sudden cardiac death [15, 16], and has been observed in models that show wave trains spatiotemporal instabilities [17-18]. It is characterized by spatiotemporally chaotic or irregular wave patterns in excitable media and remains a challenging problem in nonlinear science.

We present in this paper a new type of meandering leading to spiral breakup and offering a new route to spatiotemporal irregularity or chaos in excitable media. Spiral core expansion occurs here as the spiral free end or tip follows an outward motion along a path that looks itself like a spiral. This core expansion was previously expected by the theory of non-local effects [6, 9, 10], and was attributed to effect of curvature on the velocity of propagation coupled to the effects of the interaction of successive wave-fronts due to refractoriness. The dependence of the normal velocity of propagation on curvature is given

by $v = v_0 - kD$, where k is the local curvature, D is the diffusion coefficient and v_0 is the plane wave velocity of propagation [11]. Due to this velocity gradient, small wavelength perturbations on the segments away from the tip would decay, which would stabilize wave propagation away from the tip and maintains the rotational motion of the spiral. On the contrary, perturbations straightening a small segment containing the tip would reduce curvature, and consequently the normal velocity of wave propagation is enhanced as the gradient of the normal velocity becomes weaker. This means that the tip would have a less tendency to curl but it tends to advance further. Therefore, further straightening of this segment containing the tip is expected. Thus, the spiral tip undergoes an outward forward motion instead of simple rigid rotation. If the recovery is non-oscillatory but monotonic, this destabilizing effect of curvature would be counteracted by the repulsive wave-front interaction due to the refractory period imposed on the medium after the passage of the preceding wave. In that case, circular rigid rotation would be sustained.

This outward motion of the tip along a spiraling trajectory was predicted by Ehud Meron in his theory of non-local effects [6, 10]. He proposed an approximate spiral wave solution of the reaction diffusion system in the form of a superposition of solitary wave-fronts parallel to each other, and then derived an evolution equation using a singular perturbation approach. The numerical solution of this equation, for the case of an oscillatory recovering excitable medium, was a spiral wave whose core expands in time and whose tip moves itself along a spiraling path. However, no observation of this type of spiral wave meandering and core expansion was obtained by Meron in reaction diffusion systems.

2. The Model

Here, we present a new model showing for the first time this predicted core expansion. We use a modified Barkley's model [19, 20] given by:

$$\partial u/\partial t = \frac{1}{\varepsilon} u(1-u)[u - ((b+v)/a)] + \nabla^2 u ,$$

$$\partial v/\partial t = u^3 - v , \qquad (1)$$

where u and v are the excitation and recovery variables respectively. The parameter b determines the excitation threshold. The inverse of ε, characterizing the abruptness of excitation, determines the recovery time. In the standard Barkley's model where the local kinetics in the second equation is given by $(u - v)$, propagation cannot be maintained upon increasing ε. Here propagation is maintained due to the delay in the production of v.
Numerical simulations were performed on square grids using the explicit Euler integration method with a 9-point neighborhood of the Laplacian and no-flux

boundary conditions. The space and time steps are respectively dx = 0.51 and dt = 0.052.

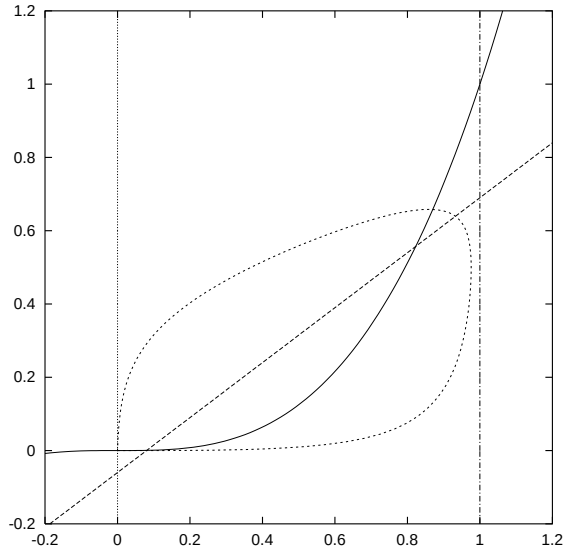

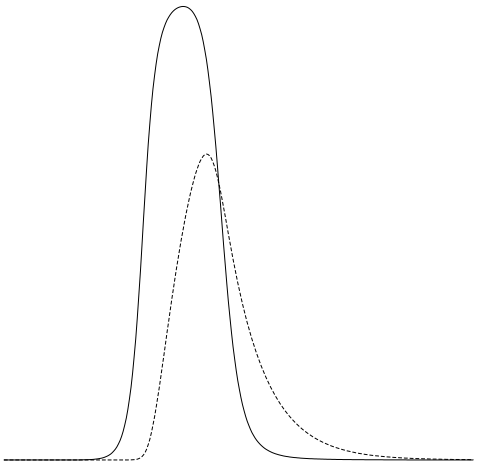

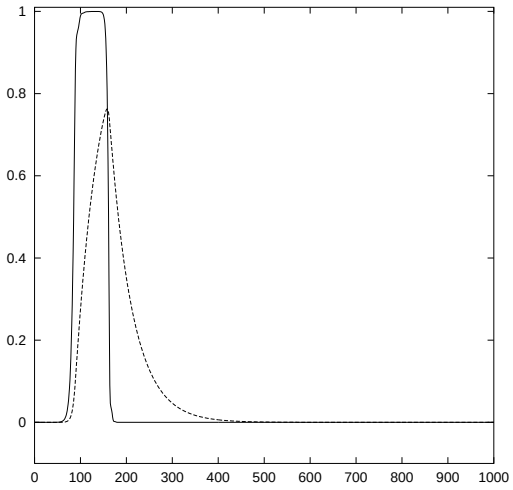
1
0.8
0.6
0.4
0.2
0
0
100
200
300
400
500
600
700
800
900
1000

```
ERROR: undefined
OFFENDING COMMAND:

STACK:
```

Proceedings, 5th Chaotic Modeling and Simulation International Conference, 12 – 15 June 2012, Athens Greece

Nanoindentation for Measuring Individual Phase Mechanical Properties of Sn-Ag-Cu Lead-Free Solders Incorporating Pileup Effects

Muhammad Sadiq, [1,2,3,5], Jean-Sebastien Lecomte, [4], Mohammed Cherkaoui, [1,2,3]

[1] George W. Woodruff School of Mechanical Engineering, Georgia Institute of Technology, 801 Ferst Drive NW, Atlanta, GA 30332, USA
[2] University of Lorraine, LEM3 UMR CNRS 7239, île du Saulcy, Metz 57045 France
[3] UMI 2958-Georgia Tech-CNRS Georgia Tech Lorraine, Metz 57070, France
[4] ENSAM-Arts et Métiers ParisTech, LEM3 UMR CNRS 7239, 4 rue Augustin Fresnel, Metz 57078 France
[5] msadiq3@gatech.edu

Abstract: Sn-Ag-Cu (SAC) alloys are considered as the best replacements of Sn-Pb alloys which are banned due to the toxic nature of Pb. But, SAC alloys have a coarse microstructure that consists of β-Sn rich and eutectic phases. Nanoindentation is a useful technique to evaluate the mechanical properties at very small length scale. In this work, CSM nanoindentation setup is used to determine the individual phase mechanical properties like Young's modulus and hardness at high temperatures. It is demonstrated that these properties are a function of temperature for both β-Sn rich and eutectic phases. Loadings starting from 500 μN upto 5000 μN are used with 500 μN steps and average values are presented for Young's modulus and hardness. The loading rates applied are twice that of the loadings. High temperatures results in a higher creep deformation and therefore, to avoid it, different dwell times are used at peak loads. The special pileup effect, which is more significant at elevated temperatures, is determined and incorporated into the results. A better agreement is found with the previous studies.

Keywords: SAC alloys, Nanoindentation, Young's modulus, Hardness, Pileup effects

1. Introduction

Good set of entire mechanical, electrical, chemical and thermal properties are the key elements before classifying any solder to be good for current solder joints. All of these properties were well set for Sn-Pb solder until no restrictions were taken by RoHS and Environmental Protection Agency (EPA), which identified Pb as toxic to both environment and health. This is because Pb and Pb-containing compounds, as cited by EPA, is one of the top 17 chemicals posing the greatest threat to human beings and the environment [1]. Moreover, current consumer demands and strict governmental legislations [2-4] are pushing the electronics industry towards lead-free solders.

Many lead-free solder alloys are studied by different researchers with wide range of applications. In Abtew's report [2], almost 70 lead-free solders are proposed to replace their lead based counterparts. Most of the newly defined

lead-free solders are binary and tertiary alloys [5], out of which, SAC tertiary alloys are considered as the best substitutes [6]. As like many other alloy systems, SAC has also certain limitation due to their coarse microstructure. Iron (Fe), cobalt (Co) and nickel (Ni) are used as potential additives to overcome these limitations [7]. In some studies, indium (In), bismuth (Bi), copper (Cu) and silver (Ag) are used as alloying elements [5]. Before classifying SAC as good substitute, extensive knowledge and understanding of the mechanical behaviour of this emerging generation of lead-free solders is required to satisfy the demands of structural reliability.

Electronic devices once subjected to severe conditions during service exposes solder joints to elevated temperatures. This causes significant evolution of the microstructure of SAC alloys. SAC alloys consists of β-Sn, eutectic Sn phases and Ag-Sn and Cu-Sn InterMetallic Compounds (IMCs). These IMCs are generally hard and brittle in nature which dictates the entire mechanical properties of the solder joints. Exposures to high temperatures causes thermal coarsening due to which the size of these IMCs grow and further deteriorate the solder joints and hence alters the structural reliability of the whole assembly. Rare-earth elements, known as the vitamins of metals, are used in different studies to control this thermal coarsening with significant results [8-11]. All these elements refine the grain size leading to a fine microstructure which ultimately improves the mechanical properties of SAC lead-free solders including yield stress and tensile strength [10-11].

The fast introduction of lead-free solders without deep knowledge of their behaviour has caused many problems in the current electronics industry. Therefore, good understanding of SAC alloys is required to explore the mechanical properties and enhance the solder joint reliability. The main focus of this work is to measure the individual phase properties like Young's modulus and hardness of SAC alloys for eutectic Sn and β-Sn phases. Many researchers have already attempted to determine the mechanical properties of Sn-Ag and SAC alloys [12-13]. The indenter causes piling up inside the soft Sn-matrix which has been neglected in many studies which makes the results unreliable. In this study, the piling up effect is considered for both phases and evaluated using semi-ellipse method and incorporated into results. Both results, before modification and after modification are provided for comparison.

2. Experimental

Solder alloy used in this study is Sn3.0Ag0.5Cu with 96.5 wt % of Sn, 3 wt % of Ag and 0.5 wt % of Cu. Since sample preparation for any kind of experimental study is crucial. Therefore a casting die is used to make the samples using "cast by melt" process with many advantages. This die gives almost final shape to the samples with minimum of final machining required. Almost voids-free surface is achieved which is very important for the nanoindentation testing. During casting the microstructure of the testing samples is controlled using specified cooling rate which is about 3°C/s. A temperature of 260°C was kept in the oven and the die was heated for about 45 minutes before

putting the molten metal into it. The 200g ingots were put in a crucible and then placed in the oven at 260°C for about 25 minutes. Water at a temperature of 15°C was used for quenching; the cooling rate of the specimens was measured with a K-type thermocouple. Only a small part of the die was dipped in the water to get a slow cooling rate of about 3°C/s, which is close to the actual soldering process. The dog-bone shape specimen is shown in Figure 1 with a thickness of 2mm.

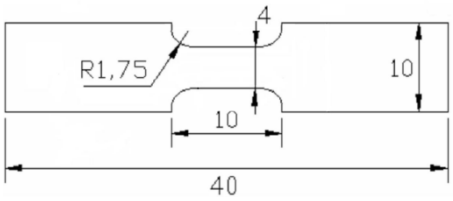

Fig. 1. Dog-bone specimen (all dimensions in mm)

Specimens were mechanical polished with silicon discs and 1 micron diamond paste. Chemical etching was performed for a few seconds using a 5% hydrochloric acid and 95% ethanol solution in order to distinguish between different phases. Figure 2 shows an SEM micrograph and Optical microscope (OM) micrograph taken before the nanoindentation. An Oxford EDS system placed in the SEM enabled to realize elemental mappings for every specimen.

Nanoindentation tests were carried out by using a nanoindenter XP equipped with a Berkovich-84 diamond indenter. The resolutions of the loading and displacement systems are 50 nN and 0.01 nm, respectively. Both of the standard deviation errors of the measured hardness and reduced modulus values for the standard are well less than 1%. The hardness value and reduced modulus values were also extracted from the unloading part of load–depth curves by using Oliver and Pharr method [14].

An acquisition frequency was 10 Hz and poison ratio, assumed, was 0.33. The load applied were 100 μN to 5000 μN with steps of 500 μN. The loading and unloading rates (mN/min) were two times that of load applied (mN). An approach speed of 3000 μN/min was used. As the lead free solders exhibit severe creep deformation, even at room temperature [15], the dwell time at the peak load is defined as 60 seconds in order to completely relieve the creep deformation and also avoid the famous “bulge” or “nose” effect during unloading [16].

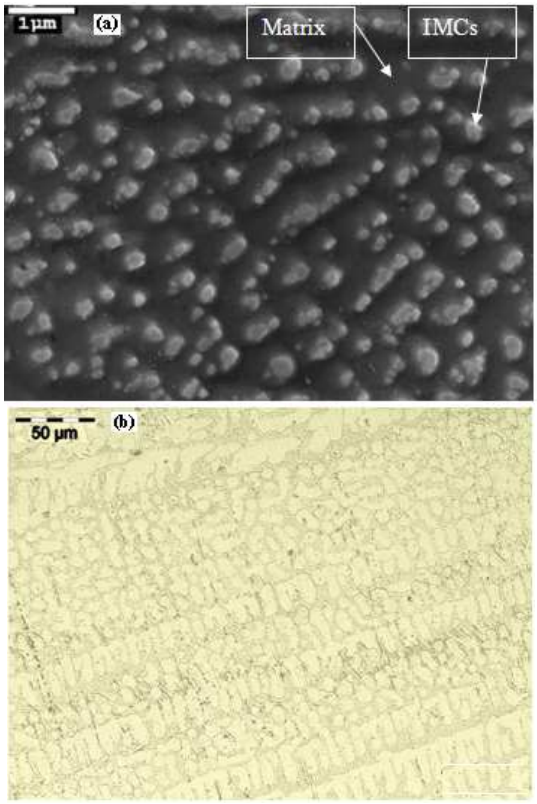

Fig. 2. (a) SEM and (b) Optical Microscope micrographs before nanoindentation

The selection of position to indent was controlled under a high-resolution Optical Microscope (OM), by which various phases can be distinguished. OM was also applied after the indentation to confirm the indenter location and avoid the grain boundary effects. For each specimen, 9 points (3X3 arrays) were tested. Both phases, eutectic and β-Sn, were selectively indented by the visual matrix method. Same tested zones were studied after the indentation testing with Atomic Force Microscope (AFM).

Afterwards, Scanning Electron Microscope (SEM) and Energy Dispersive Spectroscopy (EDS) were used to confirm the chemical composition of each phase. Further, because the Young's modules and hardness for each phase is different, curves for eutectic phase and β-Sn phase can be distinguished from the test array.

3. Results and discussion

This is well known in the nanoindentation testing that the typical load-depth curve has significant importance for extracting the overall results. Most

importantly, the slope of the unloading portion of the curve is used in almost all calculations. As discussed earlier, SAC alloys are famous for their low creep resistance and hence quite vulnerable to creep, due to which the pile-up effects happens which causes the "bulge effect" in both β-Sn and eutectic-Sn phases. It is important to avoid this "bulge effect" as it may alter the credibility of final results. Different loads were tested to avoid this effect but it still exists as shown in Figure 3.
Moreover, in order to investigate the creep effects on the mechanical properties, different holding times were used. In comparison to Sn matrix, the IMCs are expected to be resistant to the creep effect. In some cases, there is some bulge effect, but it can be concluded that this is because of the Sn matrix in which these particles are finally embedded.

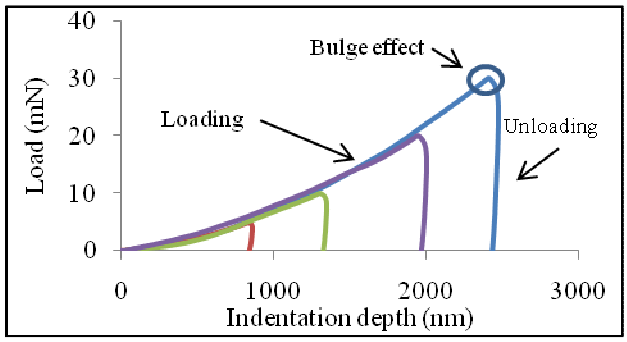

Fig. 3. Load-displacement curves with no holding time

Both β-Sn and eutectic Sn phases were subjected to indentation testing. The load-time history for the entire testing is shown in Figure 4.At a peak load of 5000μN, a 60 seconds dwell time was used to avoid the bulge effect. Solder joints are exposed to high temperatures during service. This causes thermal coarsening of IMCs, due to which, their size grows as the diffusion rate of Ag and Cu into Sn increases at elevated temperatures. It is of utmost importance to understand and explore the individual phase mechanical properties up to a homologues temperature of at least $0.4T_m$, where T_m is the melting point of SAC alloy.
The Load-Depth curves for individual phases at 20°C, 45°C and 85°C are given in Figures 5-7 respectively. In this case, the bulge effect is negligible. Quite useful information can be extracted from these curves. It is important to visualize that the elastic deformation in both phases is quite small which makes the unloading curve almost straight (vertical). Moreover, as also described by the other researchers, indentation depth in eutectic phase is significantly smaller than the β-Sn phase [15]. This effect was also confirmed when the hardness of both phases were compared, eutectic phase being harder than β-Sn phase. This could be the effect of diffusion of Ag and Cu in Sn in the eutectic zone. For confirmation of the testing zone, the tested specimens were taken under the AFM. High resolution images were collected as provided in Figure 8 for the

testing performed over eutectic zone in SAC alloy. Different size of indentation represents different loadings applied during testing.

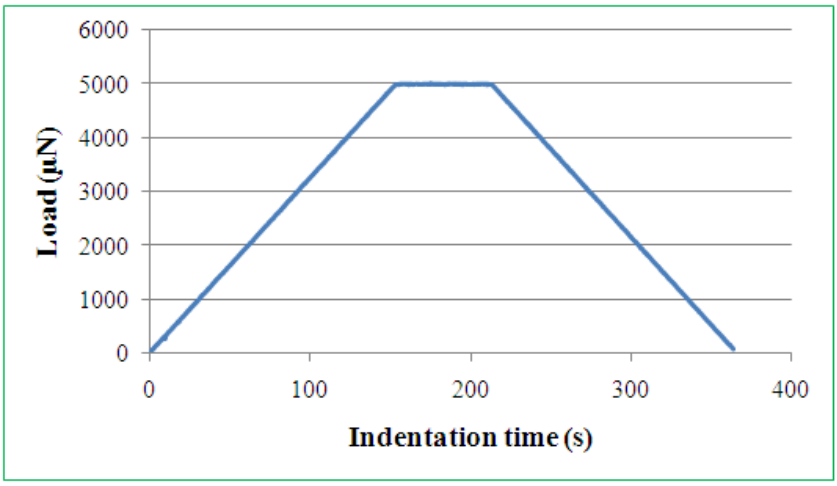

Fig. 4. Load-time history during indentation testing with 60 seconds dwell time

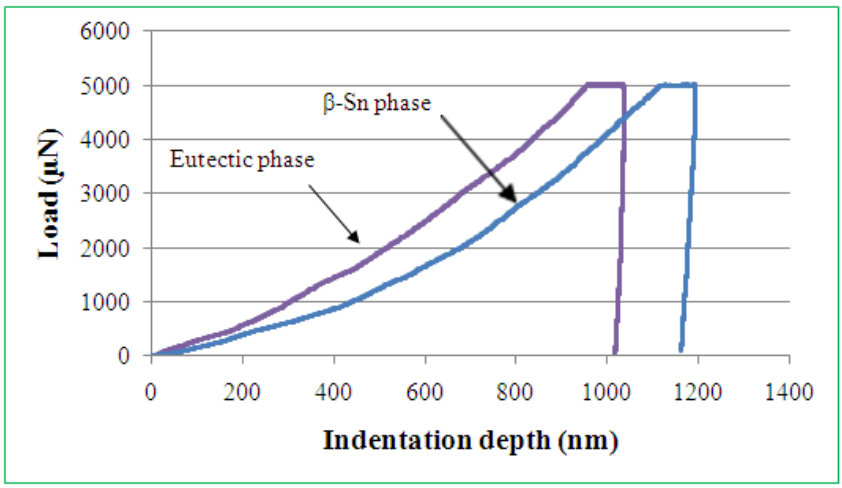

Fig. 5. Load-displacement curves for Eutectic and β-Sn phases at 20°C

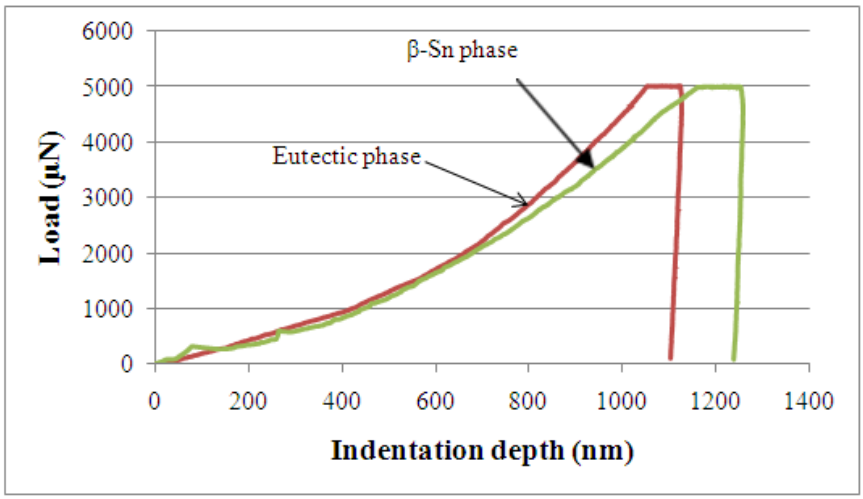

Fig. 6. Load-displacement curves for Eutectic and β-Sn phases at 45°C

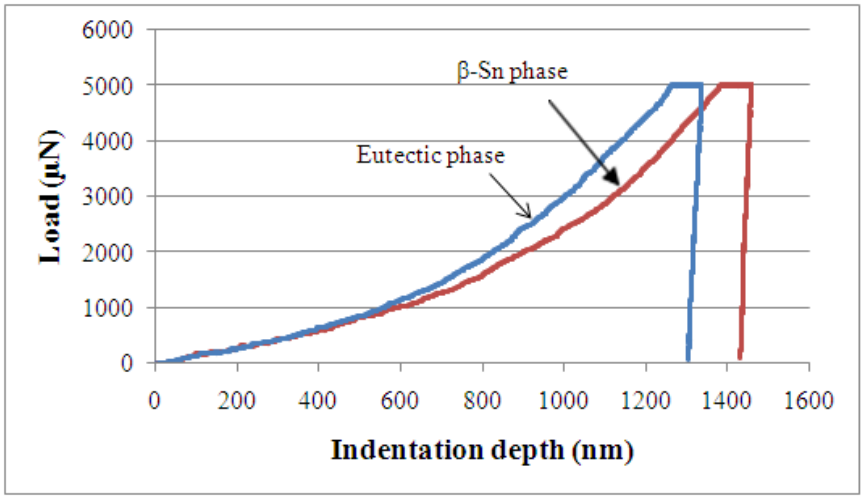

Fig. 7. Load-displacement curves for Eutectic and β-Sn phases at 85°C

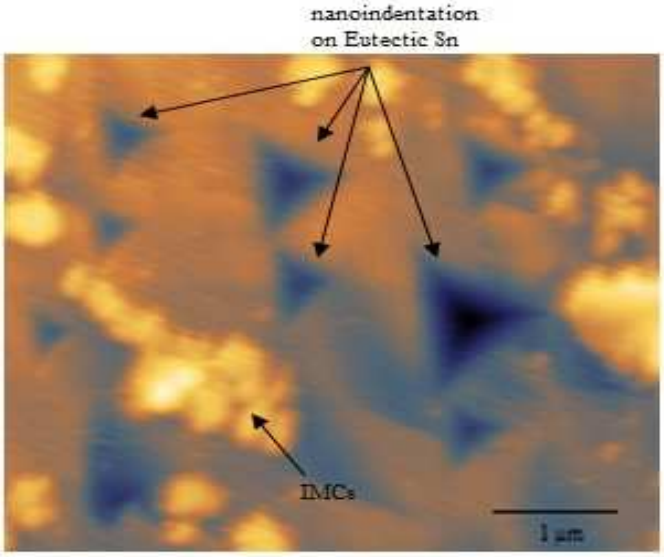

Fig. 8. AFM image after nanoindentation over eutectic zone

3. Oliver and Pharr Model

Oliver and Pharr Model (OPM) is extensively used for the solder alloys [14]. Both Young's modulus and hardness are easily extracted using OPM after calculating the reduced modulus E_r as described in equation (1),

$$\frac{1}{E_r} = \frac{\sqrt{\pi}}{2\beta} \cdot \frac{S}{\sqrt{A_{op}}} \quad \text{.....(1)}$$

where S is the contact stiffness calculated from the slope of the unloading portion of the curve, β is a constant related to the geometry of the indenter, and A_{op} is the oliver-pharr area projected during indentation. At the same time, the reduced Young's modulus could be formulated as,

$$\frac{1}{E_r} = \frac{1-v^2}{E} + \frac{1-v_i^2}{E_i} \quad \text{.....(2)}$$

where E and υ are the Young's modulus and Poisson's ratio of the tested material and E_i, υ_i are the Young's modulus and Poisson's ratio for the diamond tip. The values of E_i and υ_i used in this study were 1141 GPa and 0.07, respectively as used in most of the studies [8] and the Poisson's ratio of each phase, i.e., β-Sn and eutectic Sn phase was approximated to be 0.33 which was consistent with the previous studies [8]. Hardness (H) of the material, on the other hand, can be determined by (3) where F_{max} is the peak indentation load and A_{op} is the projected contact area

$$H = \frac{F_{\max}}{Aop} \text{.....(3)}$$

$$A_{op} = 24.5h_c^2 + \sum_{i=1}^{8} C_i h_c^{\frac{1}{2i}} \text{.....(4)}$$

Table I. Constant "C" values for berkovich-BK indenter tip

C_0	C_1	C_2	C_3	C_4	C_5
24.5	10.31	-16.03	24.45	-7.32	5.12

where C is the constant depending on the indenter type and shape and are given in Table I for Berkovich-BK indenter tip. h_c is the contact depth which is smaller than the theoretical depth due to the sinking effect of the specimen under indenter.

Both Young's modulus and hardness are determined and provided for eutectic and β-Sn phases in Table II. These are the results before pile-up effects. Almost no change was investigated with varying loading and loading rates. This is consistent with other studies [15].

Table II. Individual phases Young's modulus and hardness before pileup effects

Phase	Young's modulus (Gpa)	Hardness (Gpa)
Eutectic-Sn	60±3	0.35±0.04
β-Sn	54±4	0.30±0.045

4. Pileup area calculations

Assuming that the projected contact area, A_c, determined at contact depth, hc, traces an equilateral triangle of side b, then for a perfect Berkovich tip,

$$A_c = 24.56h_c^2 \text{.....(5)}$$

There are semi-elliptical portions at each side of the triangle as shown in Figure 9. The area of each semi-elliptical pile-up projected contact area is $\frac{\pi b}{4} a_i$ and the total pile-up contact area is, therefore,

$$A_{pu} = \frac{\pi b}{4} \sum a_i \text{.....(6)}$$

where the summation is over three semi-elliptical projected pile-up lobes and a_i being the measurement of piling up width on three surface (sides) of the equilateral triangles [2]. The AFM images are analyzed in image-plus to trace the surface profiles and are given in Figure 10. Knowing then the contact area from the Oliver–Pharr method, the total or true contact area for an indent can be obtained as:

$$A = 24.5h_c^{\,2} + \sum_{i=1}^{8} C_i h_c^{\frac{1}{2i}} + \frac{\pi b}{4}\sum a_i .....(7)$$

Incorporating this new pileup area into the original OPM as presented in equations (1) and (3) becomes,

$$\frac{1}{E_r} = \frac{\sqrt{\pi}}{2\beta}\cdot\frac{S}{\sqrt{A_{op} + A_{pu}}} .....(8)$$

$$H = \frac{F_{\max}}{A_{op} + A_{pu}} .....(9)$$

The hardness and indentation modulus measured for eutectic and β-Sn phases are shown in Table III after incorporating the pileup effects. These results are in a better agreement with the previous studies [12]. This collection of data allows for comparison of mechanical properties of different phases, where all of the samples were prepared and tested in the same manner.

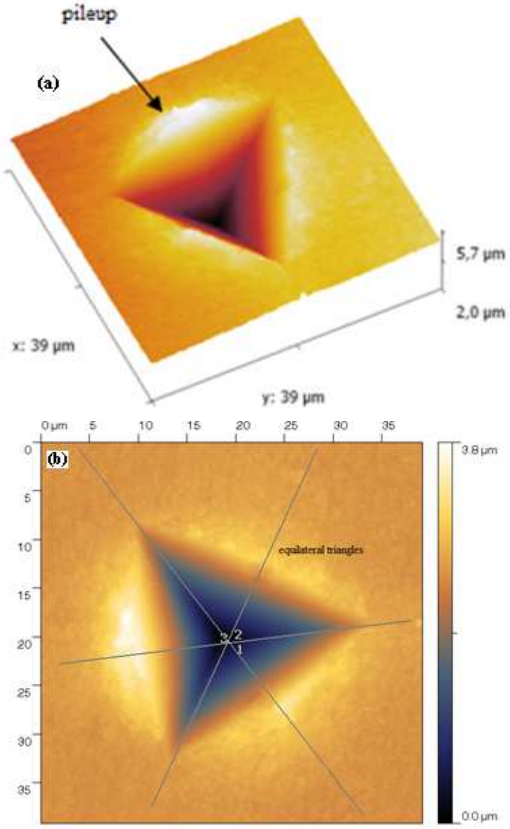

Fig. 9. (a) Pileup schematic and (b) equilateral triangles after testing

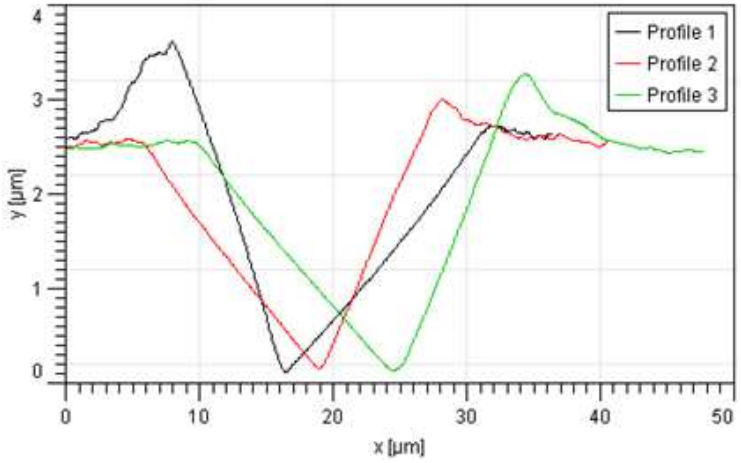

Fig. 10. Pileup profiles for equilateral triangles

Table III. Young's modulus and hardness after pileup effects

Phase	Young's modulus (Gpa)	Hardness (Gpa)
Eutectic phase	49±2	0.25±0.05
β-Sn phase	45±3	0.20±0.06

Both Young's modulus and hardness were also determined along the indentation depth with experiencing only small variations which is also consistent with [12]. The average values for the Young's modulus for eutectic phase, along the indentation depth, are determined to be 51 GPa whereas for β-Sn it is 48 GPa. Similarly, the average values for hardness, along the depth, for eutectic phase are determined to be 0.26 GPa whereas for β-Sn it is 0.22 GPa. The average values are taken from 100 nm to 500 nm depth. These values are taken after considering the pileup effects.
Similarly, summarized results for β-Sn and eutectic phases for Young's modulus and hardness at elevated temperatures are given in Tables IV-V respectively.

Table IV. Mechanical properties for β-Sn phase at different temperatures

Temperature (° C)	Young's modulus (GPa)	Hardness (GPa)
45	37.42 ±2.1	0.10 ±0.03
65	36.21 ±3.2	0.095 ± 0.025
85	34.85 ±3.5	0.087 ± 0.027

Table V. Mechanical properties for Eutectic phase at different temperatures

Temperature (°C)	Young's modulus (GPa)	Hardness (GPa)
45	42.83 ±2.7	0.19 ±0.040
65	43.72 ±2.2	0.17 ± 0.025
85	51.85 ±4.5	0.11 ± 0.027

Like the other phases of SAC alloys, the nanoindentation setup is also used for IMCs. These IMCs are hard and brittle as compare to the other phases in the same specimens. The EDS elemental mapping is used to verify the compositions of these IMCs before implementing the nanoindentation.
The AFM micrograph is given in Figure 11 in which the indentation is carried out on IMCs. These images are collected just after the indentation process. The results for Young's modulus and hardness for both Ag_3Sn and Cu_6Sn_5 IMCs are provided in Table VI, with good comparison to the previous studies [17]. This is important to mention that the pileup effect is very small for these particles which is consistent with previous studies and therefore is neglected for IMCs.

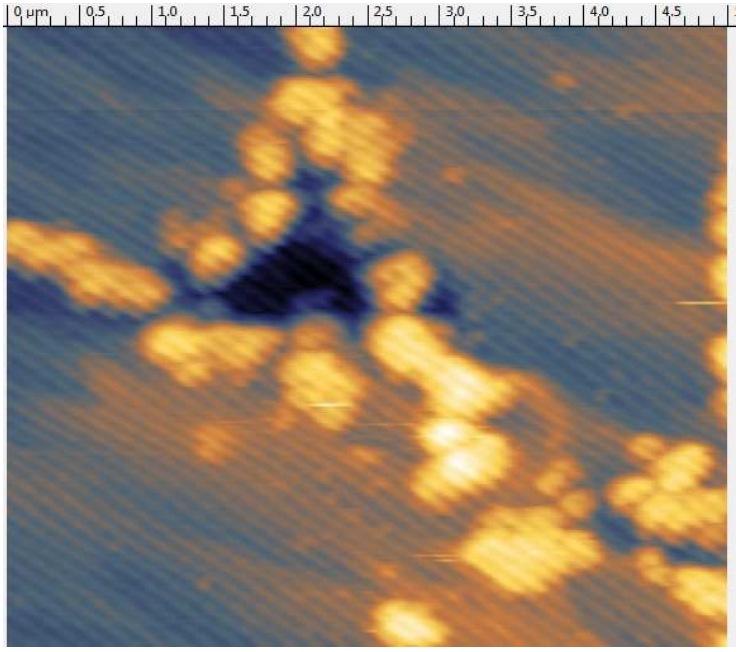

Fig. 11. AFM image for nanoindentation over IMCs

Table VI. Mechanical properties for IMCs

IMCs	Young's Modulus (GPa)	Hardness (GPa)
Ag_3Sn	74 ± 3	3.32 ± 0.2
Cu_6Sn_5	91 ± 5	5.8 ± 0.6

5. Conclusions

A detailed study was carried out to explore the individual phase mechanical properties using nanoindentation for the SAC alloy which is considered as potential substitute for SnPb solder. Varying loads and loading rates were used to avoid the typical "bulge effects" and hence make the results more reliable. Piling effect, already ignored by many researchers, is calculated and incorporated into the Oliver-Pharr model. Image-Plus software is used to treat the indentation images taken with AFM after testing and hence plot the individual surface profiles to better explain the material behaviour. It is concluded that this pileup area play a major role in calculating the real results particularly for the soft Sn phase which has more pileup than the eutectic phase. Young's modulus and hardness were also determined along the indentation depth and almost no change was observed which is consistent with previous studies. Different temperatures are used and the load-depth curves are plotted for individual phases. It is noticed that both Young's modulus and hardness reduces with increasing temperatures for both phases.

References

1. E.P. Wood, K.L. Nimmo, "In search of new lead-free electronic solders" *J. Elect. Mat.* Vol. 23 No. 8 (1994) 709–713
2. Y. Sun et al. "Nanoindentation for measuring individual phase mechanical properties of lead free solder alloy" *J. Mat. Sci: Mater Electron* 19: (2008) 514–521
3. K.N. Tu, A.M. Gusak, M. Li, "Physics and materials challenges for lead-free solders" *J. Appl. Phys.* Vol. 93 No. 3, (2003) 1335-1353
4. M. Abtew, G. Selvaduray, "Lead-free solders in microelectronics" *Mater. Sci. Eng.* Vo. 27 No. 5 (2000) 95-141
5. D. Q. Yu, J. Zhao, L. Wang, "Improvement on the microstructure stability, mechanical and wetting properties of Sn-Ag-Cu lead-free solder with the addition of rare earth elements" *J. alloys and compounds* Vol. 376 No. 1-2 (2004) 170-175
6. M. A. Rist, W. J. Plumbridge, S. Cooper, "Creep-constitutive behavior of Sn-3.8Ag-0.7Cu solder using an internal stress approach" *J. Elect. Mat.* Vol. 35, No. 5 (2006) 1050-1058
7. I. E. Anderson et al. "Alloying effects in near-eutectic Sn-Ag-Cu solder alloys for improved microstructural stability" *J. Elect. Mat.* Vol. 30 No. 9, 2001, 1050-1059
8. Anon, "Rare-Earth solders Make Better Bounds", *Photonics Spectra,* Vol. 36, No. 5 (2002), 139
9. M. Pei and J. Qu, "Effect of Lanthanum Doping on the Microstructure of Tin-Silver Solder Alloys" *J. Elect. Mat.* Vol. 37 No. 3 (2008) 331-338

10. X. Ma, Y. Qian, F. Yoshida, "Effect of La on the Cu-Sn intermetallic compound (IMC) growth and solder joint reliability" *J. alloys and compounds,* Vol. 334 No. 1-2 (2002), 224-227
11. C. M. L. Wu, Y. W. Wong, "Rare-earth additions to lead-free electronic solders" *J. Mater Sci. Mater Electron* Vol. 18 No. 1-3 (2007) 77–91
12. X. Deng, et al., "Deformation behavior of (Cu, Ag)-Sn intermetallics by nanoindentation" *Acta Mater.* Vol. 52 No. 14, (2004) 4291-4303
13. H. Rhee, J.P. Lucas, K.N. Subramanian, "Micromechanical characterization of thermomechanically fatigued lead-free solder joints" *J. Mater. Sci. Mater. Electron.* Vol. 13 No. 8 (2002), 477-484
14. W.C. Oliver, G.M. Pharr, "An improved technique for determining hardness and elastic modulus using load and displacement sensing indentation experiments" *J. Mater. Res.* Vol. 7 No. 6 (1992) 1564–1583
15. Gao F., Takemoto T., "Mechanical properties evolution of Sn-3.5Ag based lead-free solders by nanoindentation" *Materials Letters* Vol. 60 No. 19 (2006) 2315–2318
16. *Y.T. Cheng, C.M. Cheng,* "Scaling, dimensional analysis, and indentation measurements" *Mater. Sci. Eng. R Rep.* 44 (2004) 91-149
17. R. R. Chromik, R. P. Vinci, S. L. Allen and M. R. Notis "Nanoindentation measurements on Cu–Sn and Ag–Sn intermetallics formed in Pb-free solder joints" *Journal of Materials Research* 18 (2003), 2251-2261

Proceedings, 5th Chaotic Modeling and Simulation International Conference, 12 – 15 June 2012, Athens Greece

Poincaré Analysis of Non-linear Electromagnetic Modes in Electron-Positron Plasmas

V. Saxena and I. Kourakis

Centre for Plasma Physics, School of Mathematics and Physics,
Queen's University Belfast BT7 1NN , Northern Ireland, UK

Email : v.saxena@qub.ac.uk

Abstract : We present an investigation of coupled nonlinear electromagnetic modes in an electron-positron plasma by using the well established technique of Poincaré surface of section plots. A variety of nonlinear solutions corresponding to interesting coupled electrostatic-electromagnetic modes sustainable in electron-positron plasmas is shown on the Poincaré section. A special class of localized solitary wave solution is identified along a separatrix curve and its importance in the context of electromagnetic wave propagation in an electron-positron plasma is discussed.
Keywords : Poicaré section, solitary, electron-positron plasma

1.Introduction

The method of Poincaré surface of section (SOS) plots has been very useful in analysing higher dimensional non-linear dynamical systems [1]. For a given n-dimensional continuous dynamical system, the corresponding Poincaré SOS plot represents an equivalent discrete dynamical system with (n-1) dimensions and thus facilitates the analysis of possible periodic, quasi-periodic and chaotic modes, the original system can sustain. As non-linearity in plasmas is inherent they provide a perfect paradigm to study various non-linear processes ranging from coherent solitary waves to chaos and turbulence. In this respect, the subject of intense laser plasma interactions has ever received a great deal of attention. There has recently been a resurgence in this research area after the efficient production of very intense laser pulses ($I \geq 10^{18} W/cm^2$) has become a reality [2]. Laser pulses with such high intensities are called relativistically intense as the associated transverse electric fields are strong enough to drive the electrons to relativistic speeds. From theoretical point of view, these high intensity laser plasma interactions provide a favourable environment for a whole range of non-linear processes. Among them the formation of electromagnetic solitary wave is a topic of much fundamental interest particularly in theoretical plasma physics. There have been several theoretical investigations addressing the existence and stability of coupled electromagnetic solitary waves in plasmas [3].

On the other hand, the electron-positron plasmas are thought to be a constituent of various astrophysical environments e.g. in pulsar magneto-spheres, in bi-polar flows in active galactic nuclei (AGN) and at the centre of our galaxy and are believed to be the first state of matter in the early stage of universe [4,5]. The coupling of electromagnetic waves to electron-positron plasmas is therefore an active area of theoretical research and has been addressed in few earlier works [5]. We present here a detailed Poincaré section based analysis of a class of possible coupled non-linear electromagnetic modes in an un-magnetized electron positron plasma with a particular emphasis on the coupled solitary waves solutions. This work is an extension of earlier works by Saxena et al. [7] and O. B. Shiryaev [6]. We adopt the same formalism as used by Kaw et al. [8] for an electron plasma with ions forming a neutralizing background.

2.Mathematical Model

The coupling of a relativistically intense electromagnetic wave with an electron-positron plasma is described by the following set of coupled fluid-Maxwell equations.

$$A_{xx} - A_{tt} = \left(\frac{n_e}{\gamma_e} + \frac{n_p}{\gamma_p} \right) A \tag{1}$$

$$\phi_{xx} = n_e - n_p \tag{2}$$

$$\left(p_{e,p} \right)_t = \left(\phi - \gamma_{e,p} \right)_x \tag{3}$$

$$\left(n_{e,p}\right)_t + \left(\frac{n_{e,p}\, p_{e,p}}{\gamma_{e,p}}\right)_x = 0. \tag{4}$$

Here indices e and p stand for electron and positron species respectively, A, Φ, $n_{e/p}$, and $p_{e/p}$ respectively represent the electromagnetic vector potential, electrostatic potential, the electron/positron density and electron/positron longitudinal momentum. $\gamma_{e,p}$ Is the relativistic factor given by,

$$\gamma_{e,p} = \sqrt{1 + |A|^2 + p_{e,p}^2} \tag{5}$$

By performing a co-ordinate transformation defined as $\xi = x - \beta t$ where $\beta = v_{ph} / c$ is the normalized phase velocity, one obtains following set of coupled non-linear ordinary differential equations.

$$\left(\beta^2 - 1\right)a_{\xi\xi} + \left(\frac{\beta}{\sqrt{\left(\beta^2-1\right)\left(1+a^2\right)+\left(1+\phi\right)^2}} + \frac{\beta}{\sqrt{\left(\beta^2-1\right)\left(1+a^2\right)+\left(1-\phi\right)^2}}\right)a = 0 \tag{6}$$

and

$$\phi_{\xi\xi} + \frac{1}{\left(\beta^2-1\right)}\left(\frac{\beta\left(1+\phi\right)}{\sqrt{\left(\beta^2-1\right)\left(1+a^2\right)+\left(1+\phi\right)^2}} + \frac{\beta\left(1-\phi\right)}{\sqrt{\left(\beta^2-1\right)\left(1+a^2\right)+\left(1-\phi\right)^2}}\right) = 0 \tag{7}$$

Now making a change of variable defined by

$$\left(\beta^2-1\right)^{1/2} a = X$$

$$1 + \phi = -Z$$

$$\frac{\xi}{\left(\beta^2-1\right)^{1/2}} = \xi'$$

we get following set of simplified equations,

$$\ddot{X} + \beta\left[\frac{1}{\sqrt{\beta^2 - 1 + X^2 + Z^2}} + \frac{1}{\sqrt{\beta^2 - 1 + X^2 + \left(Z+2\right)^2}}\right]X = 0 \tag{8}$$

$$\ddot{Z} + \beta\left[\frac{Z}{\sqrt{\beta^2 - 1 + X^2 + Z^2}} + \frac{\left(Z+2\right)}{\sqrt{\beta^2 - 1 + X^2 + \left(Z+2\right)^2}}\right] = 0 \tag{9}$$

Above coupled equations (8) and (9) admit following constant of motion:

$$H = \frac{1}{2}\dot{X}^2 + \frac{1}{2}\dot{Z}^2 + \beta\left[\sqrt{\beta^2 - 1 + X^2 + Z^2} + \sqrt{\beta^2 - 1 + X^2 + \left(Z+2\right)^2}\right] \tag{10}$$

This problem is similar to that of coupled oscillators in Hamiltonian mechanics with two degrees of freedom and we solve above set of equations (8-10) using Runge-Kutta 4th order integration method to obtain coupled non-linear solutions.

3. Non-linear Solutions on Poincare Surface of Section

We consider the case of $\beta > 1$ and show the possible solutions on a Poincaré SOS plot defined by $X = 0, \dot{X} > 0$. We have investigated two interesting regimes $\beta - 1 << 1$ and $\beta - 1 \leq 1$. The results are shown in Fig.1 and Fig.2 respectively. It is worth noting that in the regime of phase velocities close to the speed of light, there exist a more varied class of solutions. The Poincaré plot in Fig.1 is obtained for $\beta = 1.001; H = 10$. The densely filled curves correspond to quasi periodic solutions with the ratio of the frequencies of two oscillators being a prime number. The centres of the left and right halves of the Poincaré plot represent the fixed points of zero measure and correspond to periodic orbits. The interesting island curves correspond to amplitude modulated quasi periodic modes whereas centres of these islands represent the fixed points of higher orders and correspond to periodic waves with an integer ratio of the two oscillator's frequencies. We note that the separatrix curve is not quite periodic and therefore indicates a possibility of slightly chaotic solutions.

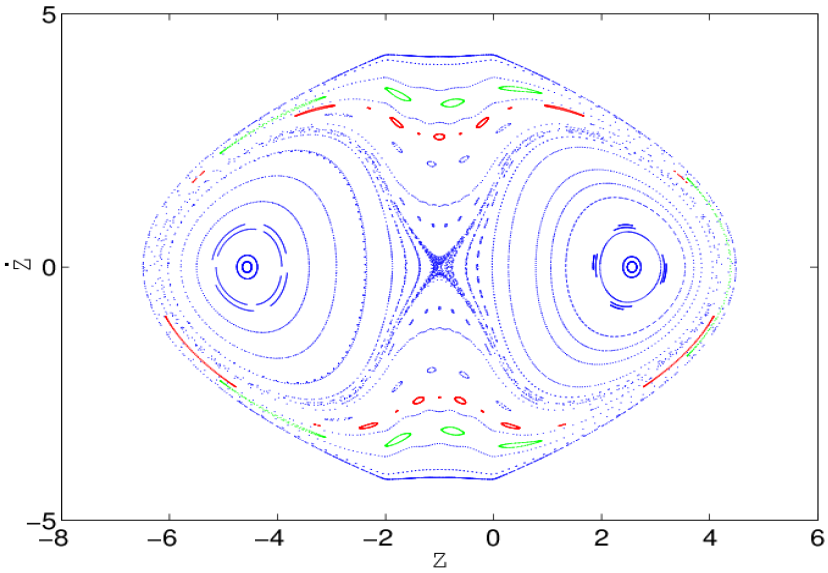

Fig.1 : Poincaré section plot for parameters β=1.001, H=10.

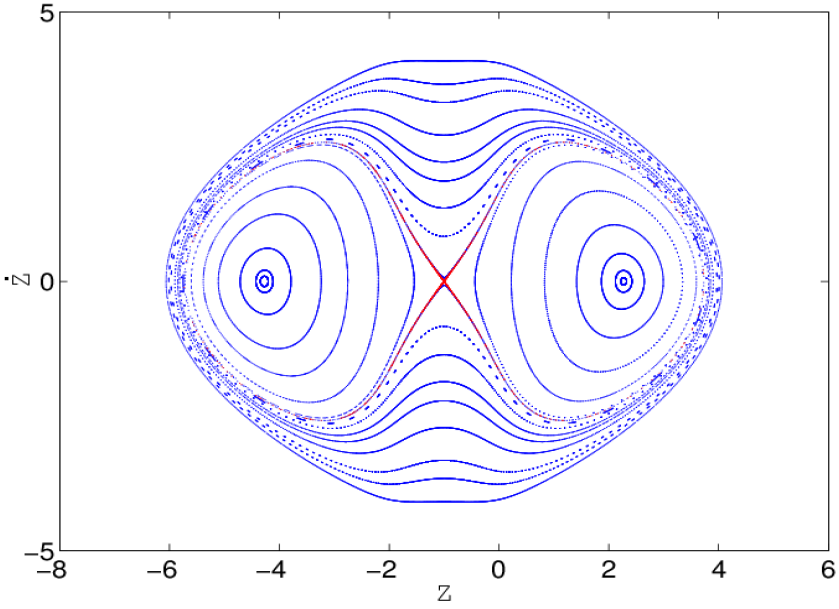

Fig.2 : Poincaré section plot for parameters β=1.1, H=10.

Now in the regime of $\beta - 1 \leq 1$, we choose the parameters to be $\beta = 1.1; H = 10$. The Poincaré surface of section plot for this case is shown in Fig.2. In this case we observe that the small island curves cease to exist. Moreover, there exists a sharp separatrix curve. This separatrix curve corresponds to localized solitary wave solutions. We show this particular solution in Fig.3.

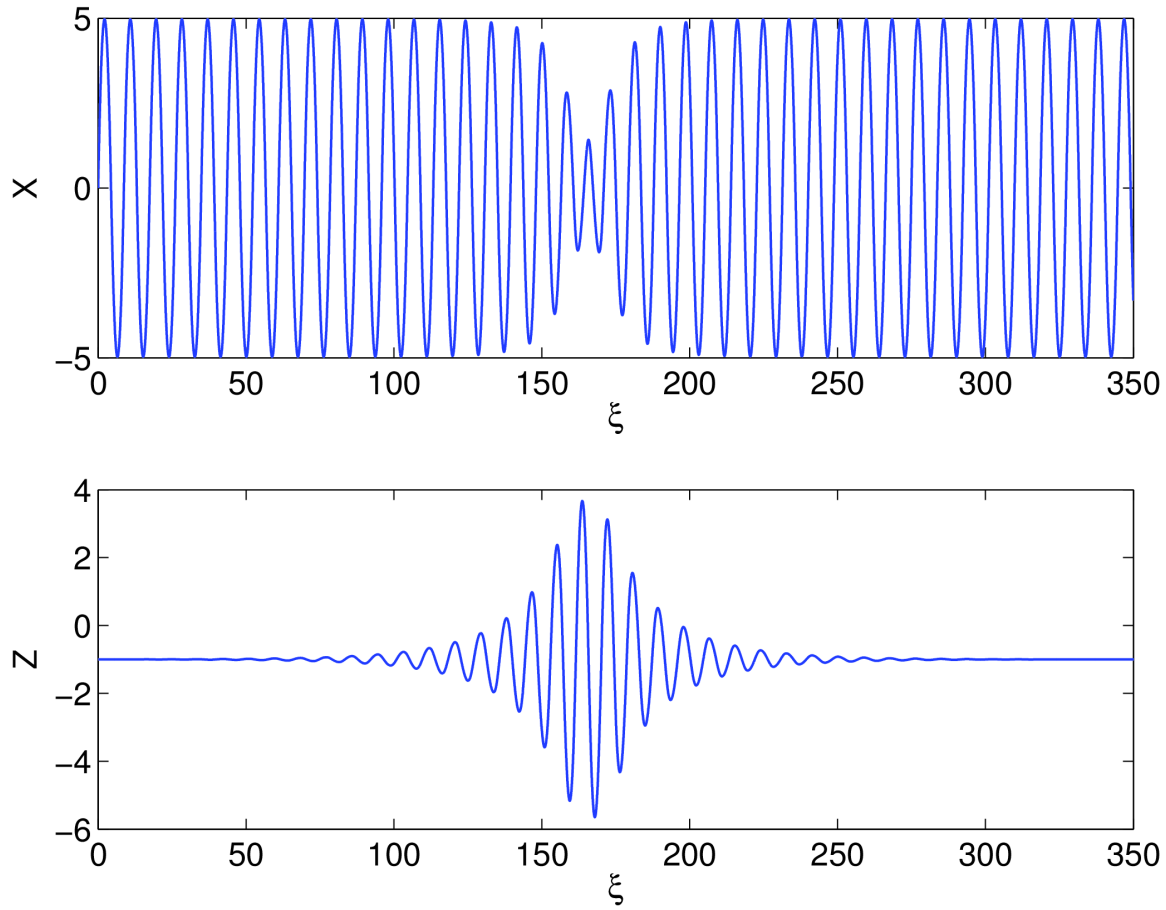

Fig.3 : Solitary solution corresponding to the separatrix curve in Fig.2.

4. Conclusions

To conclude, we have presented a class of coupled non-linear electromagnetic solutions for electromagnetic wave propagation in an electron-positron plasma by using Poincaré surface of section technique. A special class of solitary wave solutions has been identified along the separatrix curve in a parameter regime with phase velocities exceeding the speed of light by ~ 10% or more. These solitary modes play an important role in the energy localization in laser plasma interactions and therefore their stability needs to be understood which is an open area of research.

5. Acknowledgements

The authors gratefully acknowledge funding from the UK EPSRC (Engineering and Physical Science Research Council) via grant EP/I031766/1 (VS) and also (IK) via grant EP/D06337X/1.

References

1. H. Poincaré 1892 *Les methods nouvelles de la mechanique celeste* (Paris: Gauthier-Villars)
2. G. Mourou and D. Umstadter, Phys. Fluids B, vol.4, 2315 (1992).
3. V. Saxena et al., Phys. Plasmas, vol. 14, 072307 (2007) *and references therein*.
4. F.C. Michel, Rev Mod. Phys., vol. 54,1 (1982).
5. M.C. Begelman et al., Rev. Mod. Phys., vol 56, 255 (1984).
6. O.B. Shiryaev, phys. Plasmas, vol 13, 112304 (2006) *and references therein.*
7. V. Saxena, A. Sen, and P. Kaw, Phys. Rev. E, vol 80, 016406 (2009).
8. P.K. Kaw, A. Sen, and E.J. Valeo, Physica D, vol 9, 96 (1983).

Proceedings, 5th Chaotic Modeling and Simulation International Conference, 12 – 15 June 2012, Athens Greece

PROCESS AUTOMATION: UNDERRUN PROTECTION DEVICE ANALYSIS PER REGULATION

Uday Sherikar

VIT University, Vellore, Tamil Nadu, India
E-mail: uday.cadcam@gmail.com

Abstract: The report explores Process Automation Tool developed using Altair Hyper Works Process Manager to automate UPD analysis, post processing of it and plotting the results. Such a tool assists CAE analysis engineer to capture best practices for CAE model building. It also helps to reduce simulation development cycle time, increases the quality, eliminates repetitive tasks and also maintain the consistency in results.
The process template is developed to automate Front under-run protection device (FUPD), Rear under-run protection device (RUPD) and Side under-run protection device (SUPD) for RADIOSS solver. The FUPD, RUPD and SUPD are required to comply with ECE R93, ECE R58 and ECE R73 regulations, which provides strict requirements of devices design and its behavior under loading, that's the need to be fulfilled by device for approval of load carrying vehicles. The practical testing of under-run protection device (UPD) is very difficult, time consuming and costly. Also for any organization, to sustain in competition, product lead time to launch the new vehicle in market will be as minimum as possible. This causes increase in importance of computational simulation. But to get correct computational results, proper simulation method is essential.

Keywords: ECE R93, ECE R58, ECE R73, UPD, Process template

1 Introduction:

The original reason for development of CAE is to eliminate physical prototypes and tests, but many engineers and companies don't trust on result they get using CAE, so physical prototypes are still milestones in almost every design organization. For organizations simulation technology is not a problem, most companies demonstrated that when best practices are followed, results are consistent and correlated with the physical world. Inconstancy in the application of CAE technology leads to variability in results.
Process automation is the key to improving consistency. Like manufacturing, in CAE also automation was the key to improving product quality.
Altair Process Manager is programmable task management software that guides to define standard work process. It allows automating any step in simulation process. Process template provides a starting point and guide for steps to be followed during analysis. It adopts the best practice.
An automated tool is developed using Altair HWPM, commercially available software in compliance with ECE regulations as mentioned above. This Process Automation tool allows CAE analyst to import meshed component with assigned material and element properties with correct card images, selecting UPD type, vehicle data, defining boundary condition/loading position/contacts, control cards, export deck and post processing.
The following tests are carried out to avoid underrun due collision of passenger car and goods carrying vehicle. Also it helps to study the behavior of UPDs for different loading conditions for safety of occupants. Series of iterative simulations are carried out to understand the procedure and to adopt best practice to analyze UPD as per regulation.

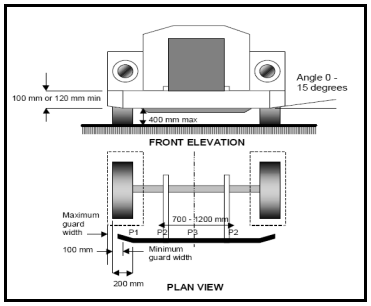

Fig. shows FUPD position

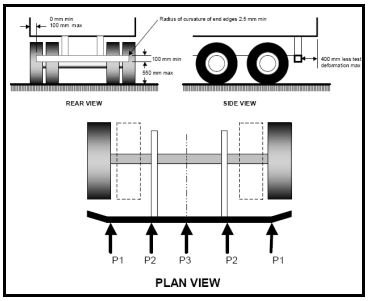

Fig. shows RUPD position

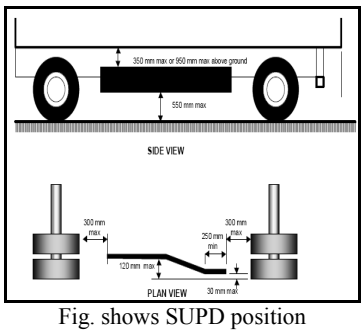

Fig. shows SUPD position

2. Process Methodology

The developed process template using Altair HWPM performs pre and post processing of UPD simulation as per above stated ECE regulations. As most of the tasks are automated through scripting, so complexity of analysis can be reduced. But still user interaction is necessary.

The process manager task tree for UPD simulation looks like as shown in figure.

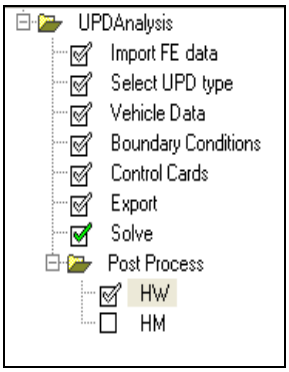

Importing FE Model

This task enable user to import UPD model. The task provided with file browsing dialog boxes for above purpose. The file browser allows importing HyperMesh and RADIOSS model.

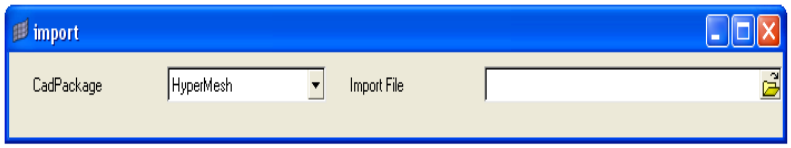

UPD type Selection

This task enables analyst to specify UPD (front, rear or side) type for analysis. According to selection, an appropriate regulation is used for validation and analysis.

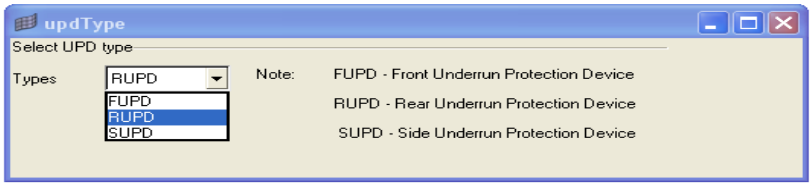

Vehicle data

This task has four sub-tasks those are, entry for vehicle width and axle width/component selection/vehicle type/entry for weight carrying capacity of vehicle. Following figure shows UI of vehicle data in case of selected UPD type is FUPD and RUPD

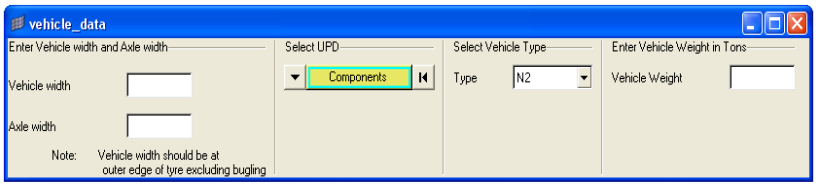

If selected UPD type is SUPD then following UI will be appear instead in above shown

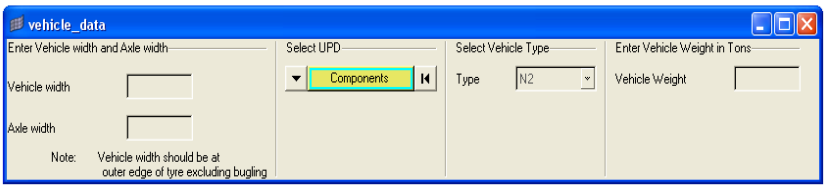

Boundary Condition

With this task analyst can enable to define boundary condition, loading position and contacts. The time entry also provided to input load curve.

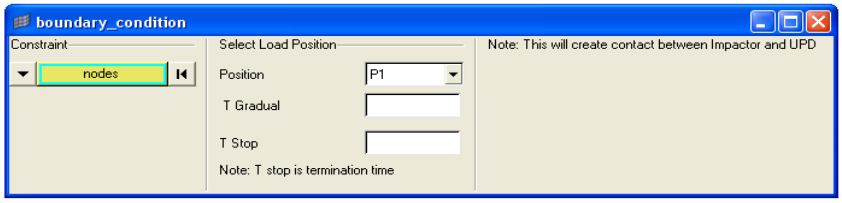

Control Cards
All necessary control cards are created automatically. Entry boxes are provided to get time input for history file and animation file.

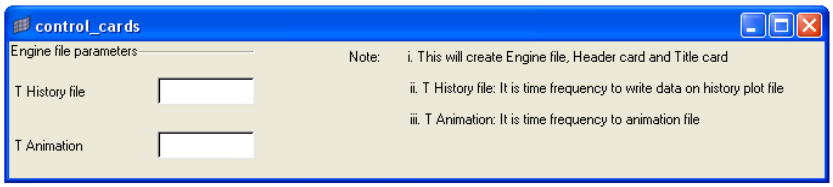

Export
This task allows user to export engine file and starter file as RADIOSS deck. The file name and path, where deck has to be saved can be specified using file browser.

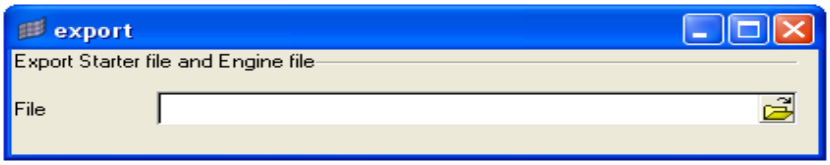

Post Processing
The solved results are automatically exported to HyperView for Post Processing and results will be generated in Word format.

3. Computational Analysis

The deformed shape of FUPD with different loading condition as mentioned in regulation is as shown below

P1 Position

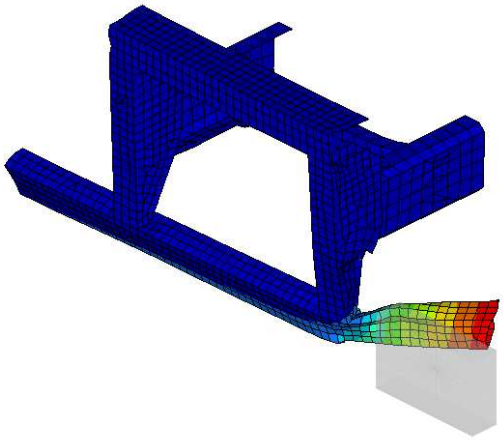

Fig. Displacement of FUPD at P1 Position

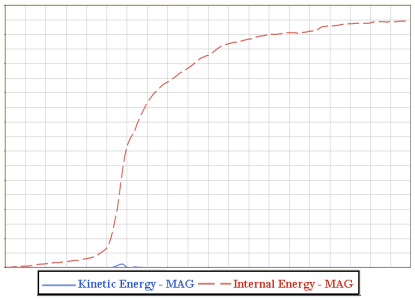

Fig. Energy Vs Time

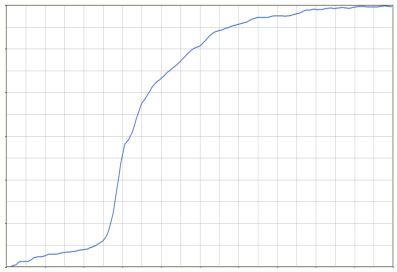

Fig. Displacement Vs Time

P2 Position

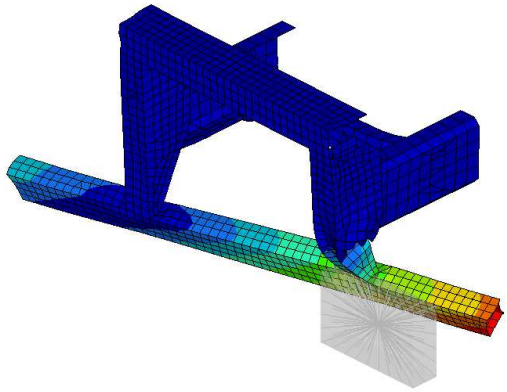

Fig. Displacement of FUPD at P2 Position

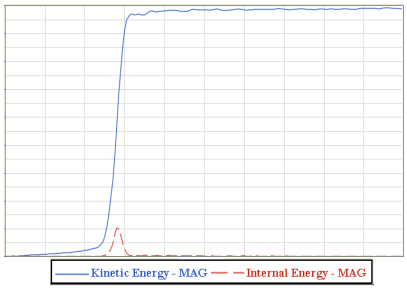

Fig. Energy Vs Time

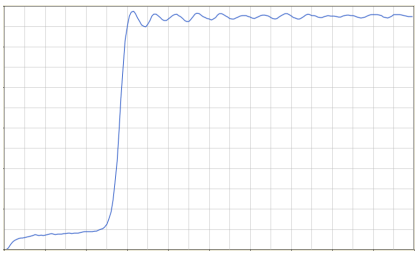

Fig. Displacement Vs Time

P3 Position

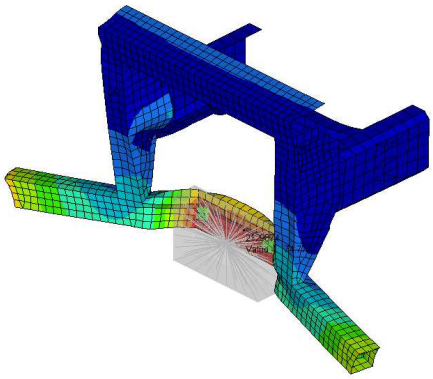

Fig. Displacement of FUPD at P**3** Position

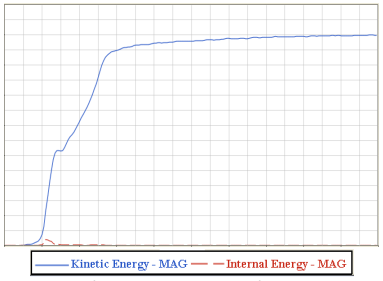

Fig. Energy Vs Time

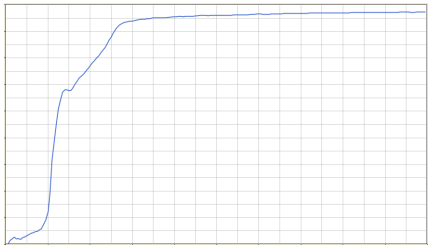

Fig. Displacement Vs Time

4. Result

This process template helps designer to setup CAE model automatically as per ECE regulation. It enables best practices through standardizing UPD simulation process. It also helps to minimize model setup time during research and model certification process.

5. Conclusion

With the above results, it is concluded that the process template developed using Altair HyperWorks products for analysis of UPD is correct. This template saves a lot of time to setup deck for analysis of UPD as per ECE regulations to meet stringent regulation and time constrain

6. Benefits Summary

- Standardize process flow
- Maintain consistent output result
- Saves deck setup time for simulation, ultimately reduces cost
- Maximized resource usages

7. References

i. The Automotive Research Association of India, Pune, Front Underrun Protective Devices (FUPD); (ECE R 93) Date of entry into force: 27 Feb 1994
ii. The Automotive Research Association of India, Pune, Rear Underrun Protective Devices (RUPD): (ECE R 58) Date of entry into force: 11 July 2008
iii. The Automotive Research Association of India, Pune, Side Underrun Protective Devices (SUPD);(ECE R 73) Date of entry into force: 09 Dec 2010
iv. Altair HyperWorks 11.0 suite manuals


Proceedings, 5th Chaotic Modeling and Simulation International Conference, 12 – 15 June 2012, Athens Greece

Delay Factors and Chaotization of Non-ideal Pendulum Systems

Aleksandr Yu. Shvets and Alexander Makaseyev

National Technical University of Ukraine Kyiv Polytechnic Institute, Kyiv, Ukraine
(E-mail: alex.shvets@bigmir.net, makaseyev@ukr.net)

Abstract. The oscillations of a plane pendulum, the suspension point of which excites by electric motor of the limited power with taking into account various factors delay are considered. Regular and chaotic attractors, phase-parametric characteristics and maps of dynamic regimes of this system are built and explored. Influence of delay factors on the appearance of deterministic chaos is analysed in detail.
Keywords: delay, chaotic attractor, map of dynamic regimes.

1 Introduction

Pendulum mathematical models are widely used to describe the dynamics of various oscillatory systems. Such models are used to study the oscillation of free liquid surface, membranes, various technical constructions, in the study of cardiovascular system of live organisms, financial markets, etc.

The problems of global energy saving require the highest minimization of excitation source power of oscillatory systems. This leads to the fact that the energy of excitation source is comparable to the energy consumed by the oscillating system. Such systems as "source of excitation - oscillating subsystem" are called nonideal by Zommerfeld-Kononenko [1]. In mathematical modeling of such systems, the limitation of excitation source power must be always taken into account.

Another important factor, that significantly have an influence on steady-state regimes of dynamical systems are different, by their physical nature, factors of delay. The delay factors are always present in rather extended systems due to the limitations of signal transmission speed: waves of compression, stretching, bending, current strength, etc. The study of the influence of delay factors on the dynamical stability of equilibrium positions of pendulum systems was initiated by Yu. A. Mitropolsky and his scientific school in the 80s of the last century [2], [3]. But only ideal pendulum models were initially considered. Mathematical models of pendulum system with limited excitation, taking into account the influence of different factors of delay, were first obtained in [4], [5]. The influence of delay factors on existence and dynamic stabilization of pendulum equilibrium positions at limited excitation was studied. Later it was discovered the existence of chaotic attractors in nonideal systems "pendulum - electric motor" and proved that the main cause of chaos is limited excitation [4], [5], [7].

In this paper the oscillations of a flat pendulum, the suspension point of which excites by electric motor of the limited power with taking into account various factors delay are considered.

2 Mathematical model of the system

In [6] the equations of motion of the system "pendulum - electric motor" in the absence of any delay factors were obtained. They are

$$\begin{cases} \dfrac{dy_1}{d\tau} = Cy_1 - y_2y_3 - \dfrac{1}{8}(y_1^2y_2 + y_2^3); \\ \dfrac{dy_2}{d\tau} = Cy_2 + y_1y_3 + \dfrac{1}{8}(y_1^3 + y_1y_2^2) + 1; \\ \dfrac{dy_3}{d\tau} = Dy_2 + Ey_3 + F; \end{cases} \tag{1}$$

where phase variables y_1y_2 describe the pendulum deviation from the vertical and phase variable y_3 is proportional to the rotation speed of the motor shaft. The system parameters are defined by

$$C = -\delta\varepsilon^{-2/3}\omega_0^{-1}, D = -\frac{2ml^2}{I}, F = 2\varepsilon^{-2/3}(\frac{N_0}{\omega_0} + E) \tag{2}$$

where m - the pendulum mass, l - the reduced pendulum length, ω_0 - natural frequency of the pendulum, a - the length of the electric motor crank, $\varepsilon = \frac{a}{l}$, δ - damping coefficient of the medium resistance force, I - the electric motor moment of inertia, E, N_0 - constants of the electric motor static characteristics.

Let us consider the following system of equations:

$$\begin{cases} \dfrac{dy_1(\tau)}{d\tau} = Cy_1(\tau-\delta) - y_2(\tau)y_3(\tau-\gamma) - \dfrac{1}{8}(y_1^2(\tau)y_2(\tau) + y_2^3(\tau)); \\ \dfrac{dy_2(\tau)}{d\tau} = Cy_2(\tau-\delta) + y_1(\tau)y_3(\tau-\gamma) + \dfrac{1}{8}(y_1^3(\tau) + y_1(\tau)y_2^2(\tau)) + 1; \\ \dfrac{dy_3(\tau)}{d\tau} = Dy_2(\tau-\gamma) + Ey_3(\tau) + F; \end{cases} \tag{3}$$

This system is a system of equations with constant delay. Positive constant parameter γ was introduced to account the delay effects of electric motor impulse on the pendulum. We assume that the delay of the electric motor response to the impact of the pendulum inertia force is also equal to γ. Taking into account the delay γ conditioned by the fact that the wave velocity perturbations on the elements of the construction has a finite value that depends on the properties of external fields, for instance, the temperature field. In turn, the constant positive parameter δ characterizes the delay of the medium reaction on the dynamical state of the pendulum. This delay is due to the limited sound velocity in that medium.

Assuming a small delay, we can write

$$y_1(\tau-\delta) = y_1(\tau) - \frac{y_1(\tau)}{d\tau}\delta + ..., \quad y_2(\tau-\delta) = y_2(\tau) - \frac{y_2(\tau)}{d\tau}\delta + ...$$

$$y_2(\tau-\gamma) = y_2(\tau) - \frac{y_2(\tau)}{d\tau}\gamma + ..., \quad y_3(\tau-\gamma) = y_3(\tau) - \frac{y_3(\tau)}{d\tau}\gamma + ...$$

Then, if $C\delta \neq -1$, we get the following system of equations:

$$\begin{cases} \dot{y_1} = \dfrac{1}{1+C\delta}\left(Cy_1 - y_2\left[y_3 - \gamma\left(Dy_2 + Ey_3 + F\right)\right] - \dfrac{1}{8}(y_1^2 y_2 + y_2^3)\right); \\ \dot{y_2} = \dfrac{1}{1+C\delta}\left(Cy_2 + y_1 y_3 - y_1\gamma(Dy_2 + Ey_3 + F) + \dfrac{1}{8}(y_1^3 + y_1 y_2^2) + 1\right); \\ \dot{y_3} = (1 - C\gamma)Dy_2 - \dfrac{D\gamma}{8}(y_1^3 + y_1 y_2^2 + 8y_1 y_3 + 8) + Ey_3 + F. \end{cases} \tag{4}$$

The obtained system of equations is already a system of ordinary differential equations. Delays are included in this system as additional parameters.

The study of the influence of delay factors on existence and stability of equilibrium positions of the system (4) was carried out. Also the effect of delay on origin the deterministic chaos was studied. Since the system of equations (4) is strongly nonlinear, the study of steady-state regimes has been carrying out using numerical methods. A large set of computer experiments have been held to determine the possibility of chaotic attractors' occurrence in the system (4). The methodology of these computer experiments is described in detail in [6].

3 Dynamic regimes maps

A very clear picture of the dynamical system behavior can give us a map of dynamic regimes. It is a diagram on the plane, where two parameters are plotted on axes and the boundaries of different dynamical regimes areas are shown. The construction of dynamical regimes maps is based on the analysis and processing of spectrum of Lyapunov characteristic exponents, phase portraits, Poincare sections and maps, Fourier spectrums and distributions of the invariant measure of attractors of the system. The atlas of maps of dynamic regimes of nonideal system "pendulum–electric" motor in the absence of delay factors were obtained in [8].

Fig. 1a shows a map of dynamical regimes, when the parameters E and D are changing, and the parameters C, D are equal to $C = -0.1, F = 0.19$ in the case of delay absence in the system. The dark-grey areas of the maps correspond to equilibrium positions of the system. The light-grey areas of the maps correspond to limit cycles of the system. And finally, the black areas of the maps correspond to chaotic attractors.

Fig. 1b–d illustrate the influence of delays γ and δ on changing the type of steady-state regime of the system. Thus Fig.1b was built at the values of the parameters $D = -0.8, E = -0.6$ that correspond to the dark-grey area of the map 1a. As can be seen from Fig.1b the type of steady-state regime does not change at very small values of the delay. It is still an equilibrium position. However, with an increase of delay values γ and δ the limit cycles appear in the system (light-grey areas of the map) and then the chaotic attractors (black areas of the map). And there is a quite complex and fanciful structure of alternating regions of existence of periodic and chaotic regimes.

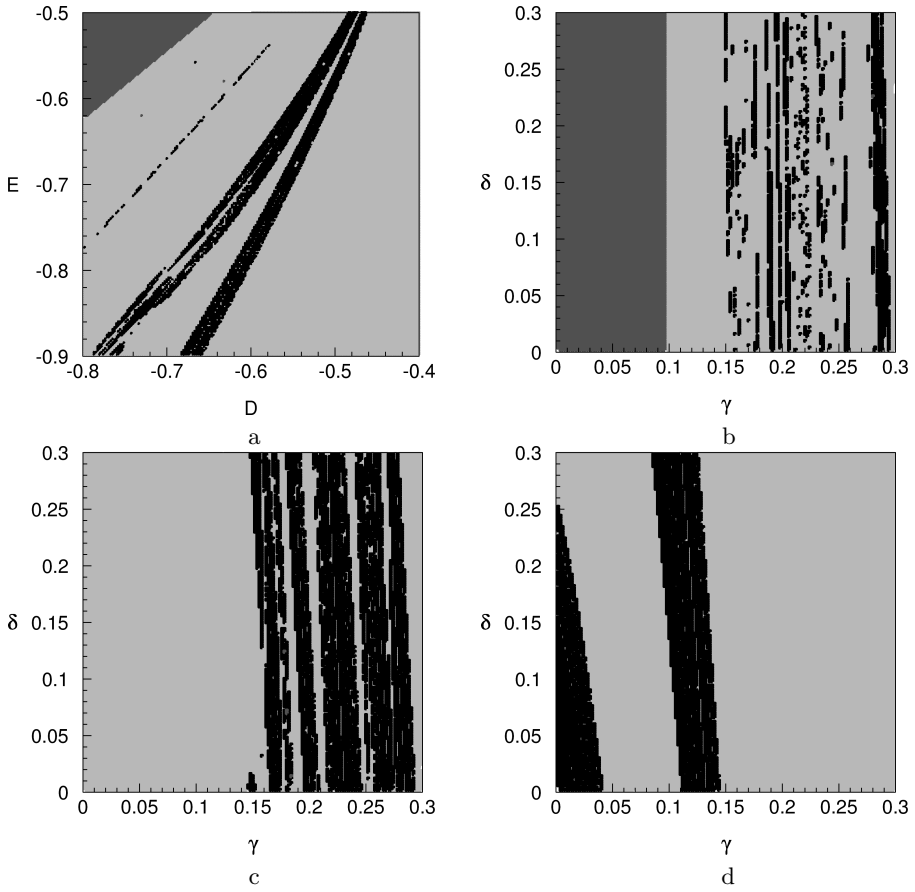

Fig. 1. Maps of dynamic regimes

Fig.1c was built at the values of the parameters $D = -0.58, E = -0.6$ that correspond to the light-grey area of the map 1a (periodic regimes). As can be seen from this figure the attractor of the system is limit cycle at very small values of the delays. With an increase of the delay values the chaos arises in the system (black areas in the figure). Finally, fig.1d was built at the values of the parameters $D = -0.53, E = -0.6$ that correspond to the black area of the map 1a (chaotic regimes). In this case, with an increase of the delay values the region of chaos is replaced by the region of periodic regimes. Then again chaos arises in the system.

Apparently from figures 1b–d when the delay of interaction between a pendulum and the electromotor γ greater than certain value, change of types of steady-state regimes can be observed at very small value of delay of a medium δ.

In fig.2a the map of dynamical regimes at $C = -0.1, D = -0.6$ in the case of delay absence is constructed. In fig.2b the change of steady-state regimes types, which takes place in the system with an increase of the delay values

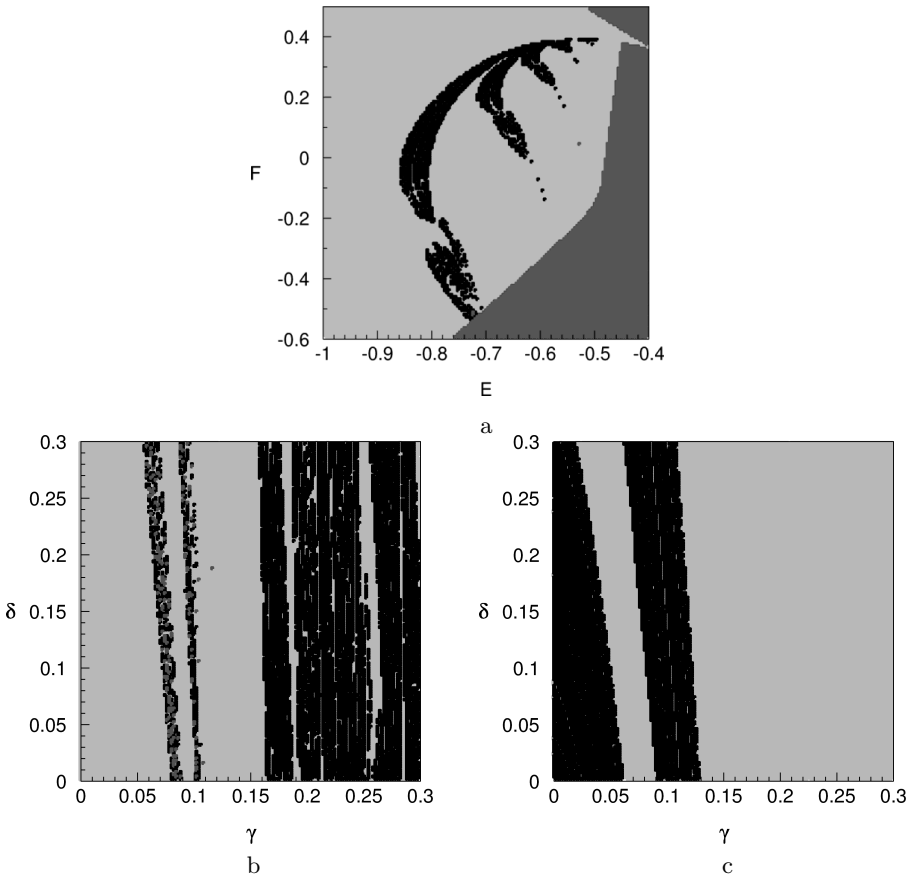

Fig. 2. Maps of dynamic regimes

is shown. Thus the point (0, 0) of the map corresponds to the values of the parameters $E = -0.7, F = -0.4$ at which the steady-state regime is a limit cycle. With an increase of the delay values in the map there are narrow areas in which the limit cycle is replaced by an equilibrium position, as well as by a chaotic attractor. Further there is a rather wide area of periodic regimes, which with further increase of the delay is replaced by chaos area. But, in this rather wide area of chaos narrow strips of periodic regimes "are built in". A Fig.2c was built for parameters $E = -0.67, F = 0.3$ that corresponds to the black area of the map 2a (chaotic regimes). Here, with an increase of values of delay the changes of the steady-state regime such as "chaos–cycle–chaos–cycle" are observed. And, apparently from this figure, we see that change of type of a steady-state regime can be observed and at very small values of the delays. increase of the delay happens under the scenario of Pomeau-Manneville, in a single bifurcation, through intermittency.

Similar changes of the dynamical regimes types of the system (4), which are observed with the delay change, are shown in Fig.3. The initial map of

dynamical regimes was built at $C = -0.1$, $E = -0.59$ (fig.3a). The maps in fig. 3b, c are constructed at $D = -0.53$, $F = -0.4$ and $D = -0.5$, $F = -0.31$ respectively. As can be seen from fig. 3b, c with an increase of the delay values the change of the steady-state regime may take place such as "equilibrium position–cycle–chaos" or "cycle–chaos" in different variations of the order of these changes.

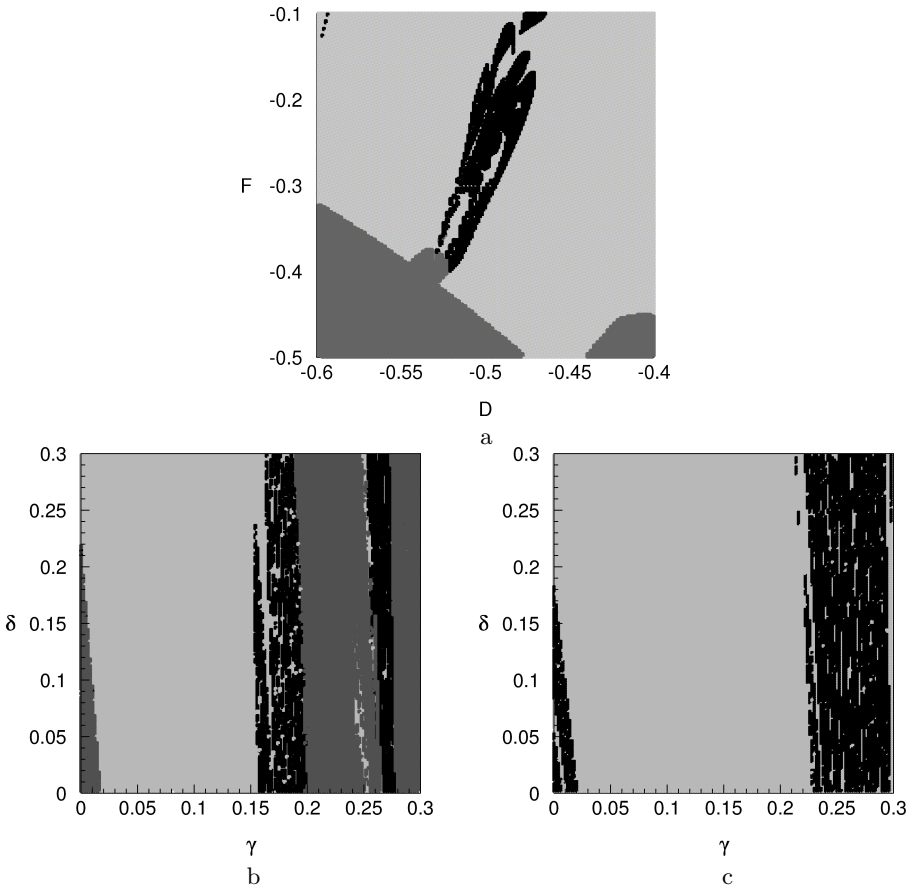

Fig. 3. Maps of dynamic regimes

4 The study of steady-state regimes of interaction

Let us consider in detail the types of regular and chaotic attractors that exist in the system (4). Let us consider the behavior of the system (4) when parameters are $C = -0.1$, $D = -0.8$, $E = -0.6$, $F = 0.19$ and the delays $\gamma = 0.29$ and $0 \leq \delta \leq 0.29$. In fig. 4a,b the dependence of maximum non-zero Lyapunov's characteristic exponent and phase-parametric characteristic of the system are shown respectively. These figures illustrate the influence of the delay of the

medium δ, in which the oscillations of the pendulum are, on chaotization of the system (4).

So in Fig.4a we can clearly see the presence of intervals δ in which maximum Lyapunov exponent of the system is positive. In these intervals in the system there are chaotic attractors. The area of existence of chaos is clearly seen in phase-parametric characteristic of the system. The areas of chaos in the bifurcation tree are densely filled with points. A careful examination of the obtained images allows not only to identify the origin of chaos in the system, but also to describe the scenario of transition to chaos. So with a decrease of δ there are the transitions to chaos by Feigenbaum scenario (infinite cascade of period-doubling bifurcations of a limit cycle). Bifurcation points for delay δ are clearly visible in Fig.4a as well as in Fig.4b. These points are the points of approaches of the Lyapunov's exponent graph to the zero line (Fig.4a) and the points of splitting the branches of the bifurcation tree (Fig.4b). In turn, the transition to chaos with an increase of the delay happens under the scenario of Pomeau-Manneville, in a single bifurcation, through intermittency.

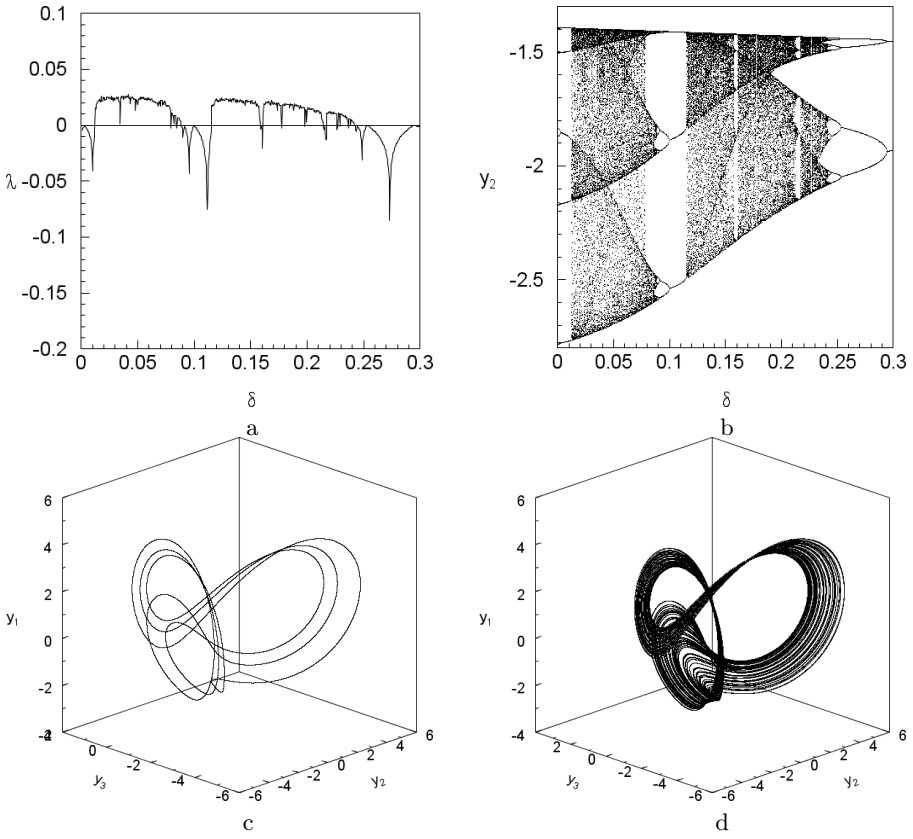

Fig. 4. The dependence of maximal non-zero Lyapunov's characteristic exponent (a), phase-parametric characteristic of the system (b), phase portrait of the limit cycle (c) and the chaotic attractor (d)

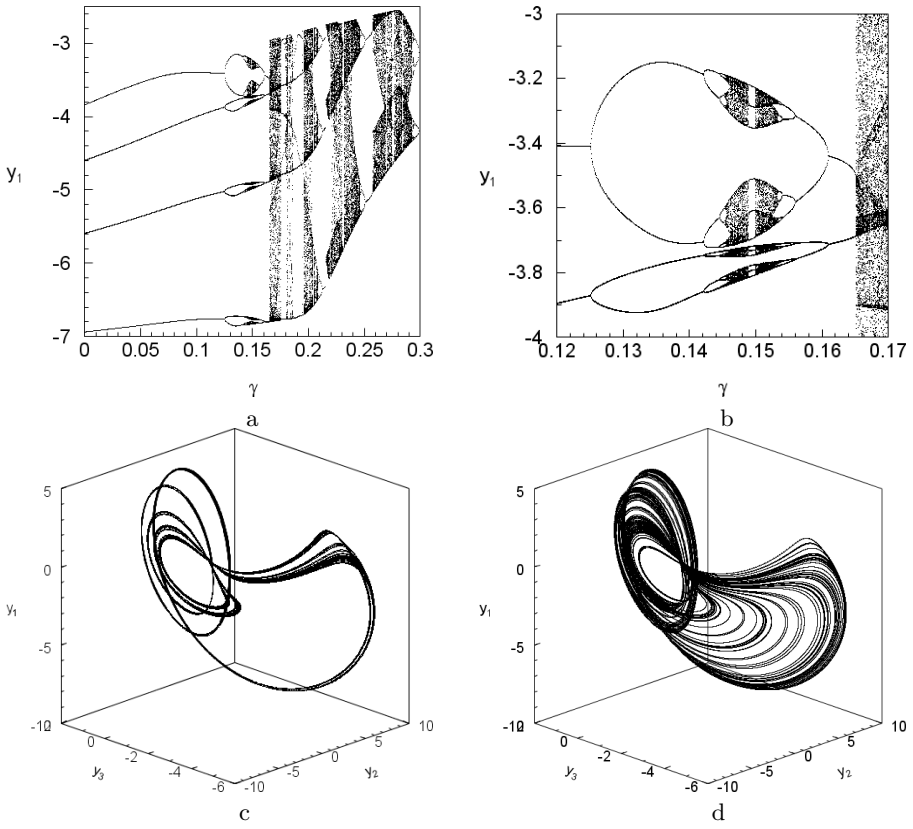

Fig. 5. Phase-parametric characteristics of the system (a)–(b), phase portraits of the chaotic attractors (c)–(d)

In Fig.4c,d phase portrait of one of the limit cycles, at $\delta = 0.11$, of the cascade of period-doubling bifurcations and phase portrait of the chaotic attractor at $\delta = 0.07$ that arises at the end of this stage are shown respectively.

Let us study the influence of the delay γ when parameters are $C = -0.1$, $D = -0.58$, $E = -0.6$, $F = 0.19$ and in the absence of the delay of the medium δ. In Fig.5a the phase-parametric characteristic of the system and in Fig.5b an enlarged fragment of the central part of this characteristic are constructed. Let us consider in more detail Fig.5b. Here there is situation, atypical for dynamical systems, of transition to chaos. As it is known, the most typical situation is when the transition to chaos happens with a decrease (increase) the bifurcation parameter through a cascade of period-doubling bifurcations and with an increase (decrease) the bifurcation parameter - through intermittency. Here there is some symmetry of scenarios of transition to chaos. As can be seen from Fig.5b, there is an interval of change the values γ in which the transition to chaos under the Feigenbaum scenario can be observed both with a decrease and with an increase of values γ. An analogous situation occurs in this interval of changes γ for intermittency. In other words the transition to chaos through

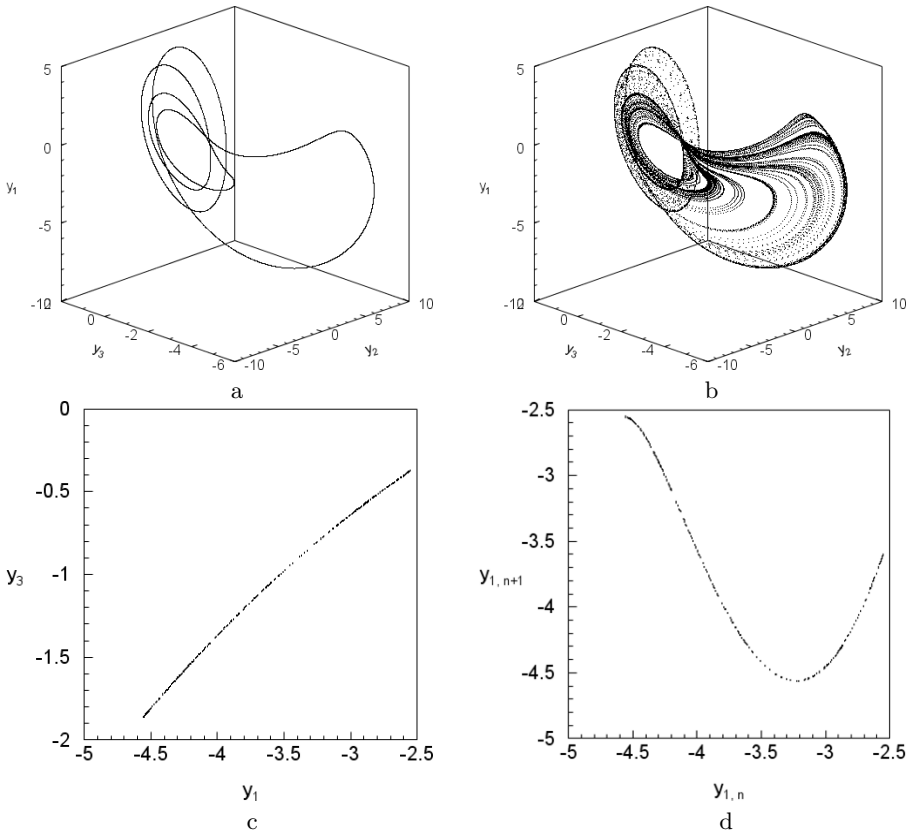

Fig. 6. The distribution of the invariant measure of the limit cycle (a) and the chaotic attractor (b), the Poincare section (c) and map (d) of the chaotic attractor

intermittency can be observed both with a decrease and with an increase the values γ. On the right part of the bifurcation tree the typical situation for non-linear dynamics is observed.

In Fig.5c,d the typical in this case phase portraits of chaotic attractors of the system are shown. The chaos shown in Fig.5c is characterized by a relatively small volume of localization in phase space of the system (4). Conversely, in Fig.5d the "developed" chaos with a much larger volume of localization in phase space is shown.

Let the system (4) parameters be $C = -0.1$, $D = -0.58$, $E = -0.6$, $F = 0.19$ and the delay $\delta = 0$. The distributions of the invariant measure of the limit cycle at $\gamma = 0.165$ (fig.6a) and the chaotic attractor at $\gamma = 0.1652$ (fig.6b) illustrate the transition to chaos through intermittency when changing the delay γ. These distributions of the invariant measure on the phase portrait of attractors allow us to identify the laminar and turbulent phase of chaotic attractor that arises under the scenario of Pomeau-Manneville.

In fig. 6c,d, rather typical for this system, the Poincare section and the Poincare map of the chaotic attractor at $\gamma = 0.28$ are constructed. Both of them

have "quasiribbon" structure. This allows building an analytical approximation of Poincare map that can be used for an approximate study the dynamics of the three-dimensional system using one-dimensional discrete map [9].

5 Conclusions

Thus, various factors of delay make the considerable influence on dynamics of system "pendulum - electromotor". Delay presence in such systems can cause both origin, and vanishing of chaotic attractors. Besides, delay leads to occurrence of atypical situations at transitions from the regular regimes to deterministic chaos.

References

1.V. O. Kononenko, *Vibrating System with a Limited Power-supply*, Iliffe, London, 1969.

2.Yu. A. Mitropolsky, A.Yu. Shvets. About influence of delay on a stability of a pendulum with the vibrating suspension point. *Analytical methods of non-linear oscillations*, Kyiv, 115–120, 1975 (in russian).

3.Yu. A. Mitropolsky, A.Yu. Shvets. About oscillations of a pendulum with a vibrating point of a suspension at presence delays. *Analytical methods of non-linear oscillations*, Kyiv, 120–128, 1975 (in russian).

4.T. S. Krasnopolskaya, A. Yu. Shvets. Chaotic interactions in a pendulum-energy-source system. *Prikl. Mekh.*, 26, No. 5, 90–96, 1990.

5.T. S. Krasnopolskaya, A. Yu. Shvets. Chaos in vibrating systems with limited power-supply. *Chaos*, 3, 3:387–395, 1993.

6.T. S. Krasnopolskaya, A. Yu. Shvets. *Regular and chaotical dynamics of systems with limited excitation.* R&C Dynamics, Moscow, 2008, (in russian).

7.A. Yu. Shvets, A. M. Makaseyev. Chaotic Oscillations of Nonideal Plane Pendulum Systems. *Chaotic Modeling and Simulation (CMSIM)*, 195–204, January 2012 Issue.

8.A. Yu. Shvets, A. M. Makaseyev. The atlas of maps of dynamic regimes of nonideal system "pendulum - electric motor". *Proceedings of the Institute of Mathematics of NAS of Ukraine*, vol. 7, no. 3, 465–480, 2010 (in russian).

9.V. S. Anishchenko, V. V Astakhov, A. B Nieman, T. E. Vadivasova, and L. Schimansky Geier *Nonlinear Dynamics of Chaotic and Stochastic Systems*. Springer, Berlin, 2003.


Proceedings, 5th Chaotic Modeling and Simulation International Conference, 12 – 15 June 2012, Athens Greece

Evidence of chaos in the Belief Propagation for LDPC codes

J.C. Sibel, S. Reynal, and D. Declercq

ETIS / ENSEA / Univ. Cergy-Pontoise / CNRS UMR 8051
F-95000, Cergy-Pontoise, France
(E-mail: {jean-christophe.sibel,reynal,declercq}@ensea.fr)

Abstract. In this paper, we investigate the behaviors of the Belief Propagation algorithm considered as a dynamic system. In the context of LDPC (Low Density Parity-Check) codes, we use the noise power of the transmission channel as a potentiometer to evaluate the different motions that the BP can follow. The computations of dynamic quantifiers as the bifurcation diagram, the Lyapunov exponent and the reconstructed trajectory enable to bring out four main behaviors. In addition, we propose a novel measure that is the hyperspheres method, which provides the knowledge of the time evolution of the attractor size. The information collected from these different quantifiers helps to better understand the BP evolution and to focus on the noise power values for which the BP suffers from chaos.
Keywords: LDPC, iterative map, chaos, Lyapunov exponent, bifurcation diagram.

1 Introduction

The channel coding is a research field whose purpose is to protect an information to transmit from environmental disturbances. The first step is the encoding of the information, a procedure in which the information, modeled as a sequence of k bits $u_1, \ldots, u_k$, is mapped to a larger sequence of N bits $x_1, \ldots, x_N$. The map consists in artificial correlations called constraints or parity-check equations. In [1] are introduced the Low-Density Parity-Check (LDPC) codes which are a widespread technique to encode the information. Such a code can be represented by a Tanner graph [2], a graphical representation which turns out to be very useful in the second step, the decoding. In this part, the bits transmitted though a random noisy channel are iteratively handled by a decoding algorithm to create an associated output sequence of N bits that verify the whole set of parity-check equations and that must be as close as possible to the input sequence. One of the most famous decoding algorithm is the Belief Propagation (BP) [3], also used in statistical physics [4], extensively studied in [5,6], which is deemed to be the optimal message-passing algorithm in the case the Tanner graph of the LDPC code is loopfree. However, in most cases the Tanner graph is not loopfree [7] that involves that the BP becomes suboptimal. Moreover, the BP presents some complex behaviors in terms of the noise power of the transmitted channel, as periodic and chaotic motions [8]. Along the whole paper, we present some

measures to bring out these different behaviors. The paper is organized as follows: in the second section are presented preliminaries about the LDPC codes and the BP, in the third section we present the dynamic environment of the BP, the measures to identify the behaviors and the associated results.

2 LDPC codes and Belief Propagation

We consider a set of N binary random variables $\mathbf{X} = \{X_1, \ldots, X_N\}$ whose global state is denoted by $\mathbf{x} = [x_1, \ldots, x_N]$. An LDPC code is built by a set of M constraints, or parity-check equations, $\mathbf{C} = \{C_1, \ldots, C_M\}$ such that for each check C_j its state is $c_j = \sum_{X_i \in \mathcal{N}_j} x_i$ where $\mathcal{N}_j$ is a subset of $\mathbf{X}$ called the neighborhood of C_j depending on the LDPC code, and the sum is computed over the Galois field GF(2). We consider that C_j and X_i such that $X_i \in \mathcal{N}_j$, form an edge e_{ij} between two nodes inside an undirected bipartite graph called the Tanner graph $\mathbf{G} = (\mathbf{X} \cup \mathbf{C}, \{e_{ij}\})$. An example of a Tanner graph is displayed on the figure 1.

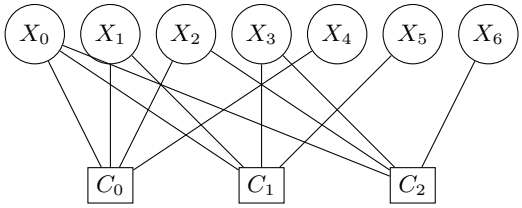

Fig. 1. Tanner graph of the Hamming code

The purpose of the BP is to estimate the joint probability distribution $p(\mathbf{X} = \mathbf{x})$, written simply $p(\mathbf{x})$, by a distribution called the belief $b(\mathbf{x})$ and to extract the most likely state $\hat{\mathbf{x}} = \arg\max_{\mathbf{x}} b(\mathbf{x})$ considered as the estimate of the input sequence. Each variable X_i has its own marginal probability distribution $p_i(x_i)$ and its own belief $\{b_i(x_i)\}_{1 \leq i \leq N}$. The BP is an iterative algorithm that consists in passing messages between the variables and the constraints on the edges of a given Tanner graph at each iteration k. For each edge e_{ij}:

- the messages $n_{ji}^{(k)}(x_i)$ from C_j to X_i are: $n_{ji}^{(k)}(x_i) = f_{ji}(\{m_{xy}^{(k-1)}\}_{(x,y)})$
- the messages $m_{ij}^{(k)}(x_i)$ from C_i to C_j are: $m_{ij}^{(k)}(x_i) = g_{ij}(\{n_{yx}^{(k)}\}_{(x,y)}, l_i(x_i))$

where the functions f_{ij} and g_{ji} are detailed in [2], and $\{l_i(x_i)\}_i$ are the likelihoods $\mathbf{L}(\mathbf{x}) = \{l_1(x_1) = p(y_1|x_1), \ldots, l_N(x_N) = p(y_N|x_N)\}$ computed from the channel obervations $\{y_1, \ldots, y_N\}$. The noisy transmission channel that we use in all of our simulations is an additive white Gaussian noise channel whose power is σ^2. We summarize the message-passing by a unic implicit equation $\forall e_{ij}, \quad n_{ji}^{(k)} = G_{ij}(\{n_{nm}^{(k-1)}\}_{(m,n)}, \{l_i\}_i)$. The convergence

of the BP is: $\forall e_{ij},\ n_{ji}^{(k)} = n_{ji}^{(k-1)}$. These messages provide the computation of the beliefs, whose equations are defined in [2]. All the simulations that follow are done on a commonly used example which is the Tanner code [9].

3 Dynamics

3.1 State space definition and properties

We consider $\{G_{ij}\}_{(i,j)}$ as a set of iterated maps on the state variables $\{n_{ji}^{(k)}\}_{(i,j)}$ and $T^{(k)} = \{n_{ji}^{(k)}\}_{(i,j)}$ as the points of the trajectories of the BP at iteration k in the associated state space $\mathcal{E}$.

3.2 Parameters and scaling

In [8] the value of σ^2, or the corresponding Signal to Noise Ratio (SNR), is used as a parameter such that different values imply different motions of the BP. However, most of their simulations are done for particular noise realizations and scaled on the SNR, that prevents from evaluating a statistical behavior. A reason is that the noise realizations that lead the BP not to converge or to converge to a wrong estimate are rare events, essentially because the LDPC codes and the iterative algorithms are created to this end. A way to have some statistical evaluations of the behavior of the BP is:

1. finding some of these noise realizations,
2. storing the corresponding initializations on the state variables,
3. averaging the quantities to measure for a sufficient set of initializations that are close in the state space in the sense of the Euclidean distance.

By this way, we target the critical values, i.e. the SNR that correspond to a blatant change in the behavior of the algorithm, which are the bifurcations.

3.3 Bifurcation diagram

A relevant method to extract the critical values of the SNR is the use of the bifurcation diagram. It consists in evaluating the value of a function E that is computed from the state variables at their steady state for J different values of the SNR. We get a sequence $[E_{\sigma_1}, \ldots, E_{\sigma_J}]$ that represents the behavior of the dynamic system in terms of the SNR. We consider the following function exposed in [8] called the mean square beliefs:

$$\forall \sigma, \quad E_\sigma = \sqrt{\frac{1}{N} \sum_{i=0}^{N-1} b_i^2(0)} \tag{1}$$

where the input sequence in the channel is the null sequence and the beliefs are computed at the last iteration K of the BP algorithm. Obviously, there is

no reason that the associated dynamic system has reached any steady state at this iteration but we need to suppose it for computation time's sake. This function presents three important values:

- $E_\sigma = 1$: all the beliefs indicate that the ouput sequence is the null sequence which is a good decoding,
- $E_\sigma = \frac{1}{4}$: all the beliefs are uniform thus there is no information about the state of the transmitted bits, which is a missed decoding,
- $E_\sigma = 0$: all the beliefs indicate that the output sequence is the complementary of the sent sequence, which is a completely wrong decoding.

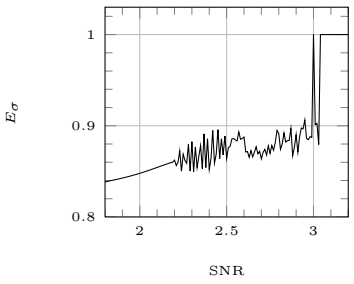

Fig. 2. Bifurcation diagrams of the BP

The display of $[E_{\sigma_1}, \ldots, E_{\sigma_J}]$ enables to know two properties of the used algorithm: the amplitudes provides information about the decoding performance, and the variation between successive values gives us the critical values of the SNR. We display on the figure 2 the mean bifurcation diagrams of the BP. We observe that for SNRs lower than 2.19 dB, the BP follows a regular increasing steady motion. When the SNR is greater than this critical value, the algorithm follows a periodic motion. However, for values in [2.5 dB, 2.98 dB] it does not appear any known evolution which can be an indication of chaos. For values greater than 2.99 dB, the BP converges to the good decoding state.

3.4 Reduced trajectory

Another use of the mean square beliefs function is the representation of the trajectory in a 3-dimensional state space. To this end, we use the phase space reconstruction [10]. The method is first to compute this function at each iteration to get the following sequence $\mathbf{E}_\sigma = [E_\sigma(k)]_{0 \leq k \leq K}$. Afterthat we share this one dimensional sequence in a three dimensional sequence $\tilde{\mathbf{E}}_\sigma$. On the figures 3 and 5 are displayed some reduced trajectories of the BP for typical values of the SNR deduced from the previous bifurcation diagram.
It appears four typical behaviors that match with the four intervals exposed in the previous paragraph. We obtain a very small sized attractor for SNR = 2.10 dB that can be considered as a fixed point, whereas the reduced trajectory transforms to a limit cycle when the SNR is between 2.19 dB and 2.49 dB. A crucial point is that the thickness of the trajectory along this limit cycle increases as the SNR is getting greater up to 2.50 dB.

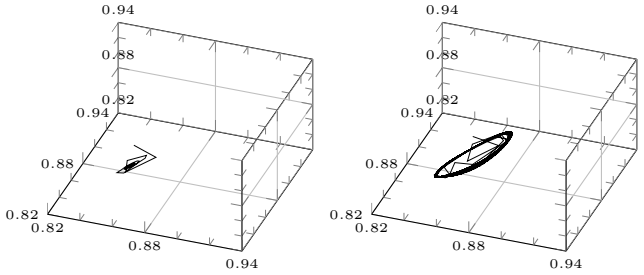

Fig. 3. Reduced trajectory for the BP on the Tanner code with SNR = 2.15 dB and 2.30 dB

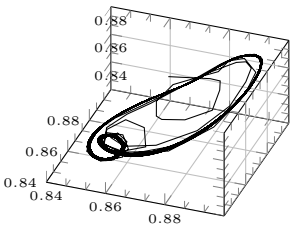

Fig. 4. Reduced trajectory for the BP on the Tanner code with SNR = 2.40 dB

At the same time this limit cycle interleaves with other limit cycles, that can be understood as a sequence of period doubling bifurcations in terms of dynamic system, as is displayed on the figure 4 with two interleft cycles. Such a phenomenon is a typical route to chaos, that is observable from 2.51 dB. A chaotic motion means that there is not any periodic motion or fixed point convergence anymore, as it is displayed for 2.70 dB. When the SNR reaches 2.99 dB the trajectory collapses to a single point that is a true fixed point.

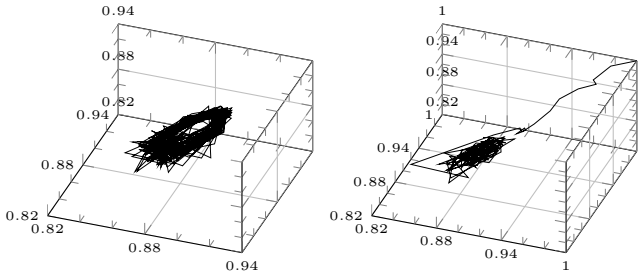

Fig. 5. Reduced trajectory for the BP on the Tanner code with SNR = 2.70 dB and 3.00 dB

We have to be cautious because $\tilde{\mathbf{E}}_\sigma$ is not a true trajectory, it does not respect the Cauchy-Lipschitz condition [10] due to the non bijection between the messages and the beliefs. Thus, this sequence only has the role of giving clues about the true behavior as the possible shape of the actual trajectory in $\mathcal{E}$ that are: convergence to a fixed point, convergence to a limit cycle,

convergence to a chaotic attractor. To distinguish these shapes, we need a criterion that reflects the behavior by its own value.

3.5 Lyapunov exponents

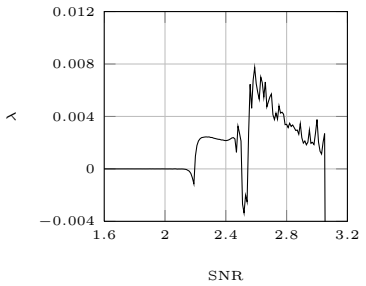

Fig. 6. Lyapunov exponents of the BP on the Tanner code scaled on the SNR

A common measure is the Lyapunov exponent λ, that consists in evaluating at each iteration $k \leq K$ the log-ratio of the Euclidean distance between two initially close trajectories. As detailed in [11,10] the sign of λ reveals the behavior of the system around the corresponding initialization of the trajectories: $\lambda \geq 0$ means the trajectories have moved away one from the other, which is an evidence of a chaotic behavior,$\lambda \leq 0$ means the trajectories have got closer, which is an evidence of a convergent behavior to a small sized volume of the state space. This volume is reduced to a fixed point if and only if $\lambda \to \infty$. When λ crosses the x-axis the system suffers from a bifurcation meaning that the algorithm has changed of motion. The corresponding SNR are the critical values. We display on the figure 6 the Lyapunov exponents of the BP on the Tanner code. As we have observed on the bifurcation diagrams, the evolution is really different as soon as the SNR is greater than 2.09 dB. The BP curves is perfectly consistent with the associated bifurcation diagram in the sense that the critical values we extract are the same and the behaviors we could imagine by the bifurcation diagram are also revealed by the Lyapunov exponent. A relevant analyze we need to effect is the comparison with the reduced trajectory we exposed previously so as to associate accurately with each reduced motion a particular evolution of λ. For SNR $\in [0\text{dB}; 2.19\text{db}]$: the reduced trajectory converges to a very small sized volume of $\mathcal{E}_{BP}$ that we can consider as a fixed point whereas λ is close to the null value, for SNR $\in [2.20\text{db}; 2.49\text{db}]$: the reduced trajectory is trapped into a limit cycle whereas λ has gone over a stair, for SNR $\in [2.50\text{db}; 2.98\text{db}]$: the reduced trajectory does not converge to any fixed point, limit cycle or quasi-limit cycle but to a chaotic attractor whereas λ soars to high values, for SNR $\in [2.99\text{db}; +\infty\text{db}]$: the reduced trajectory converges to a fixed point corresponding to a good decoding.

3.6 Hyperspheres method

We propose here a novel method to evaluate the unstability of the BP, based on its own trajectory in $\mathcal{E}$. This method is complementary to the Lyapunov exponent measure because it reveals the size of the attractor that the trajectory falls into and some other properties about the limit cycles. This method

consists in computing the rays R_k of the hyperspheres circumscribed to the trajectory inside a given temporal window centered around each point $T^{(k)}$.

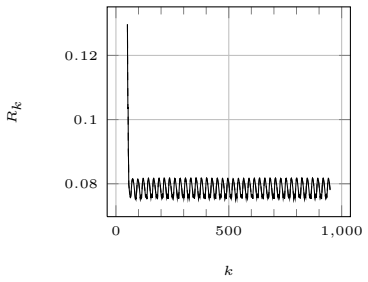

Fig. 7. Evolution of two hyperspheres rays corresponding to two initially close trajectories of the BP on the Tanner code at SNR = 2.10 dB, SNR = 2.30 dB

On the figure 7 are displayed the evolutions of two rays that correspond to two initially close trajectories in the Euclidean sense. The motion we observe for SNR = 2.30 dB is consistent with the limit cycle we observed on the reduced trajectory. The curve of the ray enables to estimate the period of the trajectory around 23 iterations. Moreover we can assert that this limit cycle is stable because the two rays cannot be distinguished. For 2.70 dB the rays moved away one from the other as it was predicted by the Lyapunov exponent observations. More accurately we can see that the rays has different oscillations step. This is due to the period doubling bifurcations explained previously. During 92 iterations in average for $k \leq 500$, the trajectory is trapped in a given limit cycle and for the next 92 iterations the trajectory falls into another limit cycle of different ray. For both it is possible to measure the period or pseudo-period that is the same as the period of the first limit cycle, that is 23 iterations. For $k \geq 500$ we cannot distinguish these different phases of evolution, the period doubling has led to chaos.

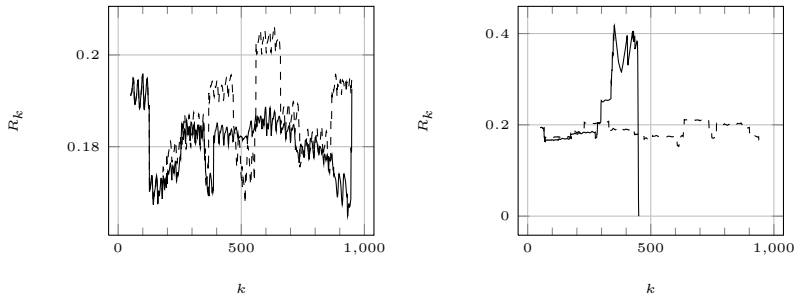

Fig. 8. Evolution of two hyperspheres rays corresponding to two initially close trajectories of the BP on the Tanner code at SNR = 2.70 dB, SNR = 3.00 dB

Such an observation makes our method relevant to bring out crucial information by a one dimensional function. Another important aspect of the hyperspheres method is the raising of the behaviors difference between two initially close trajectories: we easily observe that the evolution of the rays cannot be distinguished while $k \leq 200$ but as k is getting greater, the evo-

lution of the rays move away one from the other but they follow the same kind of motion. For both of them the hypervolumes of the state space in which they are locking in are quite of the same size. When the SNR reaches the last critical value we observe that one of the rays decreases to the null value because the BP has converged to a fixed point. The other ray has not collapsed yet because the SNR is just at the critical value, if it was increased a little we would see the two rays going to zero.

4 Conclusion

In this paper, we raised the dynamics issue of the BP by the use of known and new measures. The most important result is that the BP follows a systematic scheme when the decoding is not trivial: convergence to a small-sized attractor, locking in a limit cycle, chaos and convergence to a fixed-point. Such a property is really useful because it helps to bring out the critical values of the noise power of the channel for which the BP could present complex behaviors. Another advantage of our study is that all the measures we used can be applied on any other decoding algorithms. Therefore, we have started to create a toolbox for the dynamics study of the LDPC decoders.

References

1.R.G. Gallager. Low-Density Parity-Check Codes. *PhD Thesis, MIT*, 1963.
2.F.R. Kschischang, B. J. Frey eand H.A. Loeliger. Factor Graphs and the Sum-Product Algorithm. *IEEE Trans. on Inf. Theory*, 47.2, 2001.
3.J. Pearl. Probablistic Reasoning in Intelligent Systems: Networks of Plausible Inference. *Morgan Kaufmann publisher*, 1988.
4.H.A. Bethe. Statistical Theory of Superlattices. *Proc. Roy. Soc. London*, 1935.
5.T.J. Richardson. Error floors of LDPC codes. *Proc. 41st Annual Allerton Conf. on Comm. Cont. and Comp.*, 2003.
6.S.Y Chung, T.J. Richardson and R.L. Urbanke. Analysis of Sum-Product Decoding of Low-Density Parity-Check Codes Using a Gaussian Approximation. *IEEE Trans. on Inf. Theory*, 47.2, 2001.
7.K.P. Murphy, Y. Weiss and M.I. Jordan. Loopy belef propagation for approximate inference: an empirical study. *Proc. Uncertainty in AI*, 1999.
8.X. Zheng, F.C.M. Lau, C.K. Tse and S.C. Wong. Study of bifurcation behavior of LDPC decoders. *Int. Journal of Bifurcation and Chaos*, 16:3435–3449, 2005.
9.R.M. Tanner, R. Michael, D. Sridhara and T. Fuja. A Class of Group-Structured LDPC Codes. 2001.
10.R. Hilborn. Chaos and Nonlinear Dynamics: An Introduction for Scientists and Engineers. *Oxford University Press publisher*, 2000.
11.M.T. Rosenstein, J.J. Collins and C.J. De Luca. A practical method for calculating largest Lyapunov exponents from small data sets. *Physica D*, 65:117–134, 1993.

Proceedings, 5th Chaotic Modeling and Simulation International Conference, 12 – 15 June 2012, Athens Greece

Variable patterning in fruit fly embryos due to basins of attraction in underlying gene regulatory dynamics

Spirov, A.V.[1,2] and Holloway, D.M.[3]

[1] The Sechenov Institute of Evolutionary Physiology and Biochemistry, Saint-Petersburg, Russia.
[2] Computer Science, State University of New York at Stony Brook, Stony Brook, NY, USA.
[3] Mathematics Department, British Columbia Institute of Technology, Burnaby, B.C., Canada.

E-mail: alexander.spirov@gmail.com

Abstract: Previous work on a reaction-diffusion model of a 4-gene regulatory network governing insect segmentation characterized the dynamical basis of robustness to perturbations in this system [1,2]. Here, we computationally study system behavior near bifurcation points corresponding to weak-allele mutant embryos (i.e. with altered gene regulation). Our computations suggest that the variable expressivity and incomplete penetrance observed in some gene mutations may stem from response of the dynamical system to variable input (regulatory genes) near such bifurcation points.

Keywords: spatially extended systems, reaction diffusion, pattern formation, gene network modeling, dynamical systems, bifurcation, phase diagrams.

1. Introduction

Fruit flies (*Drosophila*) are model organisms for studying spatial pattern formation in animals. In the first few hours of development, a network of interacting genes forms expression patterns which determine the body plan. Data shows that wild-type (WT) development is remarkably robust, with various initial trajectories canalizing to an attracting state [3]. Dynamical systems analysis of a core nonlinear model of the anterior-posterior (AP) segmentation gene network has shown how this WT stability can arise as a trajectory through phase space [1,2]. The WT is stable only to a certain point, however. As CH Waddington and his colleagues showed, once an embryo's buffering capacity is overwhelmed by a sufficiently severe perturbation, altered phenotypes can arise in diverse organisms [4-6].

Strong gene mutations (deletions, insertions) can cause major (lethal) disruptions in the body plan. Our work focuses on using weaker perturbations of genes (weak alleles) to more continuously move the gene network from the WT trajectory. These gene variations can produce variable expressivity, in which the outcomes of a sample of embryos is not deterministic, but scatters between a selection of pathological outcomes (from nearly WT to strongly altered). Mutant patterns can be understood as bifurcations to pathological, non-WT, basins of attraction in a multi-stable phase space. Weak alleles bring the system to a

bifurcation point, intrinsic variability in the developmental system can then produce the variable outcomes. In this way, weak alleles can provide a tool for mapping the fine structure of the underlying phase space.

A chief focus in recent years has been to use *Drosophila* to test the positional information hypothesis [7,8], that the local concentration of a spatially-distributed gradient can specify the differentiation of cell types in the correct positions. The Bicoid (Bcd) gradient is a classic case of such a 'morphogen', but it has been discovered that Bcd gradients, compared between embryos, show much greater variability than do the patterns of one of its primary downstream targets, the zygotically expressed *hunchback* (*hb*) gap gene [9-13]. This points to error correction at the level of the initial zygotic interpretation of the maternal signal. Using 'coarse-grained' reaction-diffusion modeling, in which gene-gene interactions are simplified to single signed connections, we can study the robustness in the zygotic segmentation network via dynamical systems analysis and computations. Understanding the model components and parameters which produce the experimental pattern perturbations allows us to map the 'near-WT' phase space, and by so doing, to create a detailed understanding of the biological regulatory dynamics used in body formation.

2. Methods and Approaches

Modeling the segmentation gene network: Four gap genes, *Krüppel* (*Kr*), *giant* (*gt*), *knirps* (*kni*) and *hb*, are the core elements of our segmentation model. In *Drosophila*, these are transcriptionally activated by the maternal Bcd protein gradient in a concentration dependent manner. Three other gradients, Hb-maternal (Hb_{mat}), Caudal (Cad), and Tailless (Tll), help determine the positions of the gap genes. The combination of this upstream specification and gap-gap cross-regulation results in sharp and precise gap patterns.

Protein expression for the 4 gap genes is modeled using the gene circuit framework [1,2], producing AP concentration patterns (such as Fig. 1A). The model is computed for a one-dimensional row of nuclei, between 30 and 94% AP position (percent Egg Length, or %EL, where 0% is the anterior pole) during nuclear cleavage cycles 13 and 14A. Modeling each gene product *a* (Kr, Hb, kni, Gt) in each nucleus *i* defines a system of *number of proteins* times *number of nuclei* ODEs (Ordinary Differential Equations) given by

$$dv_i^a/dt = R_a g\left(u^a\right) + D^a\left[\left(v_{i-1}^a - v_i^a\right) + \left(v_{i+1}^a - v_i^a\right)\right] - \lambda_a v_i^a . \quad (1)$$

R_a represents protein synthesis, D_a represents diffusion, and λ_a represents decay. $g(u^a)$ is a sigmoidal regulation-expression function; for u^a below -1.5 and above 1.5 $g(u^a)$ rapidly approaches zero. u^a is given by $u^a = \sum_b T^{ab} v_i^b + m^a v_i^{Bcd} + h^a$.

Parameters T^{ab} constitute a gene interconnectivity matrix, representing activation of gene *a* by the product of gene *b* (with concentration v_i^b) if positive, repression if negative, and no interaction if close to zero. v_i^{Bcd}

represents the concentration of Bcd in nucleus *i*, which is constant in time. m^a describes the regulatory input of Bcd to each gene; Bcd is a general activator for all four gap genes considered. h^a represents regulatory input from ubiquitous factors. Our model includes Hb_{mat}, Cad, and Tll in a similar manner to Bcd, as time-independent parameters.

Stability Analysis of the Gap Gene System: The dynamics of an N variable gene circuit can be represented by behavior in an N-dimensional concentration or phase space. Time-varying solutions follow trajectories in the phase space; stable solutions are given by fixed points. In [1,2], the phase space was mapped numerically (Newton-Raphson method) and fixed points classified according to their stability ([2] Protocol S3). The positions of the fixed points and their stability properties determine the stability of a general time varying solution of the gene circuit, including bifurcation points between neighboring basins of attraction. In the present work, we computed a number of trajectories with different initial conditions to test stability and the reduction of variability. Eq. (1) was integrated for very long times in order to characterize the asymptotic behavior.

3. Results and Discussion

Non-robust patterning under perturbed parameters: Coarse-grained modeling allows us to investigate disturbances in gene-gene interaction strengths. Specifically, in [1,2] we found a set of gap network solutions (T interaction matrices, Eq. 1) which are robust to natural Bcd variability (shown in Fig. 1C). In the present work, we have used this solution set and systematically altered (in small steps) each of the 24 T^{ij} values in the solution matrices. We find cases where small parameter changes cause abrupt changes in patterning, producing severe defects from the WT-like initial solutions (Fig. 1A vs. Fig. 1B). At the borders between WT and pathological cases, we found parametric points where the Bcd variability (Fig. 1C) produces a whole range of outcomes, from nearly normal to severely defective patterns (Fig. 1B). For example, changing $T^{Kr\leftarrow cad}$ (the Cad protein effect on the Kr gene) from 0.021 to 0.035 shifts the system to the mathematical bifurcation between nearly-WT and pathological solutions (see Fig. 2). Combined with natural Bcd variability, this produces both WT and pathological patterns, as in biological variable expressivity. Our computations allow us to quantify variable expressivity as the combination of maternal (Bcd) variability and particular alterations in regulator interactions.

Visual inspection and simple statistics show the splitting between WT-like and severely defective patterns. As an illustration, Fig. 1D shows the bi-modal distribution of the Hb gap protein concentration at AP coordinate 72.5 %EL (from the data in Fig. 1B) compared to the uni-modal Bcd distribution (Fig. 1E; drawn from the data in Fig. 1C). That is, in such cases with altered T^{ij}, the natural variability in Bcd causes a subset of simulated embryos to be nearly WT, while another subset can be strongly disturbed. This behavior suggests a dynamical bifurcation.

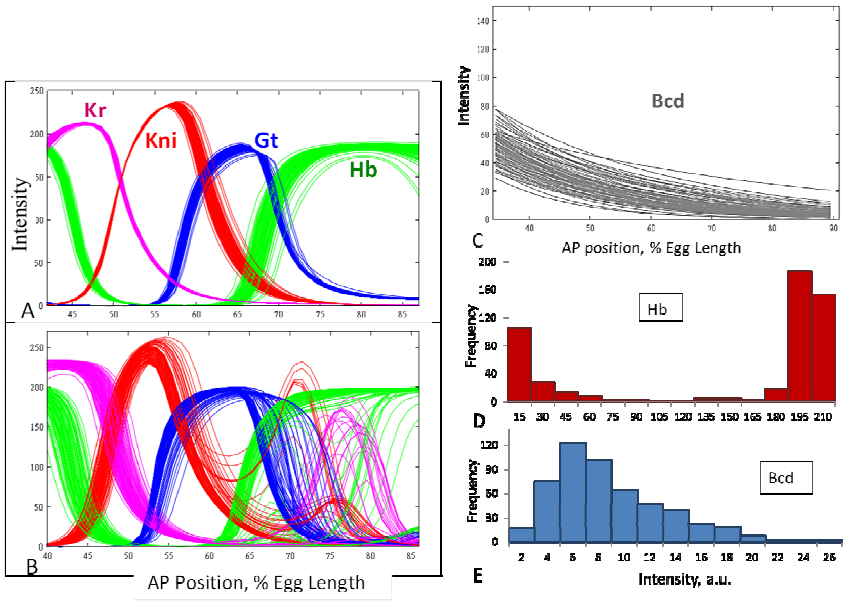

Fig. 1. Bcd-robust WT solutions vs non-robust patterning with perturbed parameters. A) From [1,2] we have a set of gap network solutions (T interaction matrices) which are robust to natural Bcd variability. B) Changing $T^{Kr \leftarrow cad}$ (Cad protein effect on Kr gene) from 0.021 to 0.035 shifts the system to the mathematical bifurcation between WT and pathological solutions. C) The natural variability of the Bcd profiles used to test solution robustness. D,E) Comparison of the bi-modal distribution of the Hb gap protein with the uni-modal Bcd distribution, at AP coordinate 72.5 %EL.

Bifurcation analysis of the incomplete penetrance solution in comparison with the published results [1,2] shows that this new behavior does corresponds to a bifurcation. For the example of changing (mutating) $T^{Kr \leftarrow cad}$, the system is shifted to the border between the old robust WT-like region of phase space and the new pathological one. Fig. 2 compares the two phase portraits at 72.5%EL in Gt, Hb, Kr coordinates, for the robust WT solution of [1,2] and for the mutant solution described here. The robust WT dynamics are characterized by a saddle-node combination (Fig. 2A; c.f. Fig. 4BE, [2]). For the mutant case, at the same AP position (72.5%EL), a second saddle-node combination appears by bifurcation (Fig. 2B). The particular attractor (node) the model reaches depends on the particular shape of the Bcd gradient. The two attractors correspond to the bi-modal distributions for Hb & Kr (both, very low vs. very high; c.f. Fig. 1D and Fig. 2B), while Gt does not show such drastic differences (see Fig. 1B).

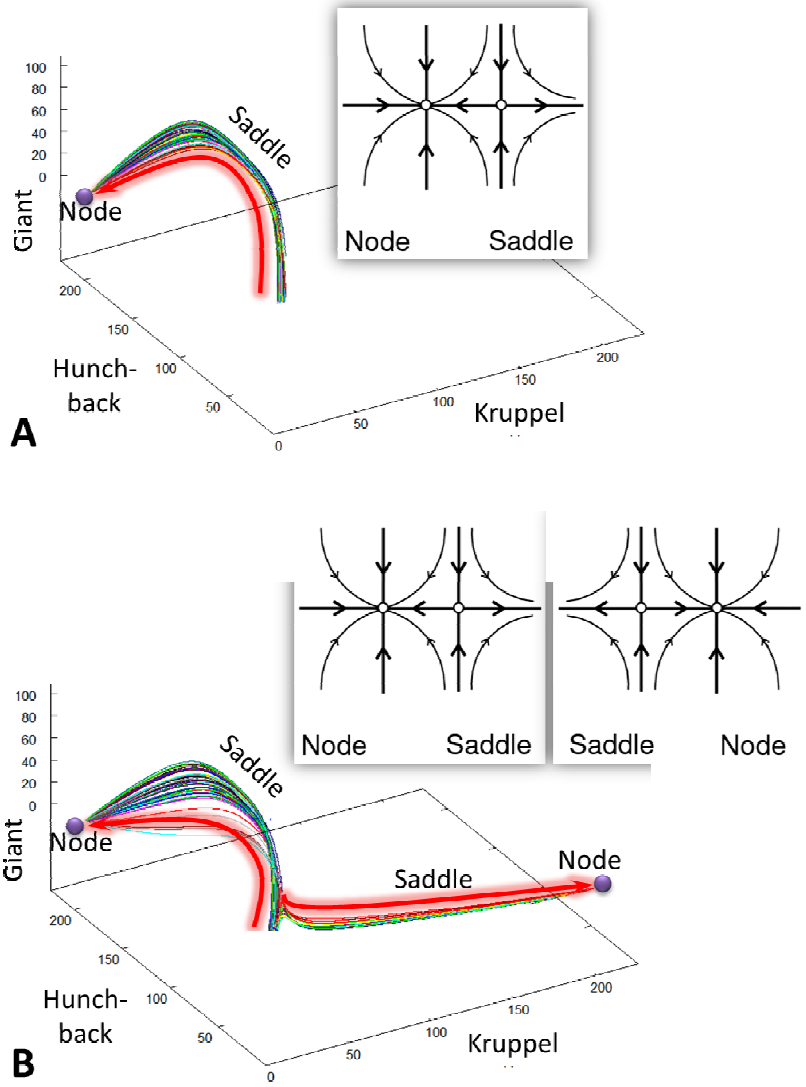

Fig. 2. Phase portraits at 72.5% EL (in Gt, Hb, Kr coordinates). A) Robust WT dynamics. The dynamics here are controlled by a saddle-node combination. B) Mutant behavior. A second saddle-node combination has appeared by bifurcation. The particular attractor (node) the model reaches depends on the particular shape of the Bcd gradient. Other nodes non-essential for this behavior have been omitted. The red bent arrows show the movements of all solutions tested, from initial points to final steady states (at the purple nodes).

4. Conclusions

Building on our previous work, we have shown here how mutation of gene-gene interactions can lead the *Drosophila* segmentation gene network to a bifurcation point, at which natural maternal variability can push embryos into neighboring basins of attraction. Such variable expressivity or incomplete penetrance is observed in nature, but the causes have been elusive. Our work suggests a dynamical basis, in which a weak mutation takes the system to a bifurcation point, and the variable outcomes are a manifestation of natural variability in upstream control; i.e. the mutation removes the robustness of the gene network to maternal variability.

Acknowledgements

This work supported by NIH grant R01-GM072022.

References

1. Manu, Surkova S, Spirov AV, Gursky VV, Janssens H, Kim A-R, Radulescu O, Vanario-Alonso CE, Sharp DH, Samsonova M, and Reinitz J (2009a). Canalization of Gene Expression in the Drosophila Blastoderm by Gap Gene Cross Regulation, PLoS Biology, PLoS Biol 7(3): e1000049.
2. Manu, Surkova S, Spirov AV, Gursky VV, Janssens H, Kim A-R, Radulescu O, Vanario-Alonso CE, Sharp DH, Samsonova M, and Reinitz J (2009b). Canalization of Gene Expression and Domain Shifts in the Drosophila Blastoderm by Dynamical Attractors, PLoS Computational Biology, PLoS Comput Biol 5(3).
3. Surkova S, Kosman D, Kozlov K, Manu, Myasnikova E, Samsonova AA, Spirov A, Vanario-Alonso CE, Samsonova M, and Reinitz J (2008). Characterization of the Drosophila segment determination morphome. Dev. Biol. 313, 844-862.
4. Waddington CH (1953). Genetic assimilation of an acquired character. Evolution 7, 118-126.
5. Waddington CH (1956). Genetic assimilation of the bithorax phenotype. Evolution 10, 1-13.
6. McLaren A (1999). Signalling for germ cells. Genes Dev. 13, 373 – 376.
7. Wolpert L (1969). Positional information and the spatial pattern of cellular differentiation. J Theor Biol 25, 1-47.
8. Wolpert L (2002). Principles of development, 2nd Edition. Oxford University Press.
9. Houchmandzadeh B, Wieschaus E, and Leibler S (2002). Establishment of developmental precision and proportions in the early Drosophila embryo. Nature 415, 798-802.
10. Spirov A.V. and Holloway D.M., (2003), Making the body plan: precision in the genetic hierarchy of Drosophila embryo segmentation, In Silico Biology, 3, 89-100
11. Gregor T, Tank DW, Wieschaus EW, and Bialek W (2007a). Probing the limits of positional information. Cell 130, 153-164.
12. Gregor T, Wieschaus EW, McGregor AP, Bialek W, and Tank DW (2007b). Stability and nuclear dynamics of the bicoid morphogen gradient. Cell 130, 141-152.
13. He, F., Wen, Y., Deng, J., Lin, X., Lu, L.J., Jiao, R., and Ma, J. (2008). Probing intrinsic properties of a robust morphogen gradient in Drosophila. Dev. Cell 15(4): 558-567.

Proceedings, 5th Chaotic Modeling and Simulation International Conference, 12 – 15 June 2012, Athens Greece

Application of planning artificial neural networks in solver of tasks of intellectual self-organizing automatic-control systems

Michail F. Stepanov, Andrew M. Stepanov

Saratov State Technical University, Saratov, Russia
E-mail: mfs@sstu.ru

Abstract: Expansion of orbs of application (appendix) of automatic control has caused development of intellectualization of control systems. One of the important directions are intelligent self-organizing system of automatic-control (ISSAC). They are capable to supply required capabilities of the purpose of control with change of environments and/or their parameters). It is attained by automatic synthesis of the law of control, the most adequate a current situation. For this purpose the intelligent system of synthesis is used. The planning subsystem creates (in the elementary case selects from already known) the most adequate procedure of synthesis. However existing approaches to planning actions have no property of mass parallelism. It do not allow to apply them in control systems owing to the big costs of time for a solution of task. It is offered to use planning artificial neural networks (PANN) within the planning subsystem of tasks solver. Features of planning of tasks solvings with use PANN are considered. Outcomes of simulation of control by a population of plants with use ISSAC are represented.
Keywords: planning artificial neural networks, simulation of intellectual control systems.

1. Introduction

Increasing thickening of objects of control in a combination with toughening requests to accuracy and quality of control has reduced to an inconsistency with traditional approaches to construction of control systems. Modern control systems, as a rule, are working (function) in interacting with other systems which can influence on their behavior. The problem is complicated that, those conditions of functioning of control systems are changing during their work. It concerns not only the change of controlled plants and environments of their functioning, but also and the purposes of control. Necessity of organization of interacting of a set of the control systems a population of probably interconnected controlled plants essentially complicates a task of control.

2. Intelligent self-organizing control systems

It is expedient to apply the approach based on usage of intellectual systems of synthesis of the law of control to a solution of the indicated problem [1]. Such systems for a solution of a specific task of synthesis of the law of control in the beginning create a program of a solution of the task as ordered population of elementary operations and executing them make the required law of control. The amount of the elementary operations used for task solving of synthesis of the law of control, is not big, as they represent procedural definition of concepts

of the theory of automatic control (TAC) [2]. Creating of the program a solution of the task is carried out based on knowledge of methods of task solving of the theory of automatic control. For this purpose are traditionally used a tools of automatic theorem proving. It is known, that tasks of scheduling of operations or automatic theorem proving are difficultly for deciding and them referred to category of NP-challenge. For such tasks of an expenditure of resources by searching of a solution will increase under the exponential law with growth of complexity of the task. Thus the most perspective are multilevel systems in which at the expense of introduction of hierarchically interconnected spaces are narrowed down of area for searching a solution of the task. Intelligent self-organizing control systems are understood as systems of automatic control, capable to self-organizing by means of a modification of the law of the control, using methods of an artificial intelligence [3].

Structure of an intelligent self-organizing system of automatic control (see fig. 1): the measuring subsystem, the executive mechanisms, the calculator of control action, the subsystem of identification of models of plant of control and environment based on the data of a measuring subsystem, the block of shaping of the purpose of control on the basis of the own purposes of behavior and an emotional state of an intelligent self-organizing control system, the intellectual subsystem of synthesis of the law of control, the block of a self-estimation realizing an evaluation of a quantitative equivalent of quality estimate ("emotion") of behavior of this intellectual self-organizing system of automatic control, formed on the basis of a self-estimation and the estimations obtained from higher hierarchy levels of control systems.

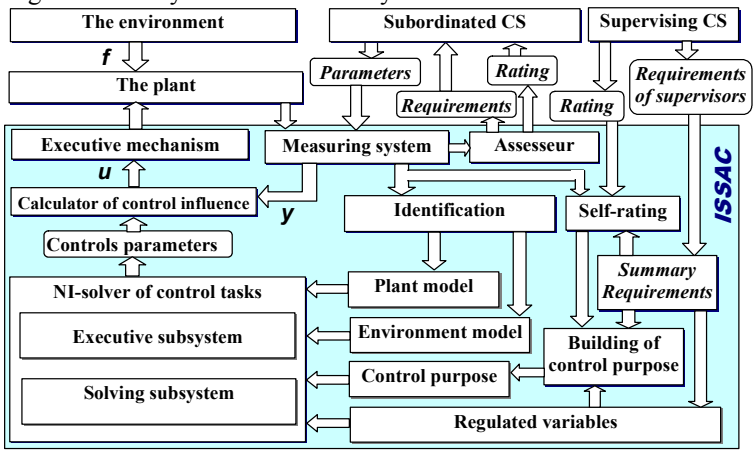

Fig. 1. Structure of an intelligent self-organizing system of automatic control

Setting of the task of synthesis of the new law of control includes exposition of known components of a control system, an environment and the purpose of control, not specifying of a method (procedure) of a solution of the task, i.e. *none procedurally*. The set of methods of synthesis and the analysis of control systems are more not very important yet. More important becomes are

availability of capabilities of tools by automatically definition are methods, relevant to the current task.

The problem of an automatic solution non procedural tasks in view demands engaging intelligent tools, understanding under a word "intelligent" ability to decide new tasks [4]. Therefore, the subsystem of automatic synthesis of the law of control of a self-organizing control system should represent the intelligent system of automatic synthesis using methods of an artificial intelligence for preliminary construction of the schedule of a solution of a specific target of synthesis. The new law of control is formed as a result of execution of the constructed plan of action. Thus, most a gorge is the mechanism of scheduling of operations. It is stipulated by that methods used now have no property of mass parallelism, and, therefore, «*the damnation of dimension*» is inherent in them, not permitting to solve tasks of practical complexity.

The complex solution of the indicated problems is known on the basis of the methodology *of automatic* problem solving the theory of automatic control including [2], [3]: 1) *formalizing* knowledge of methods of problem solving of synthesis and analysis control systems as multilevel model of a set of formalized tasks (MMSFT) TAC [2]; 2) construction *of a planning* subsystem as the system of automatic theorem proving representing the application system of calculus of sequent [4], [5] and called as the multilevel axiomatic theory of automatic solutions of formalized tasks (MATASFT) TAC [2], [3]; 3) usage *of planning artificial neural networks* (PANN) [2], [3], [6] as a search engine of output in formal axiomatic systems; 4) Result of the planning (schedule) of a solution of the task is the program on the problem oriented language "Instrument - OP", which supporting a paradigm «rules IF-THEN» [2]; 5) construction *of the executive* subsystem as the application package controlled by the interpreter of the language "Instrument - OP".

Multilevel model of a set of formalized tasks of TAC is $M_O =< \Pi, Д, O >$, were $\Pi = \{\text{п}_i \mid \text{п}_i =< P_i, H_i, \Psi_i, Q_i >,\ P_i \subseteq \wp, H_i \subseteq \aleph, \Psi_i \subseteq \Im, Q_i \subseteq \Pi\}$ – set of the formalized generalizations of control system components called as *subjects* and possessing: *properties* $p_j \in P_i \subseteq \wp = \{\rho \mid \rho = \{true \mid false\}\}$; *characteristics* $h_j \in H_i \subseteq \aleph = \{\chi_k \mid \chi_k \in \mathbf{C}^{n_k}, n_k \in \mathbf{N}\}$, **C**, **N** – sets complex and natural numbers accordingly; *forms* of mathematical models $m_j \in \Psi_i \subseteq \Im = \{\mu_1, ..., \mu_\tau\}$; *components* $q_j \in Q_i \subseteq \Pi$; $Д = \{\text{д}_i \mid \text{д}_i : \wp \cup \aleph \cup \Im \to \wp \cup \aleph \cup \Im \cup O\}$ – set of operations for processing attributes of subjects; $O = \{o_i \mid o_i : \wp \cup \aleph \cup \Im \to \{true \mid false\}\}$ – set of the predicates defined on attributes of subjects. *Actions* $\text{д}_i = \langle c_i, d_i, r_i, g_i \rangle \in Д$ and *relations* $o_i = \langle c_i, d_i \rangle \in O$ are uniquely identified by the attributes $c_i \in \wp \cup O$ – conditions of applicability,

$d_i \in \wp \cup \aleph \cup \Im$ – source data, $r_i \in \wp \cup \aleph \cup \Im \cup O$ – results of an action, $g_i \in O$ – requirements to results of an action. With a view of a raise of effectiveness multilevel representation of knowledge as a three-rank system of submodels is used, each of which has three-level representation of knowledge: $M = \langle M^1, M^2, M^3 \rangle$, $M^1 = \langle M_1^1, ..., M_m^1 \rangle$, $M^2 = \langle M_1^2, ..., M_n^2 \rangle$, $M^3 = \langle M_1^3 \rangle$, $M_i^r = \langle M_{0,i}^r, M_{1,i}^r, M_{2,i}^r \rangle$, $M_{k,i}^r = \langle \Pi_{k,i}^r, Д_{k,i}^r, O_{k,i}^r \rangle$, were M^r - model of r-th rank; M_i^r - i-th submodel of r-th rang; $M_{k,i}^r$ - i-th submodel of k-th level of r-th rank; $\Pi_{k,i}^r$ – set of subjects, $Д_{k,i}^r$ – set of actions, $O_{k,i}^r$ – set of relations of submodel $M_{k,i}^r$. The multilevel model *of M* is created by the scientists on the basis of model M_O by means of multistep generalizations of knowledge [2], [4]. The planning subsystem is the formal logical system representing the application system of calculus of sequents [4], [5], called *as the multilevel axiomatic theory of automatic solutions of formalized tasks (MATASFT)* TAC [2]: $T = \langle T_1^1, ..., T_m^1, T_1^2, ..., T_n^2, T_1^3 \rangle$, $T_i^r = \langle T_{0,i}^r, T_{10,i}^r, T_{1,i}^r, T_{21,i}^r, T_{2,i}^r \rangle$, were T_i^r – *i*-th three-level theory of solutions *r-th* rank; $T_{0,i}^r, T_{1,i}^r, T_{2,i}^r$ – *i*-th single-level theories of solutions 0-th, 1-th, 2-th levels *r*-th rank; $T_{10,i}^r, T_{21,i}^r$ – the translational theories linking 1-th and 0-th, 2-th and 1-th levels of *r*-th rank. Theory *T* is automatically generated [4] on the basis of multilevel model *of M* under the following scheme: subjects of models $\mathrm{M}_{\mathrm{k,i}}^{\mathrm{r}}$ will be converted to variable theories of solutions $\mathrm{T}_{\mathrm{k,i}}^{\mathrm{r}}$, actions – in axioms, a sheaf between subjects – in axioms of translational theories $\mathrm{T}_{\mathrm{kk\text{-}1,i}}^{\mathrm{r}}$. Specificity of data domain TAU has stipulated presence in theories of solutions $\mathrm{T}_{\mathrm{k,i}}^{\mathrm{r}}$ of the own axioms with source data, a required results, conditions for applicability, but also the requirements to results. Therefore production rules of theories of solutions $\mathrm{T}_{\mathrm{k,i}}^{\mathrm{r}}$, in addition to rules systems G4 [2], include the special production rules, which making (playing) a main role during scheduling of solving of task [3].

Scheduling of problem solving of synthesis of control system is complicated that at a stage of scheduling the values of many parameters of models of components of control system are unknown, they will defined only during executing of the scheduled program of a solution of the task. Therefore the developed schedule should include all alternate paths of a solution, choice of the most approaching from which is carried out immediately already at executing of

the scheduled program of a solution of the task. Therefore, for example, it is obvious, that before realization of any operation having conditions of applicability, values of appropriate logical expressions should be checked. On the other hand, after realization of operations with requirements to outcome it is necessary to check realization of the indicated requirements. Therefore, in the schedule of a solution of the task, in addition to the operations forming required outcome, should switch on as well the operations computing values of appropriate relations. Thus if requirements to required outcome appear outstanding then actions for elimination of a discordance should be undertaken. A common guideline on this score does not exist, as specificity of problem area here should be taken into account. In our case it reduces in include (appearance) in theories of solutions of axioms for which in conditions of applicability are indicated negation of requirements to outcome. Thus, the operation that was defined by such axiom should be applied to support of realization of requirements to outcome if it became known, that these requirements are not fulfilled. Bypass of "the damnation of dimension" can realize the *planning artificial neural networks* (PANN) [2], [3], [6] which possessing property of mass parallelism. Structurally PANN consist of *resolving artificial neural networks* (RANN) and *archive artificial neural networks* (AANN). The device of synchronization (see fig. 2) coordinates their operation. RANN is representing a three-layer network. She fulfills an inverse method of search of a solution of the task in a formalism of used fragment MATASFT TAC. The constructed schedule of a solution of the task is saved in AANN. RANN is a dynamic artificial neural network. Values on the output are varying with the constant signals on inputs. The initial state of all neurons RANN is not active.

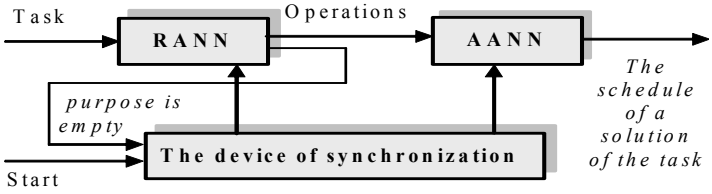

Figure 2. Structure of a planning artificial neural web, where: RANN -resolvelly artificial neural network (ANN), AANN - an archival artificial neural network

For the tasks having a solution, the separate neurons of an outputs layer of RANN short-term are going to an active (excited) state, which then is remembered in AANN for the subsequent inclusion in the schedule of a solution of the task. Values of outputs of neurons of one of interior layers of neurons of RANN is interpreted as values of the searching's purposes of a solution of the current task. Passage of these neurons in a non-active state reduces to appearance (generation) of signal, «the purpose is empty». It means that the solution of a task was obtained. Otherwise, on expiration of the solution time assigned on searching (an amount of pitches), the refusal to search a solution will be made. PANN allows solving simultaneously all subtasks of the source task, forming a united plan of a solution. On paths of usage of neural networks

always, it is necessary to solve two problems: preliminary tutoring of a web and interpretation of the obtained outcomes. In PANN both problems are solved by virtue of design features. Basic difference of the given approach is *automatic* generation MATASFT TAC, and after her and PANN on the basis of assigned MMSFT TAC. Instead of traditional tutoring of the neural network, the procedure of automatic creation (result) of the PANN is used based on the appropriate fragment MATASFT TAC, which is called as the single-level theory of solutions. The main idea of the procedure of creation of the PANN consists in shaping a neural network which stratums are compared with units of the single-level theory of solutions. Implementation on basis PANN of a planning subsystem of an intellectual system of automatic task solving of TAC was called as Naturally - Intellectual Solver (NI-solver) of tasks of TAC [2].

3. Research of intellectual self-organizing systems of automatic control

The offered concept of automatic task solving of TAC based on planning artificial neural networks has served as methodological base for creation of a system of simulation of intellectual self-organizing systems of automatic control. The task of simulation of intelligent self-organizing systems of automatic control refer to category rather complicated, because includes not only immediate control of the set plant, but also simulation of the intelligent behavior used for the purposes of self-organizing. Therefore, usage of universal software for simulation of such systems in full appeared unacceptable.

Such specialized resource is MISACS - a system of Modeling of Intelligent Self-organizing Automatic Control Systems [3]. MISACS it is intended for research of processes of control by a population probably interconnected and cooperating plants, controlled by the intelligent self-organizing systems of automatic control (ISSAC) organized in hierarchically connected structure.

MISACS gives the user the following possibilities in a graphics interactive regime: 1) To set an amount of levels of hierarchy of population ISSAC, an amount of plants of control and ISSAC in each level; 2) To install connections between plants of control and assigned for them ISSAC; 3) To set criteria of a self-estimation of behavior ISSAC (engineering, analytical); 4) To define MATASFT TAC for everyone ISSAC separately.

We research possibilities ISSAC for control of non-stationary plant (see fig. 3). Let the plant of control is described by the following equations:

$$\dot{x} = (A + \Delta A)x + u^* + Mf,\ x \in R^n,\ u \in R^n,\ f \in R^\mu,\ n = 3,\ \mu = 1,$$

$$\Delta A = [0]_n,\ 0 \le t < t_0,\ \Delta A = dA \times \sin(\omega \times (t - t_0)),\ \forall t \ge t_0$$

$$A = \begin{bmatrix} 0 & 1 & 0 \\ 0 & -300 & 1000 \\ 0 & -3 & -1 \end{bmatrix},\ M = \begin{bmatrix} 0 \\ 0 \\ 1 \end{bmatrix},\ dA = \begin{bmatrix} 0 & 0{,}1 & 0 \\ 0 & 250 & -700 \\ 0 & 2{,}5 & 0{,}7 \end{bmatrix},$$

$$f = \begin{cases} f_0, & 0 \le t < t_s \\ f_0 + f_m \times \sin(\omega_f \times (t - t_s)), & \forall t \ge t_s \end{cases},$$

were $t_0 = 4$ – the moment of the beginning of a modification of model of plant of control; ω – frequency of a modification of model of plant of control; $f_0 = 1{,}0$ – magnitude of stepping component exterior perturbation; $f_m = 0{,}25$ – amplitude of sine waves of the exterior perturbation; ω_f – frequency of sine wave of the exterior perturbation; $t_s = 5$ – the moment of inclusion of sine wave of the exterior perturbation; $[0]_n$ – zero matrix $n \times n$.

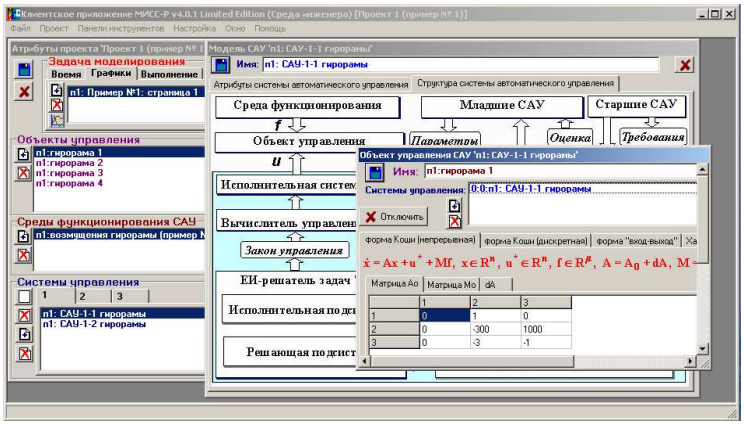

Fig. 3. Attributes of the project of simulation

The purpose of control is set as requirements on the statically errors of controlled variables:

$$\theta = Nx, \theta \in R^z, N = \begin{bmatrix} 1 & 0 & 0 \end{bmatrix}, \qquad \left|\theta_{\text{уст}_i}\right| \le \theta^*_{\text{уст}_i}, \ \theta^*_{\text{уст}}, \theta_{\text{уст}} \in R^z,$$

$\theta^*_{\text{уст}_1} = 0{,}5$ at presence of stepping exterior perturbations $f_0 = 0{,}5$.

The initial law of control was synthesized counting upon stepping exterior perturbation $f_0 = 0{,}5$. Therefore with perturbation $f_0 = 1{,}0$ of the requirement to exactitude of regulating at the disconnected self-organizing are not fulfilled even for stationary plant (a curve 1 on fig. 4). Inclusion of self-organizing in an instant $t_c = 10{,}0$ with periodicity in 1 second and with a velocity of self-organizing **0,17** eliminates a problem, ensuring a required exactitude of regulating (a curve 2 on fig. 4). The transient for non-stationary plant of control at the disconnected self-organizing is mirrored with a curve 3 on fig. 4. Inclusion of self-organizing with the same parameters ensures a required exactitude of regulating and for non-stationary plant (a curve 4 on fig. 4).

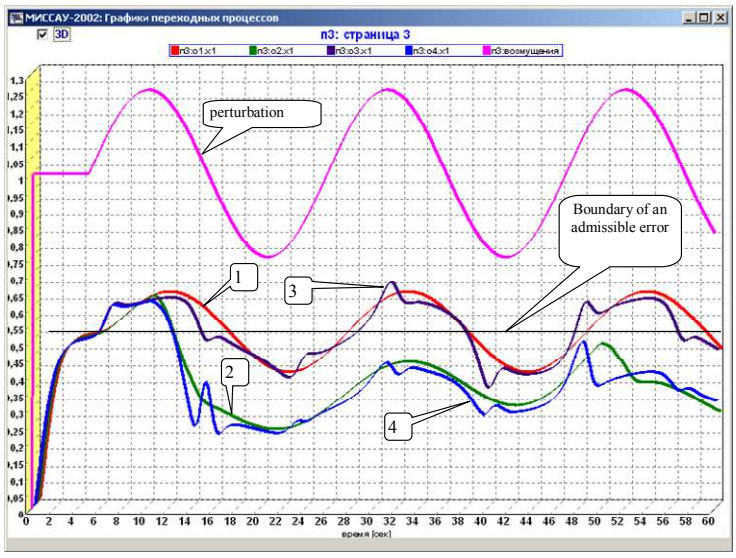

Fig. 4. Control of non-stationary plant

3. Conclusions

Tools of self-organizing ISSAC successfully compensate modifications of plant of control and an environment by means of use of new more exact law of control with the help of an intellectual system of automatic synthesis of the law of the control, based on (having) used neural computing organization based on planning artificial neural networks.

References

1. M. F. Stepanov. Intelligent self-organizing systems of automatic control - a triad "the theory of automatic control - information process engineering - an artificial intelligence" // Information process engineering. Moscow, 2001. № 11.
2. M. F. Stepanov. Automatic solution of the formalized tasks (problems) of the theory of automatic control. Saratov state technical university. Saratov, 2000.
3. M. F. Stepanov. Intelligent self-organizing automatic-control systems. Saratov state technical university. Saratov, 2002.
4. E. I. Efimov. The solvers of intellectual tasks. Science, Moscow, 1982.
5. G. Genzen. Researches of logical inferences // The mathematical theory of the logical inference. - Science. Moscow, 1967.
6. M. F. Stepanov. Problem solving of the theory of automatic control on the basis of planning artificial neural networks // Neurocomputers: design and applications, 2003. № 3-4. Pp. 27 – 44.


Proceedings, 5th Chaotic Modeling and Simulation International Conference, 12 – 15 June 2012, Athens Greece

Dynamics of a Jeffcott Rotor with Rigid Blades Rubbing against an Outer Ring

Florian Thiery and Jan-Olov Aidanpää

Luleå University of Technology, 971 87 Luleå, Luleå, Sweden
(E-mail: florian.thiery@ltu.se,jan-olov.aidanpaa@ltu.se)

Abstract. The non-linear behaviour of rub-impact systems have been studied recently by approximating rotor-stator systems as rubbing cylinders. In reality, the rotor shape is more complex, resulting in richer dynamics over smaller parameter ranges. In this paper, a bladed turbine is modelled using a Jeffcott rotor with three rigid beams attached to the mass center. The contact forces are described by a radial restoring force induced by the massless outer ring, and a tangential Coulomb frictional force. The results are presented in bifurcation diagrams and compared with a previous model described by three flexible beams entering in contact with a fixed ring assuming large displacement beam theory. This paper shows that the two models described give similarities in the overall bifurcation diagram, only showing greater differences in localized frequency ranges.

Keywords: Nonlinear, Rotor-dynamics, Jeffcott, Blade, Impact.

1 Introduction

In rotor dynamics, several types of configuration can lead to non-linear dynamics. One of them is the rub-impact systems having a high degree of non-linearity, which may lead to unwanted vibration. Many studies have been performed on the Jeffcott rotor with rubbing cylinders. For instance, Karpenko *et al.*[1] presented the effect of mass imbalance of a nonlinear rotor system with bearing clearances, as well as the case of a preloaded snubber ring [2]. Popprath and Ecker[3] studied the effect of stator damping for a similar rotor-stator system. In these types of models, complex dynamics always occur above the natural frequency of the system [4].

On the contrary, fewer studies have been performed in the case of bladed turbines which can be of interest in different industrial applications. Complex FEM blade models have been studied by Legrand *et al.*, but not over complete parameter ranges due to the model sophistication. Nonetheless, a rubbing Jeffcott rotor with three blades has been developed by Aidanpää and Lindkvist[5], showing that complex dynamics can occur below the natural frequency, especially at integer fractions of $\omega_n/3$. An accurate description of this model will be made and compared with the simplified model assumed in this paper. As the model described in [5] is rather complex due to solving equations for non-linear beam deformations, it is of interest to evaluate if a simpler model could be used and find its limitation.

2 Rotor Model

The model of the bladed Jeffcott rotor is given in Figure 1. The mass of the rotor is m with external damping c and stiffness k for the massless shaft. The three blades are assumed to be massless and rigid, equally spaced and of length L. The blades are rotating in a rigid ring of radius R attached to two springs of value k_1. The rotor is rotating with an angular velocity ω. When the blades enter in contact with the outer ring, the contact forces are described by a force P normal to the circle delimited by the ring, and a tangential force μP at the contact point where μ is a friction coefficient (Coulomb friction). The mass of the ring is neglected, as well as damping so that the outer ring returns to its initial position instantaneously. The nonlinear behaviour of the system is caused by the sudden change in stiffness when a blade gets in contact with the outer ring.

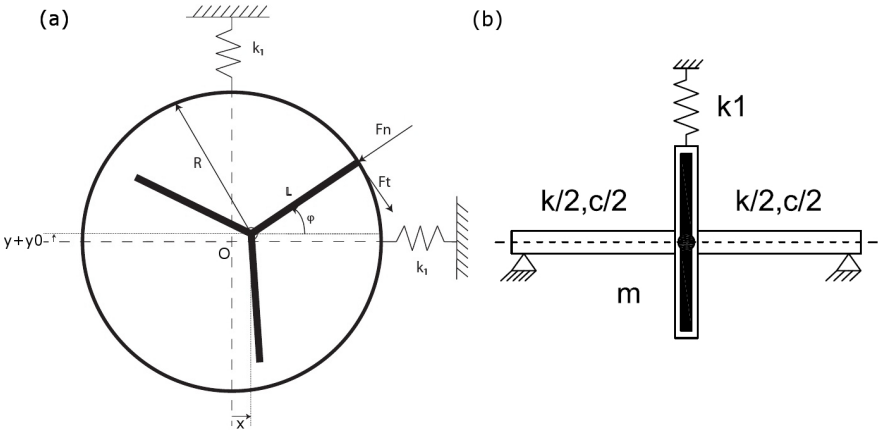

Fig. 1. (a) Side view of the bladed Jeffcott rotor (b) Overview of the Jeffcott rotor.

For the first blade, the position of the tip is expressed by the following vector

$$\mathbf{r} = (x + L\cos(\omega t))\mathbf{i} + (y + y_0 + L\sin(\omega t))\mathbf{j} \tag{1}$$

where ($\mathbf{i}$, $\mathbf{j}$) is a fixed base of the system in the x and y direction. For any blade, the position vector can be written in a same way by replacing the phase ωt by $\omega t + 2\pi(k-1)/3$ for $k = \{1, 2, 3\}$. The displacement y_0 is the initial eccentricity in the y direction. The condition for one of the k-th blade to be in contact is given by $\|\mathbf{r}_k\| = R$. It is assumed that only one blade enter in contact with the ring at the same time. The force generated by the contact can be decomposed in a normal force acting towards the origin of the coordinates system O and a force tangent to the ring with a direction

depending on the tangential contact velocity v_c^k of the corresponding blade. For the first blade, the normal contact force $\mathbf{F}_n$ is given by

$$\mathbf{F}_n = -k_1 \Delta r \frac{\mathbf{r}}{\|\mathbf{r}\|} \tag{2}$$

, while $\mathbf{F}_t$ is obtained by a rotation of $\pi/2$ of $\mathbf{F}_n$ and having a norm $\mu\|\mathbf{F}_n\|$, with the direction depending on the sign of the velocity. As a result, the equations of motion are

$$\begin{cases} m\ddot{x} + c\dot{x} + kx = (\mathbf{F}_n^k + \mathbf{F}_t^k).\mathbf{i} \\ m\ddot{y} + c\dot{y} + ky = (\mathbf{F}_n^k + \mathbf{F}_t^k).\mathbf{j} \end{cases} \tag{3}$$

when the k-th blade is in contact with the rotor ($\|\mathbf{r}_k\| = R$). For the no contact case ($\forall k \ \|\mathbf{r}_k\| < R$), the right side term of equation (3) is null. By writing them in a matrix form, using the Heaviside function $H(.)$ and sign function sgn(.) gives

$$\begin{bmatrix} m & 0 \\ 0 & m \end{bmatrix} \begin{bmatrix} \ddot{x} \\ \ddot{y} \end{bmatrix} + \begin{bmatrix} c & 0 \\ 0 & c \end{bmatrix} \begin{bmatrix} \dot{x} \\ \dot{y} \end{bmatrix} + \begin{bmatrix} k & 0 \\ 0 & k \end{bmatrix} \begin{bmatrix} \dot{x} \\ \dot{y} \end{bmatrix} = -H(\|\mathbf{r}_k\| - R) \times k_1 \times$$
$$(1 - \frac{R}{\|\mathbf{r}_k\|}) \begin{bmatrix} 1 & -\mu \operatorname{sgn}(v_c^k) \\ \mu \operatorname{sgn}(v_c^k) & 1 \end{bmatrix} \begin{bmatrix} x + L\cos(\omega t + 2\pi(k-1)/3) \\ y + y_0 + L\sin(\omega t + 2\pi(k-1)/3) \end{bmatrix} \tag{4}$$

The equations of motion are now ready to be solved numerically after normalization.

3 Simulation Method

In this paper, the equations of motion have been solved using a 4-th order Runge-Kutta integration with constant time step. An in-house code was implemented in C++. For bifurcation diagrams, 100 Poincare sections were collected after simulating 100 periods for a given normalized frequency $\Omega = \omega/\omega_n$. In this model, the state space dimension is 5 ($\mathbb{R}^4 \times \mathbb{S}$) with displacements x and y, velocities $\dot{x}$ and $\dot{y}$, and the phase $\varphi = \omega t$. The Poincare sections are retrieved at a constant phase $\theta_p = 2\pi$ in the state space. To plot the bifurcation diagrams, 5000 steps are used for the normalized frequency range. The final state vector of a simulation at a given frequency is used as the initial condition for the following one to find stable solutions over the whole studied range.

Concerning the maximum Lyapunov exponents, 100 periods were simulated at first to be on the attractor. The initial perturbation between the two trajectories was taken smaller than $\epsilon = 1.10^{-9}$ because of the strong non-linearities of the system and to avoid following other attractors for the

perturbed trajectory, which could lead to erroneous exponents values. A rescaling has been done for both positive and negative exponents. Threshold values were chosen to optimize the accuracy of the results and the computer speed. A number of 10000 periods were simulated to get a good convergence of the Lyapunov exponent for any frequency.

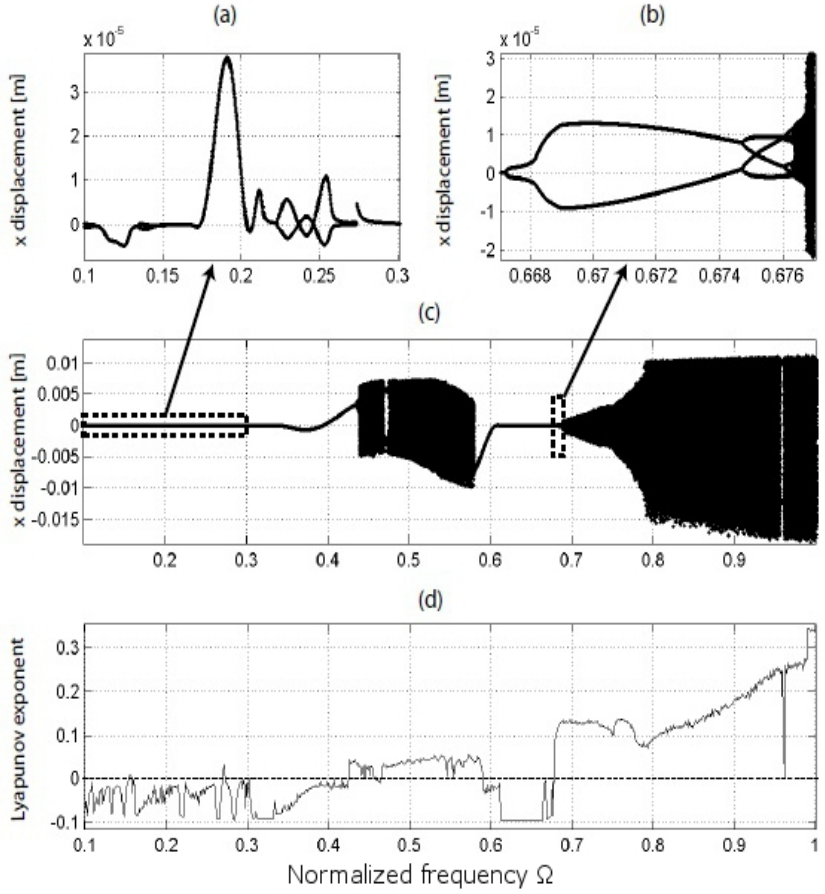

Fig. 2. (a) Bifurcation diagram - zoom 1 (b) Bifurcation diagram - zoom 2 (c) Overall bifurcation diagram (d) Maximum Lyapunov exponent

4 Numerical Results

The parameters of the system are $R = 0.11$, $L = 0.1$, $\delta = R - L = 0.01$ $m = 1$, $k = 100$, $k_1 = 15000$, $\omega_n = 10$, $\mu = 0.1$ [SI units]. These parameters are kept constant and will constitute the reference case if values are not

specified explicitly. Figure 2 (c) shows that higher vibrations start to appear at $\Omega = 0.33$, with an apparent periodic motion below this frequency. Figure 2 (c)-(d) correlates the bifurcation diagram together with the Lyapunov exponents, which allows to identify chaotic motions not visible in region ① (see Figure 3 for areas numeration). An interesting change in the diagram also appears at $\Omega = 0.666$ showing the route to chaotic motion by period doubling bifurcations from ③ to ④.

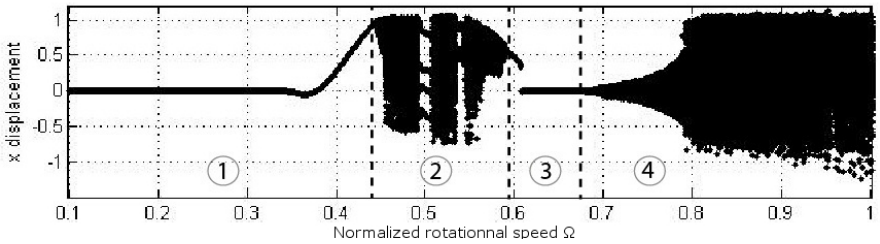

Fig. 3. Bifurcation diagram for the axially elastic blade model

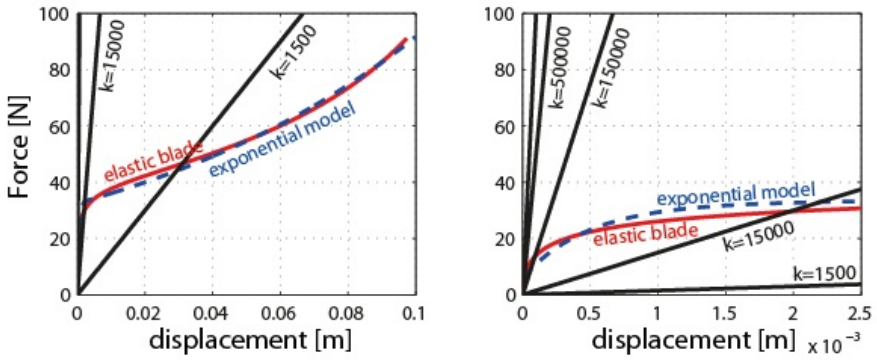

Fig. 4. Axial stiffness modelling for different simulations

The model described by [5] differs in some details and complexity. In opposition to our model, the outer ring is rigid and fixed while the blade is elastic and can be deformed axially and transversally when contacts occur by assuming large beam displacement theory. The relation between displacement and stiffness was done by polynomial curve fitting. Though the models are sensitively different, global bifurcations, periodic and chaotic motions appear in the same regions on Figure 3, with small differences becoming visible in localized frequency ranges in regions ② and ④.

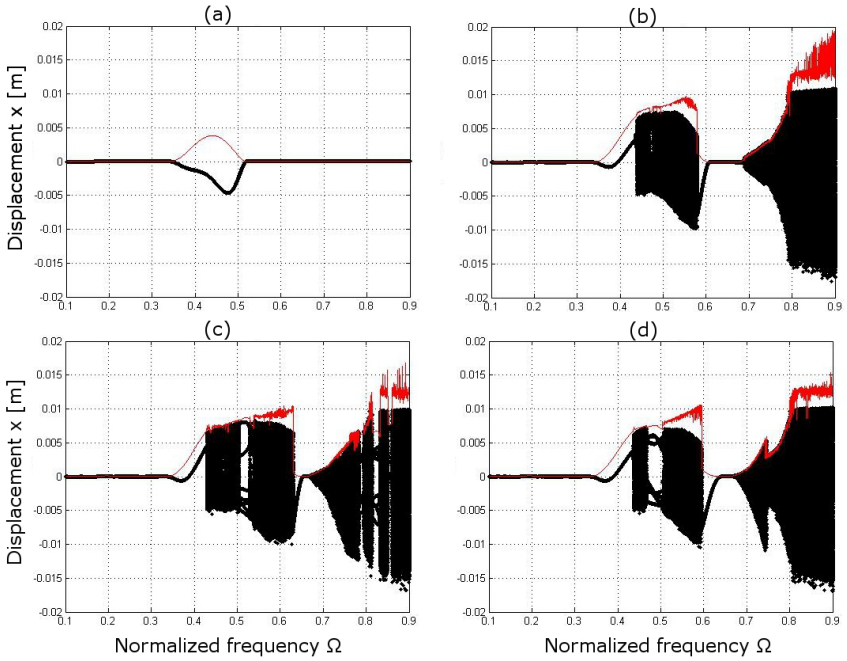

Fig. 5. Bifurcation diagram for different k_1: (a) 1.5×10^3 (b) 1.5×10^4 (c) 1.5×10^6 (d) exponential function

A model has been performed by changing the constant stiffness with an exponential fit of the axial stiffness calculated in [5]. The force-displacement fitting function is given by $F(x) = a\exp(bx) + c\exp(dx)$, with $a = 32.53$, $b = 10.36$, $c = -26.25$ and $d = -2012$. A representation of this function together with constant stiffness curves is displayed on Figure 4. It shows that the contact stiffness is extremely high for small displacements. As a result, bifurcation simulations are also performed for different constant stiffness values $k_1 = [1.5 \times 10^3; 1.5 \times 10^4; 1.5 \times 10^6]$. On Figure 5, bifurcation diagrams show similar behaviour regardless of the stiffness, excepted for the lowest stiffness (a) only showing a periodic motion over the whole frequency range. A simulation performed for a variable stiffness ratio k_1/k shows that chaotic motion appears for a stiffness ratio of 39 (at a frequency $\Omega = 0.74$). Therefore the general dynamic behaviour of the system is similar for every $k_1 \geq 3900$, but it confirms that weaker outer rings do not represent correctly the dynamics of the system under a certain threshold value. Moreover, the contact forces shown on Figure 6 vary greatly for each different stiffness k_1 by a ratio 1/100 from the smallest to the biggest value, making it difficult to know the validity of the model to get realistic contact forces as in the elastic beam model.

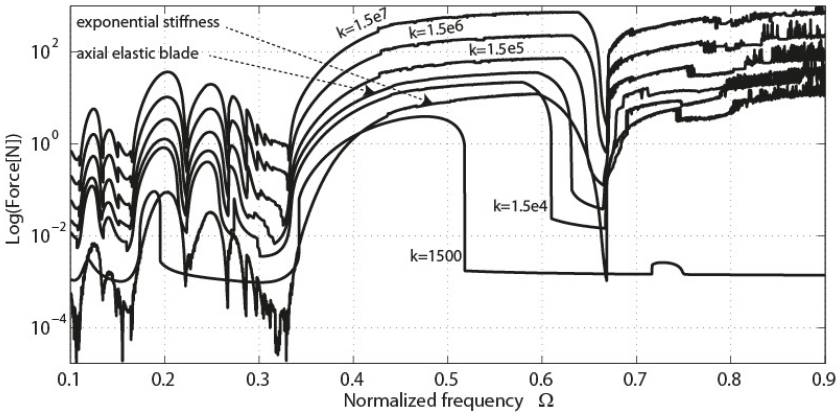

Fig. 6. Maximum force-frequency curves for different stiffness values

Regarding the influence of other parameters, tests have been performed for damping at $\Omega = 0.74$, showing that increasing damping has a stabilizing effect. Morever, complex dynamics only occur for a minimum value of the initial eccentricity $y_{0,min} = 0.010000019$, so that a reasonable value must be chosen for contacts to happen and get the system's main dynamic properties. For instance, a initial eccentricity within the range [0.0100000048-0.010000019] will only show the first chaotic range ②, while the chaotic range ④ disappears suddenly. Below this range, no significant dynamics occur at all (similar to a non-contact case).

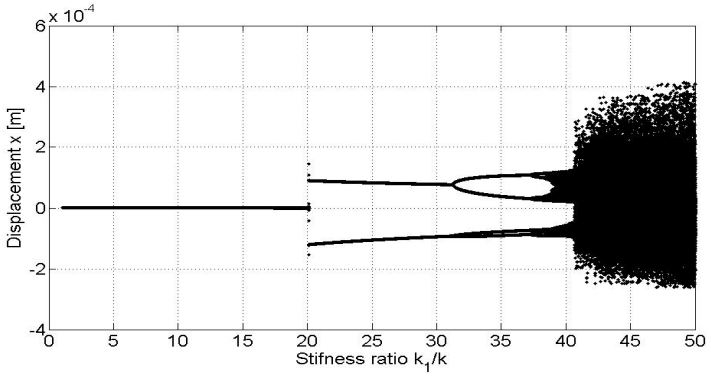

Fig. 7. Bifurcation diagram at $\Omega = 0.74$ for: (a) varying stiffness ratio (b) varying damping

5 Discussion and Conclusion

Though few studies have been performed concerning blade impacts in rotordynamics, it was shown that complex dynamics occur below the natural frequency at integer fractions of $\omega_n/3$. The present study confirms the subcited results by adopting a simpler model with different assumptions, only giving small differences in localized frequency ranges. Though the general dynamic behaviour is similar, the drawback of the new model is that no insight is given concerning forces amplitude so that validity of the model cannot be totally identified. Nonetheless, the main advantage is to evaluate the influence of the design parameters (ξ, μ, y_0, δ, k_1/k) in a faster way due to the model simplicity. From a numerical point of view, the Lyapunov exponents calculation showed sensitivity to the initial perturbation and threshold values, because of different solutions that may coexist for a fixed parameter set. Hence, jumping from one attractor to another may lead to erroneous exponents values. As a result, extraction of multiple solutions in bifurcation diagrams would allow to have better confidence in maximum Lyapunov exponents.

6 Acknowledgements

The research presented was carried out as a part of Swedish Hydropower Centre-SVC. SVC has been established by the Swedish Energy Agency, Elforsk and Svenska Kraftnät together with Luleå University of Technology, The Royal Institute of Technology, Chalmers University of Technology and Uppsala University. www.svc.nu.

References

1.E.V. Karpenko, M. Wiercigroch and M.P. Cartmell. Regular and chaotic dynamics of a discontinuously non-linear rotor system. *Chaos, Solitons & Fractals*, 13:1231-1242, 2002.

2.E.V. Karpenko, M. Wiercigroch and E.E. Pavlovskaia. Bifurcation analysis of preloaded jeffcott rotor. *Chaos, Solitons & Fractals*, 15:407-416, 2003.

3.S. Popprath and H. Ecker. Nonlinear dynamics of a rotor contacting an elastically suspended stator. *Journal of Sound and Vibration*, 308(3-5):767-784, 2007.

4.J.-O. Aidanpää. Multiple solutions in a rub-impact Jeffcott rotor. *The 10th International Symposium on Transport Phenomena and Dynamics of Rotating Machinery, Honolulu, Hawaii, March 07-11*. ISROMAC10-2004-120, 2004.

5.J.-O. Aidanpää and G. Lindkvist. Dynamics of a rubbing Jeffcott rotor with three blades. *Chaos 2010*, 58:251-259, 2010.


Proceedings, 5th Chaotic Modeling and Simulation International Conference, 12 – 15 June 2012, Athens Greece

Inversive congruential generator with a variable shift

P. D. Varbanets[1] and S. P. Varbanets[2]

[1] I.I. Mechnikov Odessa National University, str. Dvoryanskaya 2, 65026 Odessa, Ukraine
(E-mail: varb@sana.od.ua)
[2] I.I. Mechnikov Odessa National University, str. Dvoryanskaya 2, 65026 Odessa, Ukraine
(E-mail: varb@sana.od.ua)

Abstract. We give the description for elements of the sequence of inversive congruential pseudorandom numbers y_n as polynomials on number n and initial value y_0. We also estimate some exponential sums over y_n.
Keywords: inversive congruential numbers, exponential sum, discrepancy.

1 Introduction

Let p be a prime number, $m > 1$ be a positive integer. Consider the following recursion

$$y_{n+1} \equiv a\overline{y}_n + b(mod\ p^m), (a, b \in \mathbb{Z}), \tag{1}$$

where $\overline{y}_n$ is a multiplicative inversive $mod\ p^m$ for y_n if $(y_n, p) = 1$. The parameters a, b, y_0 we call the multiplier, shift and initial value, respectively.

In the works of Eichenauer, Lehn, Topuzoğlu, Niederreiter, Flahive, Sharlinski, Grothe, Emmerih ets were proved that the inversive congruential generator (1) produces the sequence $\{x_n\}$, $x_n = \frac{y_n}{p^m}$, $n = 0, 1, 2, \ldots$, which passes s-dimensional serial tests on equidistribution and statistical independence for $s = 1, 2, 3, 4$ if the defined conditions on relative parameters a, b, y_0 are accomplishable.

It was proved that this generator is extremely useful for Quasi-Monte Carlo type application (see, [3],[4]). The sequences of PRN's can be used for the cryptographic applications. Now the initial value y_0 and the constants a and b are assumed to be secret key, and then we use the output of the generator (1) as a stream cipher. By the works [1],[2] it follows that we must be careful in the time of using the generator (1).

In the current paper we give the generalization for the generator (1). We consider the following recursive relation

$$y_{n+1} \equiv a\overline{y}_n + b + cF(n+1)y_0(mod\ p^m) \tag{2}$$

under conditions

$$(a, p) = (y_0, p) = 1,\ \ b \equiv c \equiv 0(mod\ p),\ \ F(u) \text{ is a polynomial over } \mathbb{Z}[u].$$

The generator (2) we call the generator with a variable shift $b + cF(n + 1)y_0$. The computational complexity of generator (2) is the same as for the generator (1), but the reconstruction of parameters a, b, c, y_0, n and polynomial $F(n)$ is a tricky problem even if the several consecutive values $y_n, y_{n+1}, \dots, y_{n+N}$ will be revealed. Thus the generator (2) can be used in the cryptographical applications. Notice that the conditions $(a, p) = (y_0, p) = 1$, $b \equiv c \equiv 0(mod\ p)$ guarantee that the recursion (2) produces the infinite sequence $\{y_n\}$.

Our purpose in this work is to show passing the test on equidistribution and statistical independence for the sequence $\{x_n\}$, $x_n = \frac{y_n}{p^m}$, and hence, the main point to be shown is the possibility for such sequences to be used in the problem of real processes modeling and in the cryptography.

Notations: For p being a prime number

$$
\begin{aligned}
&R_m := \{0, 1, \dots, p^m - 1\},\\
&R_m^* := \{a \in R_m \mid (a, p) = 1\},\\
&e_m(u) := e^{2\pi i \frac{u}{p^m}}, u \in \mathbb{R},\\
&exp(x) := e^x \text{ for } x \in \mathbb{R},\\
&\nu_p(A) = \alpha \in \mathbb{N} \cup \{0\} \text{ if } p^\alpha \parallel A,\ p^{\alpha+1} \not| A.
\end{aligned}
$$

For $u \in \mathbb{Z}$, $(u, p) = 1$ we write $\overline{u}$ if $u \cdot \overline{u} \equiv 1(mod\ p^m)$.

2 Auxiliary results

We need the following simple statements.

Let $f(x)$ be a periodic function with a period τ. For any $N \in \mathbb{N}$, $1 \le N \le \tau$, we denote

$$S_N(f) := \sum_{x=1}^{N} e^{2\pi i f(x)}$$

Lemma 1. *The following estimate*

$$|S_N(f)| \le \max_{1 \le n \le \tau} \left| \sum_{x=1}^{\tau} e^{2\pi i \left(f(x) + \frac{nx}{\tau}\right)} \right| \log \tau \tag{3}$$

holds.

Let $\mathfrak{J}(A, B; p)$ be a number of solutions of the congruence $A - Bu^2 \equiv 0(mod\ p)$, $(u, p) = 1$.

Lemma 2. *Let p be a prime number and let $f(x)$, $g(x)$ be the polynomials over $\mathbb{Z}$*

$$
\begin{aligned}
f(x) &= A_1 x + A_2 x^2 + p(A_3 x^3 + \cdots),\\
g(x) &= B_1 x + p(B_2 x^2 + \cdots),
\end{aligned}
$$

and, moreover, let $\nu_p(A_2)=\alpha>0$, $\nu_p(A_j)\geq\alpha$, $j=3,4,\ldots$. *Then we have the following estimates*

$$\left|\sum_{x\in R_m} e_m(f(x))\right| \leq \begin{cases} 2p^{\frac{m+\alpha}{2}} & \text{if } \nu_p(A_1)\geq\alpha, \\ 0 & \text{else;} \end{cases} \tag{4}$$

$$\left|\sum_{x\in R_m^*} e_m(f(x)+g(\overline{x}))\right| \leq \begin{cases} (\mathfrak{I}(A_1,B_1;p)\cdot p)^{\frac{m}{2}} & if\ (B_1,p)=1, \\ 2p^{\frac{m+\alpha}{2}} & if\ \nu_p(A_1)\geq\alpha, \\ & \quad \nu_p(B_j)\geq\alpha, \\ & \quad j=1,2,\ldots, \\ 0 & if\ \nu_p(A_1)<\alpha\leq\nu_p(B_j), \\ & \quad j=1,2,3,\ldots. \end{cases} \tag{5}$$

3 Preparations

Consider the sequence $\{y_n\}$ produced by the recursion (2).
Let $n=2k$. We put

$$y_{2k}\equiv\frac{a_0^{(k)}+a_1^{(k)}y_0+\cdots}{b_0^{(k)}+b_1^{(k)}y_0+\cdots}:=\frac{A_k}{B_k}(mod\ p^m) \tag{6}$$

Twice using the recursion (2) we infer

$$\begin{aligned} y_{2(k+1)}=\frac{A_{k+1}}{B_{k+1}} &\equiv \frac{\left(aA^{(k)}+abB^{(k)}+b^2A^{(k)}\right)}{aB_k+bA_k+cA_kF(2k+1)y_0}+ \\ &+\frac{\left(acB^{(k)}+bcA^{(k)}F(2k+2)+bcA^{(k)}F(2k+1)\right)y_0}{aB_k+bA_k+cA_kF(2k+1)y_0}\equiv \\ &\equiv \frac{(aA_k+abB_k+b^2A_k)}{aB_k+bA_k+cA_kF(2k+1)y_0}+ \\ &+\frac{(acB_k+bcA_kF(2k+2)+bcA_kF(2k+1))\,y_0}{aB_k+bA_k+cA_kF(2k+1)y_0}+ \\ &+\frac{c^2A_kF(2k+1)F(2k+2)y_0^2}{aB_k+bA_k+cA_kF(2k+1)y_0} \end{aligned} \tag{7}$$

Define the following matrices

$$\begin{aligned} &S_0=\begin{pmatrix} a+b^2 & ab \\ b & a \end{pmatrix},\ S_1=\begin{pmatrix} b & a \\ 0 & 0 \end{pmatrix},\ S_2=\begin{pmatrix} 1 & 0 \\ 1 & 0 \end{pmatrix},\ S_3=\begin{pmatrix} 1 & 0 \\ 0 & 0 \end{pmatrix} \\ &T_k=S_0+cy_0F(2k+2)S_1+bcy_0F(2k+1)S_2+ \\ &\quad +c^2y_0^2F(2k+1)F(2k+2)S_3 \end{aligned} \tag{8}$$

Now from (6)-(7) we obtain the matrix equality

$$\begin{pmatrix} A_{k+1} \\ B_{k+1} \end{pmatrix}=T_kT_{k-1}\cdots T_1\begin{pmatrix} A_0 \\ B_0 \end{pmatrix},\ \begin{pmatrix} A_0 \\ B_0 \end{pmatrix}=\begin{pmatrix} y_0 \\ 1 \end{pmatrix} \tag{9}$$

Denote

$$Y_i = cy_0F(2i+2)S_1 + cby_0F(2i+1)S_2 + c^2y_0^2F(2i+1)F(2i+2)S_3$$

Then we have

$$T_1T_2\cdots T_k = S_0^k + \sum_{\ell=1}^{k-1} S_0^{k-\ell} \sum_{j=0}^{k} {\sum_{i_1,\ldots,i_\ell}}' Y_{i_1}\cdots Y_{i_\ell}, \tag{10}$$

where the sum ${\sum_{i_1,\ldots,i_\ell}}'$ takes over all collections $i_1,\ldots,i_\ell$ for which $0 \le i_1,\ldots,i_\ell \le k$, $i_t \ne i_s$ for $t \ne s$, and $i_t \ne j$, $t = 1,\ldots,\ell$, $s = 1,\ldots,\ell$.

We will suppose that $\nu = \nu_p(b) < \nu_p(c) = \mu$. Therefore $Y_i \equiv 0 (mod\ p^\mu)$, and hence, all summands of sum ${\sum_{i_1,\ldots,i_\ell}}'$ are equal to zero modulo p^m if $\ell > k_0 := \left[\frac{m+1}{\mu}\right]$.

First we study S_0^k in detail.

We have

$$S_0 = aI + bZ,$$

where

$$I = \begin{pmatrix} 1 & 0 \\ 0 & 1 \end{pmatrix}, \ \ Z = \begin{pmatrix} b & a \\ 1 & 0 \end{pmatrix}.$$

Hence, putting $\ell_0 = \min\left(\left[\frac{k+1}{2\nu}\right], \left[\frac{m+1}{2\nu}\right]\right)$ we can write

$$S_0^k = \sum_{j=0}^{k} \binom{k}{j} a^{k-j}b^jZ^j = \sum_{\substack{j=0 \\ \text{j is even}}}^{\ell_0} + \sum_{\substack{j=0 \\ \text{j is odd}}}^{\ell_0} := \sum\nolimits_1 + \sum\nolimits_2, \tag{11}$$

where modulo p^m

$$\begin{aligned} \sum\nolimits_1 &= \sum_{j=0}^{\ell_0} \binom{k}{2j} a^{k-2j}b^{2j}Z^{2j}, \\ \sum\nolimits_2 &= \sum_{j=0}^{\ell_0} \binom{k}{2j+1} a^{k-2j-1}b^{2j+1}Z^{2j+1}. \end{aligned} \tag{12}$$

Notice that

$$Z^2 = \begin{pmatrix} b & a \\ 1 & 0 \end{pmatrix}^2 = \begin{pmatrix} a+b^2 & ab \\ b & a \end{pmatrix} = aI + bZ.$$

Consequently, raising to square in series the matrix Z we derive for $j \le \ell_0$

$$Z^{2j} = F_0(j)I + F_1(j)Z \tag{13}$$

where

$$\begin{cases} F_0(j) = f_{0,j} + b^2 f_{2,j} + \cdots + b^{2j-2} f_{2j-2,j}, \\ F_1 = b f_{1,j} + b^3 f_{3,j} + \cdots + b^{2j-1} f_{2j-1,j}, \\ f_{0,j} = a^j, \;\; f_{1,j} = a^{j-1} j. \end{cases} \tag{14}$$

Moreover, it is easy to see that

$$\begin{cases} f_{2,j} = a^{j-1}(2j-3), \;\; f_{3,j} = \overline{2} a^{j-1}(3j^2 - 9j + 8), \\ f_{2j-4,j} = a^2(2j-3), \;\; f_{2j-2,j} = a, \\ f_{2j-3,j} = a(f_{2j-3,j-1} + 2j - 3), \;\; f_{2j-1,j} = 1, \\ f_{2\ell,j} = a^{j-\ell}(f_{2\ell,j-1} + f_{2\ell-1,j-1}), \\ f_{2\ell+1,j} = a^{j-\ell}(f_{2\ell,j-1} + f_{2\ell+1,j-1} + f_{2\ell-1,j-1}), \\ \ell = 2, 3, \ldots, j-2. \end{cases} \tag{15}$$

So, for $k \geq m$ the coefficients $f_{\ell,j}$ does not depend on k.
From (13)-(14) we derive

$$\begin{aligned} Z^{2j+1} &= (j a^j b + f_{3,j} a^{j-1} b^3 + \cdots + a b^{2j-1}) I + \\ &+ (a^j + a^{j-1} b^2 (f_{2,j} + j) + \cdots + a b^{2j-2}(2j-1) + b^{2j}) Z = \\ &= G_0(j) I + G_1(j) Z. \end{aligned} \tag{16}$$

Thereby the relations (13)-(16) give

$$\begin{aligned} S_0^k = &\sum_{j=0}^{\ell_0} a^{k-2j-1} b^{2j} \left(\binom{k}{2j} a F_0(j) + \binom{k}{2j+1} b G_0(j) \right) I + \\ &+ \sum_{j=0}^{\ell_0} a^{k-2j-1} b^{2j} \left(\binom{k}{2j} a F_1(j) + \binom{k}{2j+1} b G_1(j) \right) Z. \end{aligned} \tag{17}$$

Now after the simple calculations we obtain

$$S_0^k = H_0(k) I + H_1(k) Z, \tag{18}$$

where modulo p^m

$$\begin{cases} H_0(k) = a^k + k a^{k-1} b (1 + b^2 h_{01}) + k^2 a^{k-2} b^2 (\overline{2} + b^2 h_{02}) + \\ \qquad + k^3 a^{k-2} b^3 H_{03}(k), \\ H_1(k) = a^{k-1} b k (1 + b^2 h_{11}) + k^3 b^3 H_{13}(k), \\ H_{03}(k), H_{13}(k) \in \mathbb{Z}[k], \;\; h_{01}, h_{02}, h_{11} \in \mathbb{Z}. \end{cases} \tag{19}$$

Repeating the argument used in the proof of relations (18),(19) we easy deduce that

$$\sum_{\ell=1}^{k_0} S_0^{k-\ell} \sum_{j=0}^{k} {\sum_{i_1,\ldots,i_\ell}}' Y_{i_1} \cdots Y_{i_\ell} = \overline{H}_0(k) I + \overline{H}_1(k) Z, \tag{20}$$

where

$$\begin{cases} \overline{H}_0(k) = kca^k \left[(\overline{f}_{0,0} + \overline{H}_{01}b) + kb^2\overline{H}_{02}(k) \right], \\ \overline{H}_1(k) = kbca^k\overline{H}_{1,0}(k), \end{cases} \tag{21}$$

$\overline{H}_{01}(k), \overline{H}_{02}(k), \overline{H}_{10}(k)$ are the integer polynomials with coefficients depending only on $\overline{a}, (\overline{a})^2, \dots, (\overline{a})^m,\ b_0, b_0^2, \dots, b_0^{\left[\frac{m+1}{\nu}\right]},\ c_0, c_0^2, \dots, c_0^{\left[\frac{m+1}{\mu}\right]},\ b_0 = \frac{b}{p^\nu}$, $c_0 = \frac{c}{p^\mu}$.

After all this preliminaries it is straightforward to establish two representations for y_n:

Lemma 3. *Let p be a prime number, $p \geq 5$, and let $m \in \mathbb{N}$, $m \geq 3$; $a, b, c \in \mathbb{Z}$, $GCD(a, p) = 1$, $b \equiv c \equiv 0 (mod\ p)$, $\nu = \nu_p(b)$, $\mu = \nu_p(c)$, $\nu < \mu$, also, let $\{y_k\}$ is the sequence from (2). Then for any $y_0 \in R_m^*$ and $k = 0, 1, 2, \dots$ we have*

$$\begin{aligned} y_{2k} &= (kb - 2^{-1}k(k^2-1)a^{-1}b^3 + G_0(k)) + \\ &+ (1 + k(k+1)a^{-1}c + G_1(k))y_0 + \\ &+ (-ka^{-1}b - (k^3c + k^2(k+1)a^{-1})bc + \\ &+ (2^{-1}3k^3 - 2k^2 + 2^{-1}k)a^{-2}b^3 + G_2(k))y_0^2 + \\ &+ (k^2a^{-2}b^2 - k^2a^{-1}c + G_3(k))y_0^3 + G_4(k, y_0)y_0^4; \\ y_{2k+1} &= ((k+1)b - k^2a^{-1}c + k(k-1)a^{-1}b^3 + H_0(k)) + \\ &+ ((2k+)c + H_1(k))y_0 + (a - k^2c - 2k^2b^2 + H_{-1}(k))y_0^{-1} + \\ &+ (-kab + 2^{-1}3k^2(k+1)b^3 + 4^{-1}k^2(k^2-1)a^{-1}b^3 + \\ &+ H_{-2}(k))y_0^{-2} + y_0^{-3}H_3(k, y_0^{-1}), \end{aligned}$$

where

$G_i(k) \in \mathbb{Z}[k],\ G_i(0) = 0,\ G_i(k) \equiv 0 (mod\ p^{\min(2\nu+\mu, 4\nu)}),\ i = 0, 1, 2, 3;$
$H_i(k) \in \mathbb{Z}[k],\ H_i(0) = 0,\ H_i(k) \equiv 0 (mod\ p^{\min(2\nu+\mu, 4\nu)}),\ i = -2, \pm 1, 0;$
$G_4(k, u),\ H_3(k, u),$ *are the polynomials on* $k, u,$

moreover,

$$G_4(0, u) = H_3(0, u) = 0,\ G_4(k, u) \equiv H_3(k, u) (mod\ p^{\min(2\nu+\mu, 4\nu)}).$$

Lemma 4. *For $k = 0, 1, 2, \dots$ we have*

$$\begin{aligned} y_{2k} &= y_0 + k(b(1 - a^{-1}y_0^2) + 2a^{-1}b^3(a + y_0^2) + a^{-1}cy_0 + C_1(y_0)) + \\ &+ k^2(-a^{-1}b^2y_0 + a^{-1}cy_0(1 - y_0^2) + C_2(y_0)) + k^3C_3(k, y_0) \end{aligned}$$

$$\begin{aligned} y_{2k+1} &= (b + cy_0 + ay_0^{-1}) + k(b(1 - ay_0^{-2}) + 2cy_0 + D_1(y_0, y_0^{-1})) + \\ &+ k^2(c(a^{-1} - y_0^{-1}) + D_2(y_0, y_0^{-1})) + k^3D_3(k, y_0, y_0^{-1}) \end{aligned}$$

where $C_1(y_0) \equiv C_2(y_0) \equiv C_3(k, y_0) \equiv 0 (mod\ p^{\min(\nu+\mu, 3\nu)})$,
$D_1(y_0, y_0^{-1}) \equiv D_2(y_0, y_0^{-1}) \equiv D_3(k, y_0, y_0^{-1}) \equiv 0 (mod\ p^{\min(\nu+\mu, 3\nu)})$
for every $y_0, y_0^{-1} \in R_m^*,\ k \in \mathbb{Z}$.

Corollary 1. *Let τ be a period length of the sequence $\{y_n\}$ generated by recursion (2), y_0 be an initial value, and let $\nu_p(b) = \nu$, $\nu_p(c) = \mu > \nu$.*

(A) If $a \not\equiv {y_0}^2 (mod\ p)$, then $\tau = 2p^{m-\nu}$.
(B) If $\nu_p(a - y_0^2) = \delta < \min(3\nu, \mu)$, then $\tau = 2p^{m-\nu-\delta}$.
(C) Otherwise: $\tau \le 2p^{m-\nu-\min(3\nu,\mu)}$.

4 Main results

Let the sequence $\{y_n\}$ is produced by recursion (2) and let the least length of period for $\{y_n\}$ is equal to τ.

For any N, $1 \le N \le \tau$, and $h \in \mathbb{Z}$ we define the sum

$$S_N(h, y_0) = \sum_{n=0}^{N-1} e_m(hy_n)$$

Theorem 1. *Let $\{y_n\}$ is the sequence generated by the recursion (2) with the parameters a, b, c and the function $F(n)$, $F(0) = 0$, and let $0 \le \nu_p(a - y_0^2) < \nu = \nu_p(b)$, $2\nu < \mu = \nu_p(c)$, $\nu_p(h) = s$. Then we have*

$$|S_N(h, y_0)| \le \begin{cases} 2p^{\frac{m+\nu+s}{2}} \left(\frac{N}{\tau} + \frac{\log \tau}{p}\right) & if \quad \nu + s < m \\ N & else. \end{cases}$$

Theorem 2. *In the notations of Theorem 1 we have*

$$\overline{S}_N(h) = \frac{1}{\varphi(p^m)} \sum_{y_0 \in R_m^*} |S_N(h, y_0)| \le 3Np^{-\frac{m-s-\nu}{4}}$$

The proofs of these theorems are an analogue of the proofs for Theorem 7 and 8[5] and by the representations of y_n which have been obtained in Lemmas 3 and 4, and using Lemmas 1 and 2.

Now applying the Turan-Koksma inequality(see,[3]) for the discrepancy D_N we obtain

Theorem 3. *Let $p > 2$ be a prime number, $y_0, a, b, c, m \in \mathbb{Z}$, $m \ge 3$ and let a, y_0 are co-primes to p and let $b \equiv c \equiv 0 (mod\ p)$, $0 < \nu_p(b) < \nu_p(c)$, $a \not\equiv y_0^2 (mod\ p)$. Then for the sequence $\{x_k\}$, $x_k = \frac{y_k}{p^m}$, $k = 0, 1, \ldots$, where y_k determine by (2) we have*

$$D_N(x_0, x_1, \ldots, x_{N-1}) \le \frac{1}{p^m} + 2N^{-1}p^{\frac{m-\nu}{2}} \left(\frac{1}{p}\left(\frac{2}{\pi}\log p^m + \frac{7}{5}\right)^2 + 1\right),$$

where $1 \le N \le \tau$, and τ is the least length of a period for $\{y_k\}$.

Next, we denote

$$X_n^{(s)} = (x_n, x_{n+1}, \ldots, x_{n+s-1}),\ s = 2, 3, 4.$$

Theorem 4. *The discrepancy* $D_N^{(s)}(X_0^{(s)}, X_1^{(s)}, \ldots, X_{N-1}^{(s)})$ *produced by the recursion (2) with the period* $\tau = 2p^{m-\nu}$ *satisfies the inequality*

$$D_\tau^{(s)} \leq \frac{\sqrt{p}}{\sqrt{p}-1} p^{-\frac{m}{2}+\nu} \left(\frac{1}{\pi} \log p^{m-\nu} + \frac{3}{5} \right)^s + 2p^{-m+\nu}.$$

From the Theorems 3 and 4 it follows that the sequence $\{x_n\}$, $x - n = \frac{y_n}{p^m}$ passes the s-serial tests, $s = 2, 3, 4$ on equidistribution and statistical independence.

Thus, by the complexity of reconstruction for the parameters a, b, c, y_0, $F(u)$ under recursion (2) the sequence of PRN's $\{y_n\}$ can be used in cryptographical applications.

References

1. S.R. Blackburn, D. Gomez-Peres, I. Gutierrez and I. Shparlinski. Predicting nonlinear pseudorandom number generators. *Math. Comp.*, 74(251):1471–1494, 2004.
2. S.R. Blackburn, D. Gomez-Peres, I. Gutierrez and I. Shparlinski. Reconstructing noisy polynomial evaluation in residue rings. *J. of Algorithm*, 61(2):47–59, 2006.
3. H. Niederreiter. Random number generation and Quasi-Monte Carlo methods. *SIAM, Philadelphia*, 1992.
4. H. Niederreiter and I. Shparlinski. Recent advances in the theory of nonlinear pseudorandom number generators. *Proc. Conf. on Monte Carlo and Quasi-Monte Carlo Methods, 2000, Springer-Verlag, Berlin*, 86–102, 2002.
5. P. Varbanets, S. Varbanets. Exponential sums over the sequences of inversive congruential pseudorandom numbers with prime-power modulus. *VoronoÏ's impact on modern science*, Book 4(1):112–130, 2008.

Proceedings, 5th Chaotic Modeling and Simulation International Conference, 12 – 15 June 2012, Athens Greece

A Repeating Relation for Electron Velocities in Argon Plasma. An attempt to extend the Perturbation Theory.

C. L. Xaplanteris[1,2], E. D. Filippaki[1], I. S. Mistakidis[2] and L. C. Xaplanteris[3]

(1) Plasma Physics Laboratory, IMS, NCSR "Demokritos", Athens , Greece

(2) Hellenic Military Academy , Vari Attica , Greece .

(3) School of Physics, National and Kapodistrian University of Athens , Greece .

e-mail: cxaplanteris@yahoo.com

Abstract: It is a commonplace fact that the mathematical representation of the chaos theory on the whole is very difficult to be given. This means that there is not any mathematical equation capable of describing and solving a nonlinear and chaotic problem. So, as every case is unique, our work has to contribute to the chaotic topic both mathematically and experimentally. Magnetized argon plasma is produced into a metallic cylinder. A coaxial antenna is used for the r-f energy importation and the plasma maintenance consequently. This device has a complete cylindrical symmetry and the mathematic elaboration in the cylindrical system is carried out. An attempt to show a repeating relation for ion velocities of magnitude of every order is presented as our new work. In addition, it is well known that the perturbation theory can be used to extend the linear theory of plasma waves into the nonlinear regime and, thus, give an explanation of many nonlinear phenomena. This nonlinear perturbation theory of small amplitude plasma waves and their interactions is well developed; on the contrary, the perturbation theory of large-amplitude plasma waves is still being developed. In the present paper, a generalization of the perturbation theory is attempted with the division of the perturbed magnitude and the use of the repeating estimation.

1. Introduction

In the early 60's many plasma instabilities have been observed taking wavy forms into the plasma [1,2]. These waves absorb the plasma energy, then the plasma temperature is consequently reduced and the removal of the thermonuclear fusion conditions is resulted. So, the wavy instabilities are considered to be a serious obstacle to the nuclear fusion process and their study has been carried out constantly and in detail during the last decades [3-5]. Many special books constitute the Plasma Physics Literacy [6-8], list and study all the waves from the low frequency region [1- 5] to the high frequency one [9]. In the Plasma Laboratory of the Center "Demokritos" an adequate amount of experience has been gained, especially on the low frequency electrostatic waves [10-12] and their effect on the plasma conductivity [11]. The chaotic behavior of the plasma waves has been studied as well [13-14]. It is well known that the plasma can easily pass from a steady state into a chaotic one, which was repeatedly published in our previous papers [15, 16]. In the present work an attempt takes place to compare the experimental data with the computation results, and so, our theory may be confirmed. A mathematic relation, which connects the different order velocities, was found and may be used as a repeating relation showing the chaotic behavior of the plasma. The relation is valid under the condition that the perturbed qualities are small in comparison with the unperturbed one [6-8]. In the present work a calculative trial using the relation as a repeating one may bring it into the function conditions and the perturbed theory can be therefore extended. Although the experimental results are in a satisfactory agreement with the calculation, the subject remains open as a chaotic state and requires further study.

The paper is organized as following: The experimental devices are briefly described in Sec.2, since the experimental results are presented in the following Sec.3. In Sec. 4 a full mathematical elaboration and the computational results are curried out. The confirmation between theory and experiment and conclusions are included in Sec. 5. The appendix in the end provides a more detailed mathematical elaboration.

2. Experimental Arrangement

As our experience on the magnetized argon plasma is concentrated on full cylindrical symmetry, the same

geometry is used at the present study as well, since the low frequencies of plasma waves are persistent [1-3, 10-12]. A cylindrical cavity made of steady steel is located with its' axis along the external magnetic field B . The cavity is $60cm$ long with $6cm$ internal diameter and, in the center of the first disk-like base, the $25cm$ rf power antenna is mounted; in the other disk-like base a $25cm$ external driving wave antenna is mounted as well, which enables us to affect and control the plasma waves. Electrostatic Langmuir probes were fixed to move radially, azimouthally and axially with the ability to detect the plasma waves that appear and measure their physical quantities (wave frequency, wave amplitude, plasma temperature, plasma density, plasma potential e.t.c.). Furthermore, a disk-probe was fixed to move radially and around its' axis, which allows, apart from the above quantities, the measuring of the azimouthal electron drift current. In Fig.1 (a) the plasma column cut is shown, whereas an extensive drawing of the cavity's position into the magnetic field is presented in Fig.1 (b).

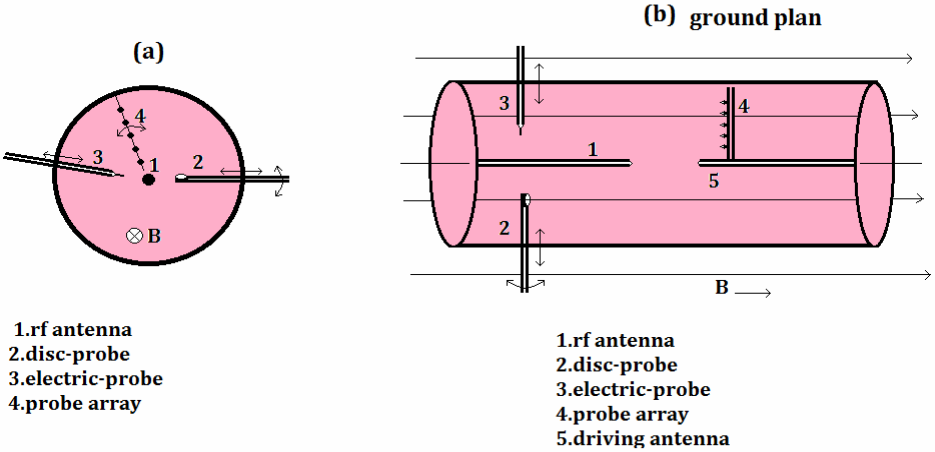

Fig.1 (a), the plasma column is shown. Fig.1 (b), the cavity's placing into the magnetic field is presented (ground plan).

The argon entrance, its outlet to the pump and a suitable window are visible at the Fig.1 (b) as well.

3. Experimental Results

The existence of the electrical waves into the argon plasma is confirmed once more. These low frequency waves are divided into three frequency regions with a quasi-same behavior in many instances. An extensive study of these waves was carried out at the Plasma Laboratory of NCSR ''Demokritos'' previously, and two of them were absolutely identified [10, 12]. Figure 2 gives a middle frequency region wave indicatively with its' spectrum of frequencies where the upper harmonics appear.

The plasma is lit into an wide space of the external plasma parameters (gas pressure p , magnetic field B and rf field absorbed power P) and results in a wide region of plasma quantities as well; these quantities include the plasma temperature T , the plasma density n , the plasma potential Φ , and all the wave parameters. Table 1 shows some typical values of the plasma parameters.

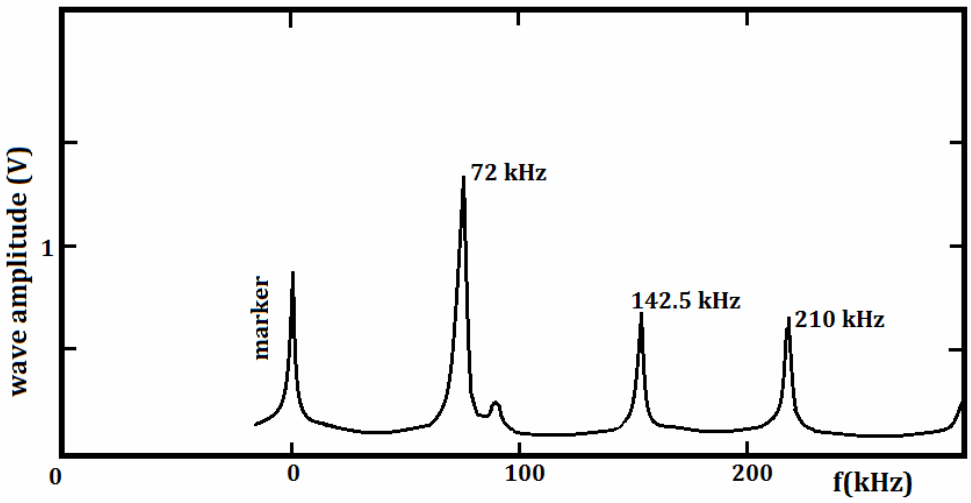

Fig. 2, a typical wave spectrum in the middle frequency region.

Table 1 The plasma parameters ranging values

Parameters	Minimum value	Maximum value
Argon pressure p	$0.001\,Pa$	$0.1Pa$
Argon number density, n_g	$2\times10^{15}\,m^{-3}$	$2\times10^{17}\,m^{-3}$
Magnetic field intensity, B	$10\,mT$	$200\,mT$
Microwaves' power, P	$20Watt$	$120Watt$
Frequency of the rf power (standard value)	$2.45GHz$	
Electron density, n_0	$2\times10^{15}\,m^{-3}$	$4.6\times10^{15}\,m^{-3}$
Electron temperature, T_e	$1.5eV$	$10eV$
Ion temperature, T_i	$0.025\,eV$	$0.048\,eV$
Ionization rate	0.1%	90%
Electron drift velocity, u_e	$1\times10^{4}\,m/s$	$1.7\times10^{4}\,m/s$
Electron-neutral collision frequency, ν_e	$1.2\times10^{7}\,s^{-1}$	$3\times10^{9}\,s^{-1}$

The experimental part of the present paper consists of the following steps:

i) By using the radially moving probe, the plasma potential $\Phi(r)$ is measured along the cylinder radius and then, from the relation $\varepsilon=-\frac{\Delta\Phi}{\Delta r}$ the plasma electric field ε is calculated. Figures 3 (a), (b) show the radial potential and radial electric field respectively.

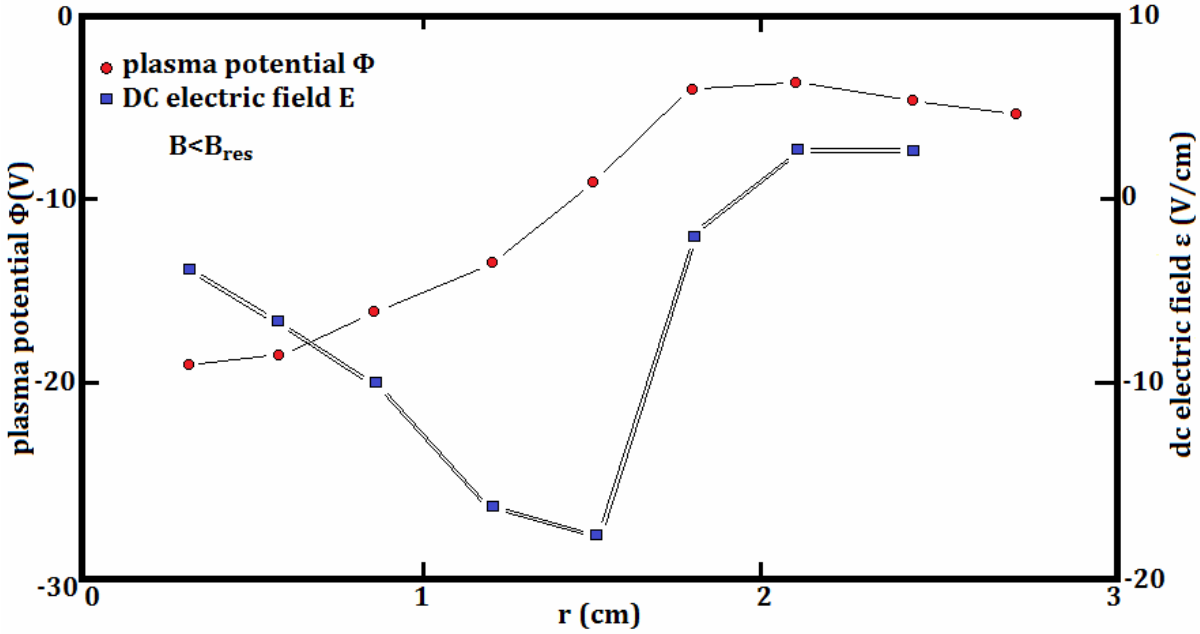

Figs.3 (a), (b) show the plasma potential $\Phi(r)$ and the electric field ε along the cylinder radius respectively.

It must be noted that the electric field ε remains nearly constant in the middle of the radius, where the wave rises and its' amplitude constantly increases [5, 10-12]. The measurement has been done by $B \prec B_0$.

ii) The perturbed electric field E must be measured, consequently. This measurement may be a result of the wave amplitude as it appears along the cylinder radius. Figures 4 (a), (b) show the wave amplitude (in Volts) and the perturbed field E correspondingly. The measurement was repeated for values of the magnetic field B , under and above the upper cyclotron resonance B_{res} .

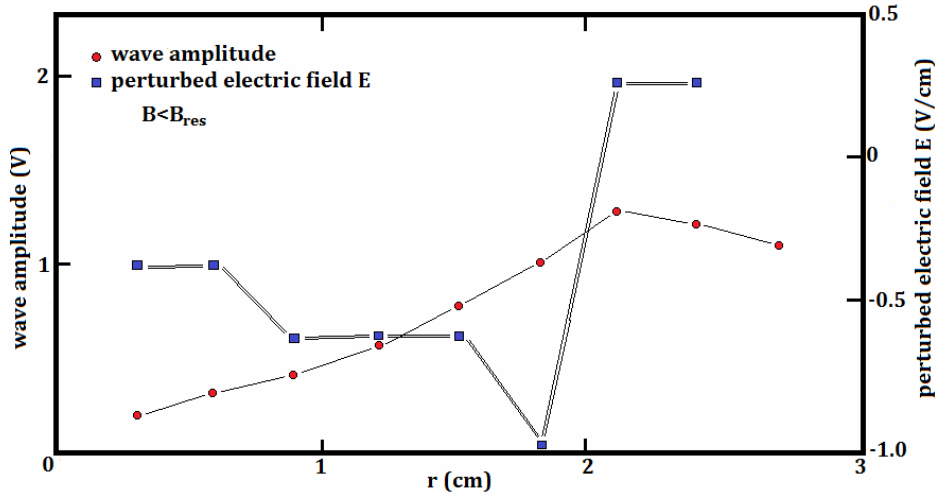

Figs.4 (a), (b) show the wave amplitude and the perturbed electric field E along the cylinder radius correspondingly (respectively).

iii) The measurement of the azimouthal electron drift velocity u_e is the next step. This is obtained by using the disk probe as it moves around its' axis. Figure 5 indicates the method of the measurement of the azimouthal

electron current I_θ, which requires two simple movements: the orientation of the probe surface perpendicularly to the electron drift course, and after, in the opposite direction of the electrons' motion.

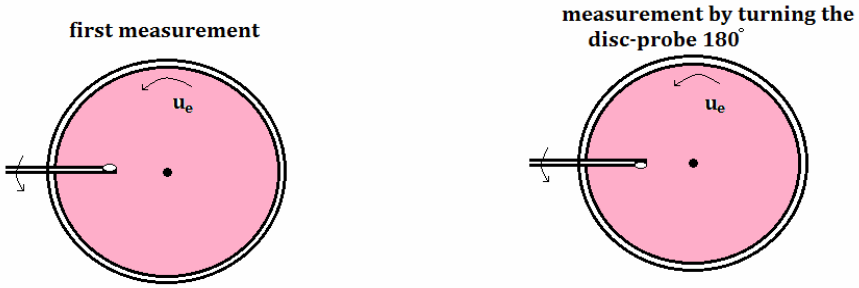

Fig. 5, the electron drift current measurement

The next relations $I_1 = I_\theta + I_{th}$ and $I_2 = -I_\theta + I_{th}$ are valid and result in the relation below,

$$I_\theta = \frac{I_1 - I_2}{2}$$

Taking into consideration that the relation $I_\theta = e.n_e.u_e.\mathrm{A}$ is valid (with A the probe surface area), the azimouthal electron drift can be found. Measurements and estimations are listed in Table 2, since the electron drift velocity u_e and the perturbed velocity υ are presented in Fig. 6, as well.

Table 2 The azimouthal electron drift current and the drift velocity along a cylinder radius

Radius r (cm)	drift current I_e (μA)	plasma density n_e ($x\mathbf{10^{15}}\, m^{-3}$)	drift velocity u_e ($x10^3\, m/s$)	E/ε	perturbed velocity υ_θ (m/s)
0.3	20	6.0	4.43	–0.1	–443
0.6	26	6.2	5.57	–0.05	–278
0.9	30	6.5	6.17	–0.067	–413
1.2	37	7.0	7.02	0.04	281
1.5	42	6.8	8.20	0.037	303
1.8	46	6.2	9.85	0.25	2462
2.1	35	5.9	7.92	0.1	792
2.4	25	5.6	5.93	0.1	593
2.7	16	5.5	3.86		

iv) The perturbed velocity υ_θ is impossible to be found directly by an experimental measuring, but it can be estimated from the relation $\upsilon_\theta = \frac{E}{\varepsilon} u_\theta$, as the quantities ε, E and u_θ have been measured/determined above. The results for the υ are given again in Table 2.

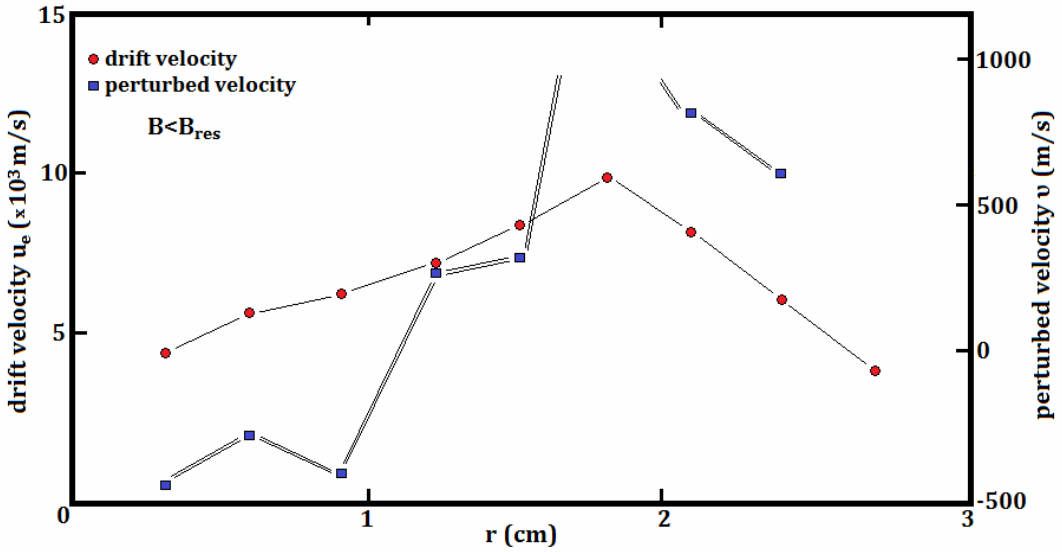

Fig. 6. The drift velocity u_e and the perturbed velocity υ are presented

4. Mathematical Elaboration-Computational Results

Perturbed velocities' study

In the Appendix it is proved that the drift and perturbed velocities are related to the electrical fields with the Eq. (A. 9),

$$\upsilon_r = \frac{E}{\varepsilon} u_r \quad \text{and} \quad \upsilon_\theta = \frac{E}{\varepsilon} u_\theta \qquad \text{(A. 9)}$$

A. When the perturbed electric field E is very small, then the relations $\upsilon_r \prec u_r$ and $\upsilon_\theta \prec u_\theta$ are valid.

B. If the relation $\upsilon \approx u$ is valid, the electric fields must have the same behavior as $E \approx \varepsilon$. This means that the wave amplitude undergoes some big changes along the cylinder radius.

With the replacement of the quantity Π , the Eqs (A. 7) are written:

$$\upsilon_\theta = \frac{E}{B} \cdot \frac{\omega_c^2}{\omega_c^2 + \left[j(ku-\omega) + \nu \right]^2} \qquad \text{and} \qquad \upsilon_r == \frac{E}{B} \cdot \frac{\omega_c \left[j(ku-\nu) + \nu \right]}{\omega_c^2 + \left[j(ku-\omega) + \nu \right]^2} \qquad (1)$$

The azimouthal perturbed velocity υ_θ is of the most interest: by taking $\Pi^2 = \nu^2 - (ku-\omega)^2 + j2\nu(ku-\omega)$ and limiting the real part only, the first of Eqs (1) is rewritten as following,

$$\upsilon = \frac{E}{B} \cdot \frac{\omega_c^2}{\omega_c^2 + \nu^2 - (ku-\omega)^2} \qquad (2)$$

with $\upsilon_\theta = \upsilon$ for simplicity; this may be used as the repeating relation.

It must be reminded that the Eq.(A. 9) was produced with the presupposition that the relation $\upsilon \prec\prec u$ is valid. This consists a necessary condition for the linearization of Eq. (A. 1) (perturbation theory).

Now, if we seek a solution for $\upsilon \approx u$, approximately, by separating the perturbed velocity υ into small parts $\upsilon_1, \upsilon_2, \upsilon_3, ...\upsilon_i$ with $i = 10,100,1000,....$ and every part $\upsilon_i \prec\prec \upsilon$, the perturbation theory condition is satisfied.

Taking $u = u_0$ and $\upsilon = \upsilon_1 \prec \frac{\upsilon}{10}$, the Eq. (2) is written,

$$\upsilon_1 = \frac{E}{B}.\frac{\omega_c^2}{\omega_c^2 + \nu^2 - (ku_0 - \omega)^2} \qquad (3)$$

With the addition $u_1 = u_0 + \upsilon_1$, the above equation gives the term υ_2,

$$\upsilon_2 = \frac{E}{B}.\frac{\omega_c^2}{\omega_c^2 + \nu^2 - (ku_1 - \omega)^2}$$

If it is taken $u_2 = u_1 + \upsilon_2$, the Eq. (2) gives the term υ_3,

And so on, with $u_{i+1} = u_i + \upsilon_{i+1}$ the repeating relation,

$$\upsilon_{i+1} = \frac{E}{B}.\frac{\omega_c^2}{\omega_c^2 + \nu^2 - (ku_i - \omega)^2} \qquad (4)$$

is obtained.

Repeating equation study

It is evident that the minimum value of the term $(ku_i - \omega)^2$ is zero, and then the denominator in the Eq. (4) takes the maximum value. Then, we conclude that, at the value $u_i = \frac{\omega}{k}$, the υ_{i+1} has the minimum value, $\upsilon_{i+1} = \frac{E}{B}\frac{\omega_c^2}{\omega_c^2 + \nu^2}$, which is the same as if the quality $\Pi = j(ku - \omega) + \nu \cong \nu$, is taken.

Another significant result is obtained if the relations $u_1 = u_0 + \upsilon_1$, $u_2 = u_1 + \upsilon_2$, $u_3 = u_2 + \upsilon_3$, ... $u_i = u_{i-1} + \upsilon_i$, are added by parts, when the relation $u_i = u_0 + \upsilon_1 + \upsilon_2 + \upsilon_3 + ... + \upsilon_i$ or

$$u_i = u_0 + \upsilon \quad (5) \text{ is obtained}$$

with $\upsilon = \upsilon_1 + \upsilon_2 + \upsilon_3 + ... + \upsilon_i$ the whole-total large perturbed velocity.

The relation $u_i = u_0 + \upsilon$ must be confirmed experimentally.

Computational results

The experiment leads to the following calculations;

$$\frac{E}{B} \cong \frac{100V.m^{-1}}{70.mT} \quad \Rightarrow \frac{E}{B} \cong 1430\frac{m}{s}.$$

$$\omega_c^2 = \left(\frac{e.B}{m_e}\right)^2 = \left(\frac{1{,}6.10^{-19}.7.10^{-2}}{9{,}1.10^{-31}}\right)^2 \quad , \qquad \underline{\Rightarrow \omega_c^2 \cong 1{,}5.10^{20}\, s^{-2}}$$

$\underline{\nu^2 \cong 10^{19}\, s^{-2}}$

When it is taken $ku_0 - \omega = 0$, then $u_0 = \omega/k = \omega.R/l \Rightarrow u_0 = \omega.R/l$.

Taking $\omega = 2\pi.f = 2\pi.7.10^4\, s^{-1} \Rightarrow \omega = 1{,}4.\pi.10^5\, s^{-1}$, $l = 1$ and $R = 2.10^{-2}\, m$ then

$u_0 = 1{,}4.\pi.10^5.2.10^{-2}\ m/s \qquad \underline{\Rightarrow u_0 \cong 0{,}88.10^4\ m/s}$

In the above case the perturbed velocity υ_1 is minimized at the value, (see eq. 3) ,

$$\upsilon_1 = 1430.\frac{10^{20}}{10^{20}+10^{19}}\ m/s \qquad \underline{\Rightarrow \upsilon_1 \cong 1300\ m/s}$$

On the other hand, the relation $\upsilon = E/\varepsilon u$ gives,

$$\upsilon = \frac{2V.cm^{-1}}{20V.cm^{-1}}.u \qquad \underline{\Rightarrow \upsilon = 880\ m/s}$$

Now, with $u_1 = u_0 + \upsilon_1 = (8800 + 880)\ m/s \Rightarrow u_1 = 9680\ m/s$, the perturbed υ_2 from the repeating equation below can be calculated,

$$\upsilon_2 = \frac{E}{B}.\frac{\omega_c^2}{\omega_c^2 + \nu^2 - (ku_1 - \omega)^2}$$

or
$$\upsilon_2 = 1430.\frac{1{,}5.10^{10}}{16.10^9 - (5.0{,}968 - 4{,}4)^2}$$

or
$$\upsilon_2 = 1340{,}624999983778437500 19$$

Now it is taken, $u_2 = u_1 + \upsilon_2$, $\Rightarrow u_2 = 9680 + 1340{,}624999983778437500 19$

$\Rightarrow u_2 = 11020{,}624999983778437500 19$, and so on.

5. Explanations- Conclusions

The existence of the low frequency waves into the argon magnetized plasma was observed in our early experiments at the Plasma Laboratory of Demokritos. A satisfactory explanation about it was given as well [10,12]. In previous publication the possibility for development of the low frequency waves has been presented. Two kinds of these waves has been identified already [10, 12]. The cylindrical symmetry of the plasma column gives them an azimouthal propagation, whereas the boundaries cause for standing waves formation. By using the perturbation theory on the two fluids model, the relation,

$$\upsilon = \frac{E}{B}.\frac{\omega_c^2}{\omega_c^2 + \nu^2 - (ku-\omega)^2}$$

is obtained under the conditions $\upsilon \prec\prec u$.

The validity of the above equation is attempted to be proved with the present experiment. So, the value of the perturbed velocity υ was found at first experimentally and then by estimation from the above equation. The direct measurement of the perturbed velocity υ is impossible to be carried out as it is added on the drift velocity u, resulting in the inability to be distinguished from it. For this reason, the relation $\upsilon = {}^{E}\!/_{\varepsilon}.u$ was used, which requires the measurement of the quantities E, ε and u. As Figs 3 and 4 show, the electric fields E and ε are maximized in the middle of the radius, where the wave is developed, and the ratio ${}^{E}\!/_{\varepsilon}$ is very close to the perturbation theory condition. Furthermore, from Table 2 the values of the drift electron velocity are taken. Figure 6 gives the measured values of the perturbed velocity υ. Afterwards, the calculated values from the repeating equation are taken. Despite the inevitable inclinations of the measurements, the two results are satisfactory close, and may have the certainty that the suggested calculation method is right. Another significant observation is that, because of the use of the equation as a repeating one, the values of the perturbed velocity are slightly affected from the drift velocity enlargement. On the contrary, the drift velocity enlargement strengthens the function condition $\upsilon \prec\prec u$.

Appendix

The momentum equation on the two fluids theory based on a non-local slab is written as,

$$N_\alpha m_\alpha \left[\frac{\partial}{\partial t} + \vec{V}_\alpha.\vec{\nabla}) \right]\vec{V}_\alpha = N_\alpha q_\alpha (\vec{\varepsilon} + \vec{E}) + N_\alpha q_\alpha \frac{\vec{V}_\alpha x\vec{B}}{c} - N_\alpha m_\alpha \nu \vec{V}_\alpha - \vec{\nabla} p$$

where the indicator α is given for both kinds of the charged particles, electrons and ions. In the following elaboration, the α is omitted for simplicity and the momentum equation for either electrons and ions becomes,

$$N\ m\ \left[\ \frac{\partial}{\partial t} + \vec{V}.\vec{\nabla})\ \right]\vec{V} = Nq(\vec{\varepsilon} + \vec{E}) + Nq\frac{\vec{V}x\vec{B}}{c} - Nm\ \nu\vec{V} - \vec{\nabla} p \qquad \text{(A.1)}$$

where $N = n_0 + n(\vec{r},t), \vec{E}_{tot} = \vec{\varepsilon} + \vec{E}(\vec{r},t)$, and $\vec{V} = \vec{u}_0 + \vec{\upsilon}(\vec{r},t)$,

and $n(\vec{r},t), \vec{E}(\vec{r},t)$, and $\vec{\upsilon}(\vec{r},t)$, the perturbed qualities with harmonic influence $\propto e^{j(\vec{k}\vec{r}-\omega t)}$.

When no perturbation exists, the drift velocity u_0, is obtained;

$$0 = n_0 q\vec{\varepsilon} + n_0 q\frac{\vec{u}_0 x\vec{B}}{c} - n_0 m\nu\vec{u}_0 \qquad \text{(A. 2)}$$

With the separation on the $\vec{r}$ and θ axis the drift components are given,

$$u_\theta = \frac{q\varepsilon}{m}.\frac{\omega_c}{\omega_c^2 + \nu^2} \qquad \text{and} \qquad u_r = \frac{q\varepsilon}{m}.\frac{\nu}{\omega_c^2 + \nu^2} \qquad \text{(A. 3)}$$

(drift velocities are represented by the 0-order equation).

i) If the perturbation is taken into account, eq.(A. 1) gives,

α) $$n_0 \frac{\partial}{\partial t} + n_0\vec{u}_0\vec{\nabla}\vec{\upsilon} = n_0 \frac{q\vec{E}}{m} + n\frac{q\vec{\varepsilon}}{m} + nq\frac{\vec{u}_0 x\vec{B}}{mc} + n_0 q\frac{\vec{\upsilon}x\vec{B}}{mc} - n\nu\vec{u}_0 - n_0\nu\vec{\upsilon} \qquad \text{(A. 4)}$$

(the 1st order equation)

β) $$n_0\vec{\upsilon}.\vec{\nabla}\vec{\upsilon}+n\frac{\partial\vec{\upsilon}}{\partial t}+n\vec{u}_0.\vec{\nabla}\vec{\upsilon}=\frac{nq\vec{E}}{m}+nq\frac{\vec{\upsilon}x\vec{B}}{mc}-n\nu\vec{\upsilon}-\frac{\vec{\nabla}p}{m} \qquad \text{(A. 5)}$$

(the 2vd order equation)

γ) And finally,

$$n\vec{\upsilon}.\vec{\nabla}\vec{\upsilon}\cong 0 \quad \text{(A. 6)}$$

(the 3rd order equation).

_ From the equilibrium state (zero order equation), the drift velocity components are easily obtained,

$$u_\theta=\frac{q\varepsilon}{m}.\frac{\omega_c}{\omega_c^2+\nu^2}=\frac{\varepsilon}{B}.\frac{\omega_c^2}{\omega_c^2+\nu^2} \quad \text{and} \quad u_r=\frac{q\varepsilon}{m}.\frac{\nu}{\omega_c^2+\nu^2}=\frac{\varepsilon}{B}.\frac{\omega_c\nu}{\omega_c^2+\nu^2}$$

_ From the first order equation, the perturbent velocity components may be given as,

$$\upsilon_\theta=\frac{qE}{m}.\frac{\omega_c}{\omega_c^2+\Pi^2}=\frac{E}{B}.\frac{\omega_c^2}{\omega_c^2+\Pi^2} \quad \text{and} \quad \upsilon_r=\frac{qE}{m}.\frac{\Pi}{\omega_c^2+\Pi^2}=\frac{E}{B}.\frac{\omega_c\Pi}{\omega_c^2+\Pi^2} \qquad \text{(A. 7)}$$

with , $\Pi=j(ku-\omega)+\nu$

A combination of drift and perturbed velocities components gives,

$$\upsilon_\theta=\frac{E}{\varepsilon}\frac{\omega_c^2+\nu^2}{\omega_c^2+\Pi^2}.u_\theta \quad \text{and} \quad \upsilon_r=\frac{E}{\varepsilon}\frac{\Pi}{\nu}\frac{\omega_c^2+\nu^2}{\omega_c^2+\Pi^2}.u_r \qquad \text{(A. 8)}$$

If it is considered that $ku-\omega \prec\prec \nu$, then it is taken $\Pi\cong\nu$ and the perturbed velocity components (eq.A. 7) become,

$$\upsilon_\theta=\frac{E}{B}.\frac{\omega_c^2}{\omega_c^2+\nu^2} \quad \text{and} \quad \upsilon_r=\frac{E}{B}.\frac{\omega_c\nu}{\omega_c^2+\nu^2}$$

as the drift velocity components by replacing the dc electric field ε with the perturbed one E .

If $ku-\omega \prec\prec \nu$, then $\Pi\cong\nu$ is taken likewise and from Eqs (A. 8) the below relations (A. 9) are obtained,

$$\upsilon_r=\frac{E}{\varepsilon}u_r \quad \text{and} \quad \upsilon_\theta=\frac{E}{\varepsilon}u_\theta \qquad \text{(A. 9)}$$

References

1. N. D' Angelo, N. Rynn. Phys. Fluids 4, 1054 (1961)
2. N.D'Angelo and R.W. Motley, Phys. Fluids 6, 423 (1963)
3. F.F. Chen, Phys. Fluids 8, 1323 (1965)
4. K Hendel H. W., Coppi B., Perkins F. and Politzer P.A. Phys. Rev. Lett. 18. 439 (1967)
5. E. Marden-Marshall, R.F.Ellis and J.E.Walsh Plasma Phys. Vol. 28 No 9B 1461 (1986)
6. J. Wesson, Tokamaks, 2nd edn.Oxford: Clarendon Press, 1997.
7. N.Krall and A.Trivelpiece, Principles of Plasma Physics, McGraw-Hill Kogakusha,LTD, 1973.
8. M. Lieberman and A. Lichtenberg, Principles of Plasma Discharges and Materials Processing , New Yprl: John Wiley & Sons, 1994.
9. Y.S. Satya and R.K.Kaw, Phys. Rev. Lett. **31**, 1453 (1973)
10. A. Anastassiades, and C.L. Xaplanteris, J. Phys.Soc. of Jpn **52,** 492 1983
11. C.L. Xaplanteris, Astrophys. Space Science 139, 233-242, 1987.
12. C.L. Xaplanteris, J. Plasma Physics, Vol. **75,** part 3 pp 395-406, 2009.
13. Klinger, in Handbook of Chaos Control, edited by H.G.Schuster (Wiley VCH, Weinheim, 1998) pp 513-562.

14. D.Block et al, Phys. Rev. E **63,** 056401, 2001.
15. C.L. Xaplanteris and E. Filippaki CHAOS 2010, International Conference Proceedings Chania, 2010.
16. C.L. Xaplanteris et al, J. Plasma Physics, Vol. **78,** Issue 02, pp 165-174, 2012


Proceedings, 5th Chaotic Modeling and Simulation International Conference, 12 – 15 June 2012, Athens Greece

Chaotic behavior of the closed loop thermosyphon model with memory effects

Justine Yasappan, Ángela Jiménez-Casas[1], and Mario Castro[2]

[1] Grupo de Dinámica No Lineal (DNL), Escuela Técnica Superior de Ingeniería (ICAI), Universidad Pontificia Comillas, Madrid E-28015, Spain
(E-mails: justemmasj@gmail.com, ajimenez@dmc.icai.upcomillas.es)
[2] ICAI, Grupo Interdisciplinar de Sistemas Complejos (GISC) and DNL, Universidad Pontificia Comillas, Madrid E-28015, Spain
(E-mail: marioc@upcomillas.es)

Abstract. This paper presents the motion of a viscoelastic fluid in the interior of a closed loop thermosyphon. A viscoelastic fluid described by the Maxwell constitutive equation is considered for the study. This kind of fluids present elastic-like behaviors and memory effects. Numerical experiments are performed in order to describe the chaotic behavior of the solution for different ranges of the relevant parameters by using the inertial manifold for this system proved in [1]. This work comes to verify the complex nature of the behavior of viscoelastic fluids extending the result in [2] when we consider a given heat flux instead of Newton's linear cooling law.

Keywords: Thermosyphon, Viscoelastic fluid, Asymptotic behavior, Numerical analysis.

1 Introduction

Chaos in fluids subject to temperature gradients has been the subject of intense work for its applications in the field of engineering or atmospheric sciences. A thermosyphon is a device composed of a closed loop *pipe* containing a fluid whose motion is driven by the effect of several actions such as gravity and natural convection [3–5]. The flow inside the loop is driven by an energetic balance between thermal energy and mechanical energy. The interest on this system comes both from engineering and as a *toy* model of natural convection (for instance, to understand the origin of chaos in atmospheric systems). The theoretical results of the behavior of viscoelastic fluids of this model has been proved in [1] but in this work we explore it numerically.

As viscoelasticity is, in general, strongly dependent on the material composition and working regime, here we will approach this problem by studying the most essential feature of viscoelastic fluids: memory effects. To this aim we restrict ourselves to the study of the so-called Maxwell model [6]. In this model, both Newton's law of viscosity and Hooke's law of elasticity are generalized and complemented through an evolution equation for the stress tensor,

σ. The stress tensor comes into play in the equation for the conservation of momentum:

$$\rho\left(\frac{\partial \mathbf{v}}{\partial t}+\mathbf{v}\cdot\nabla\mathbf{v}\right)=-\nabla p+\nabla\cdot\sigma \tag{1}$$

For a Maxwellian fluid, the stress tensor takes the form:

$$\frac{\mu}{E}\frac{\partial\sigma}{\partial t}+\sigma=\mu\dot{\gamma} \tag{2}$$

where μ is the fluid viscosity, E the Young's modulus and $\dot{\gamma}$ the shear strain rate (or rate at which the fluid deforms). Under stationary flow, the equation (2) reduces to Newton's law, and consequently, the equation (1) reduces to the celebrated Navier-Stokes equation. On the contrary, for short times, when *impulsive* behavior from rest can be expected, equation (2) reduces to Hooke's law of elasticity.

The derivation of the thermosyphon equations of motion is similar to that in [3–5]. The simplest way to incorporate equation (2) into equation (1) is by differentiating equation (1) with respect to time and replacing the resulting time derivative of σ with equation (2). This way to incorporate the constitutive equation allows to reduce the number of unknowns (we remove σ from the system of equations) at the cost of increasing the order of the time derivatives to second order. The resulting second order equation is then averaged along the loop section (as in Ref.[3]). Finally, after adimensionalizing the variables (to reduce the number of free parameters) we arrive at the main system of equations

$$\begin{cases} \varepsilon\dfrac{d^2v}{dt^2}+\dfrac{dv}{dt}+G(v)v=\oint Tf, & v(0)=v_0,\ \frac{dv}{dt}(0)=w_0 \\ \dfrac{\partial T}{\partial t}+v\dfrac{\partial T}{\partial x} & =h(x)+\nu\frac{\partial^2 T}{\partial x^2},\ T(0,x)=T_0(x) \end{cases} \tag{3}$$

where $v(t)$ is the velocity, $T(t,x)$ is the distribution of the temperature of the viscoelastic fluid in the loop, ν is the temperature diffusion coefficient, $G(v)$ is the friction law at the inner wall of the loop, the function f is the geometry of the loop and the distribution of gravitational forces, $h(x)$ is the general heat flux and ε is the viscoelastic parameter, which is the dimensionless version of the viscoelastic time, $t_V=\mu/E$. Roughly speaking, it gives the time scale in which the transition from elastic to fluid-like occurs in the fluid. We consider G and h are given continuous functions, such that $G(v)\geq G_0>0$, and $h(v)\geq h_0>0$, for G_0 and h_0 positive constants. Finally, for physical consistency, it is important to note that all functions considered must be 1-periodic with respect to the spatial variable.

2 Inertial manifold: Finite dimensional asymptotic behavior

In this section we summarize the main results related to the finite dimensional asymptotic behavior of the system of equations (3) as proved in [1]. The existence and uniqueness of the solutions of (3) was proved in [1] following the techniques used in [2]. The main idea in [2] is that we rewrite our main equations (3) in terms of the Fourier expansions of each function and observing the dynamics of each Fourier mode, where $h, f \in \dot{L}^2_{per}(0,1)$ are given by the following Fourier expansions:

$$h(x) = \sum_{k\in D} b_k e^{2\pi kix}, f(x) = \sum_{k\in D} c_k e^{2\pi kix}$$

with $D = D - \{0\}$ while $T_0 \in \dot{H}^1_{per}(0,1)$ is given by

$$T_0(x) = \sum_{k\in D} a_{k0} e^{2\pi kix}$$

and $T(t,x) \in \dot{H}^1_{per}(0,1)$ is given by

$$T(t,x) = \sum_{k\in D} a_k(t) e^{2\pi kix}$$

where

$$\dot{L}^2_{per}(0,1) = \{u \in L^2_{loc}(I\!R), u(x+1) = u(x) a.e., \oint u = 0\}, \dot{H}^m_{per}(0,1) = H^m_{loc}(I\!R) \cap \dot{L}^2_{per}(0,1). \tag{4}$$

The coefficients $a_k(t)$ verify the equation:

$$\dot{a_k}(t) + (2\pi kvi + 4\nu\pi^2 k^2) a_k(t) = b_k, \quad a_k(0) = a_{k0}, \quad k \in D.$$

Here, we assume that $h \in \dot{H}^m_{per}$ with

$$h(x) = \sum_{k\in K} b_k e^{2\pi kix}$$

where $b_k \neq 0$, for every $k \in K \subset D$ with $0 \notin K$, since $\oint h = 0$. We denote by V_m the closure of the subspace of $\dot{H}^m_{per}$ generated by $\{e^{2\pi kix}, k \in K\}$. If $b_k = 0$ then the kth mode for the temperature is dumped out exponentially and therefore the space V_m attracts the dynamics for the temperature. Moreover if K is a finite set, the dimension of $\mathcal{M}$ is $|K| + 2$, where $|K|$ is the number of elements in K.

Under the above hypotheses we assume that

$$f(x) = \sum_{k\in J} c_k e^{2\pi kix}$$

with $c_k \neq 0$ for every $k \in J \subset D$. Then on the inertial manifold we have:

$$\oint (T \cdot f) = \sum_{k \in K} a_k(t)\bar{c_k} = \sum_{k \in K \cap J} a_k(t)\bar{c_k}.$$

Therefore the evolution of velocity v, and acceleration w depends only on the coefficients of T which belong to the set $K \cap J$. From [1], using similar techniques as in [7,8] we will reduce the asymptotic behavior of the initial system (3) to the dynamics of the reduced explicit nonlinear system of ODE's (5) where we consider the relevant modes of temperature $a_k, k \in K \cap J$.

$$\begin{cases} \dfrac{dw}{dt} + \dfrac{1}{\varepsilon}w + \dfrac{1}{\varepsilon}G(v)v = \dfrac{1}{\varepsilon}\displaystyle\sum_{k \in K \cap J} a_k(t)\bar{c_k} & w(0) = w_0 \\ \dfrac{dv}{dt} = w, & v(0) = v_0 \\ \dot{a_k}(t) + (2\pi k v i + 4\nu\pi^2 k^2)a_k(t) = b_k, & a_k(0) = a_{k0}, \quad k \in K \cap J. \end{cases} \tag{5}$$

Note that the set $K \cap J$ can be much smaller than the set K and therefore the reduced subsystem may possess far fewer degrees of freedom than the system on the inertial manifold. Also note that it may be the case that K and J are infinite sets, but their intersection is finite. For instance, for a circular circuit we have $f(x) \sim a\sin(x) + b\cos(x)$, i.e., $J = \{\pm 1\}$ and then $K \cap J$ is either $\{\pm 1\}$ or the empty set.

3 Numerical experiments

3.1 Preliminary mathematical approximation

In this section, we integrate the system of ODEs (5), where we consider only the coefficients of temperature $a_k(t)$ with $k \in K \cap J$ (relevant modes). Thus,

$$\begin{cases} \frac{dw}{dt} + \frac{w}{\varepsilon} + \frac{G(v)v(t)}{\varepsilon} = \frac{2}{\varepsilon} Real\left(\sum_{k \in K \cap J} a_k(t)\bar{c_k}\right) & w(0) = w_0 \\ \frac{dv}{dt} = w, & v(0) = v_0 \\ \dot{a_k}(t) + a_k(t)(2\pi k i v + \nu 4\pi^2 k^2) = b_k, & a_k(0) = a_{k0}. \end{cases}$$

We impose that all the physical observable as real functions, then $a_{-k} = \bar{a}_k$, $b_{-k} = \bar{b}_k$ and $c_{-k} = \bar{c}_k$. In particular, we consider a thermosyphon with a circular geometry, so $J = \{\pm 1\}$ and $K \cap J = \{\pm 1\}$. Consequently, we can take $k = 1$ and omit the equation for $k = -1$ (is conjugated of the equation for $k = 1$). Also in order to reduce the number of free parameters we make the following change of variables $a_1 c_{-1} \to a_1$.

$$\begin{cases} \frac{dw}{dt} = \frac{2a_1}{\varepsilon} - \frac{w}{\varepsilon} - \frac{G(v)v(t)}{\varepsilon}, & w(0) = w_0 \\ \frac{dv}{dt} = w, & v(0) = v_0 \\ \dot{a_1}(t) + a_1(t)(2\pi i v + \nu 4\pi^2) = b_1, & a_1(0) = a_{10}. \end{cases}$$

We denote the real and imaginary parts of the $a_1(t)$ (the Fourier mode of the temperature) in the following way:

$$a_1(t) = a^1(t) + i a^2(t), \tag{6}$$

$$b_1 = A + iB \tag{7}$$

with $A \in I\!R, B \in I\!R$. Thus we obtain the corresponding nonlinear system of equations where we need to make explicit choice of the constitutive laws for both the fluid-mechanical and thermal properties for this model:

$$\begin{cases} \frac{dw}{dt} = \frac{2a^1}{\varepsilon} - \frac{w}{\varepsilon} - \frac{G(v)v(t)}{\varepsilon}, & w(0) = 0 \\ \dot{v} = w, & v(0) = 0 \\ \dot{a^1} = A - \nu 4\pi^2 a^1 + v2\pi a^2, & a^1(0) = 1 \\ \dot{a^2} = B - \nu 4\pi^2 a^2 - v2\pi a^1 & a^2(0) = 1. \end{cases} \tag{8}$$

Hereafter, we present the numerical experiments of equations (5) that are carried out for the resolution of the nonlinear system of ODEs using the fourth-order explicit Runge-Kutta method. The summary of our results is presented in the figures of section 3.2. In particular, we present the plots for velocity, acceleration and (the fourier transform of the) temperature of this system. All the variables and equations that we deal with are adimensional. As the system is multidimensional, we present the results in temporal graphs (variables vs time) and phase-space graphs (two physical variables plot against each other).

In all cases, we take the same mathematical form for the friction law, $G(v) = (|v| + 10^{-4})$, as used in the previous works (see, for instance, [2,7,8]), for a similar model of thermosyphon with a non-viscoelastic fluid with one component. The rationale behind this equation is that it interpolates between a constant (low Reynolds number laminar flow) and a linear (highly turbulent flow) function of the velocity. Likewise, A and B, which refer to the position-dependant (x) heat flux inside the loop will be used as tuning parameters. We will assume $A = 0$ in order to simplify, as different values of A only changes the *phase* the periodic function $h(x)$. We will also fix $B = 50$ the heat flux parameter, $\nu = 0.002$ the diffusion coefficient and observe the evolution of the variables. The initial conditions are fixed to $w(0) = 0, v(0) = 0, a^1(0) = 1, a^2(0) = 1$. Finally, we have also studied the behavior of the system of equations by keeping ε as a tuning parameter ranging from 1 to 10, to observe the response of the system under the effects of viscoelasticity.

3.2 The chaotic behavior of the model

The impact of ε on the system has been keenly observed for various parameters. In general (see below), as the viscoelastic component ε increases, the chaotic behavior of the system also increases. In Fig. 1 we show the time evolution of the acceleration, $w(t)$, for the viscoelastic parameter $\varepsilon = 1$. The acceleration $w(t)$ ranges from -15 to 15. The plot is chaotic but, although this is more apparent in the acceleration plot than in the velocity one. This is reasonable as the velocity is the time integral of the acceleration, namely, the velocity curve looks smoother than that of acceleration (therefore the chaotic behavior is not so apparent).

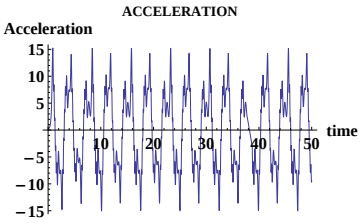

Fig. 1. The time evolution of the acceleration, $w(t)$, with $\varepsilon = 1$, $A = 0$, $B = 50$, $\nu = 0.002$ and $G(v) = (|v| + 10^{-4})$

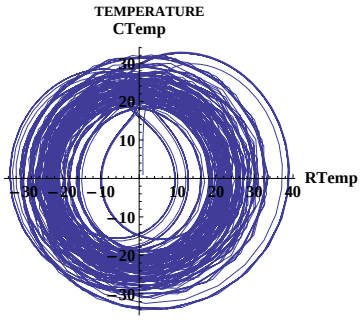

Fig. 2. Phase-plane of the real and imaginary parts of Fourier transform of the temperature for $\varepsilon = 1$, $A = 0$, $B = 50$, $\nu = 0.002$ and $G(v) = (|v| + 10^{-4})$.

In Fig. 2 we show the phase-diagram for the real $a^1(t)$ and imaginary $a^2(t)$ parts of the Fourier transform of the temperature. As expected, the trajectory in this phase-plane moves inwards and outwards. This plot illustrates the underlying complex dynamics of the attractor as a two dimensional projection.

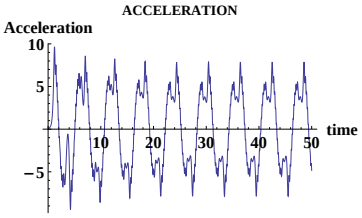

Fig. 3. The time evolution of the acceleration, $w(t)$, with $\varepsilon = 3$, $A = 0$, $B = 50$, $\nu = 0.002$ and $G(v) = (|v| + 10^{-4})$

In the second set of numerical experiments we increase the value of viscoelastic component to $\varepsilon = 3$. As the value of viscoelastic component ε is relatively higher than the previous experiment i.e., $(\varepsilon = 3)$ the system tends to be more chaotic than the previous experiment. The acceleration $w(t)$

ranges from -10 to 10. The deviation in the progress of acceleration is maintained till the end of the progress. Apparently, the behavior is also chaotic but this chaos seems to be embedded in larger timescale oscillations. Interestingly, the number of oscillations is reduced from 15 to 9, Fig. 3 showing less number of peaks than the first case. This is a reflection of the memory effects associated to the viscoelastic of the fluid. Thus, as ε plays the role of a time scale, the larger this value the longer are the memory effects (in our case exposed through the period of the underlying oscillations).

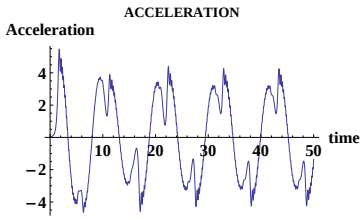

Fig. 4. The time evolution of the acceleration, $w(t)$, with $\varepsilon = 10$, $A = 0$, $B = 50$, $\nu = 0.002$ and $G(v) = (|v| + 10^{-4})$

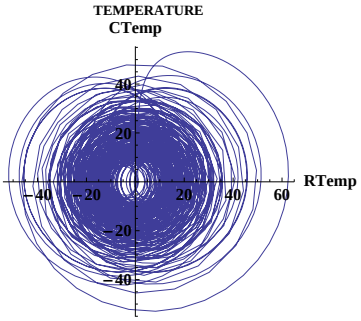

Fig. 5. Phase-plane of the real and imaginary parts of Fourier transform of the temperature for $\varepsilon = 10$, $A = 0$, $B = 50$, $\nu = 0.002$ and $G(v) = (|v| + 10^{-4})$.

For $\varepsilon = 10$ (Fig. 4), the system still exhibits a chaotic progression, with the acceleration ranging from -4 to 4 and with even an underlying longer-period oscillations compared to the previous experiments.

Finally, in Fig. 5 we show the phase-diagram for $a^1(t)$ and $a^2(t)$. Again, as expected, the trajectory in this phase-plane moves inwards and outwards. This plot illustrates the underlying complex dynamics of the attractor of a two dimensional projection.

In summary, larger values of the viscoelastic parameters ε, results in sustained chaotic behaviors overlapped with an (almost) periodic behavior whose

period scales with the numerical value of ε. The dynamics becomes more complex and is characterized in all cases by periods of chaos and of violent oscillations, giving an idea of the complexity of the solutions of the system under these variables due to memory effects.

4 Conclusion

The physical and mathematical implications of the resulting system of ODEs which describe the dynamics at the inertial manifold is analyzed numerically. The role of the parameter ε which contains the viscoelastic information of the fluid was treated with special attention. We studied the asymptotic behavior of the system for different values of ε the coefficient of viscoelasticity. We can conclude that for larger values of ε the system behaves more chaotic. Physically, this induction of chaotic behaviors is related to the memory effects inherent to viscoelastic fluids. Thus, in the same way as delayed equations are known to produce chaos, even in the simplest situations, viscoelasticity produces the same kind of transition.

Acknowledgements

This work has been partially supported by Projects MTM2009-07540, GR58/08 Grupo 920894 BSCH-UCM, Grupo de Investigación CADEDIF and FIS2009-12964-C05-03, SPAIN.

References

1.A. Jiménez-Casas, Mario Castro, and Justine Yasappan. Finite-dimensional behavior in a thermosyphon with a viscoelastic fluid. submitted, 2012.
2.Justine Yasappan, A. Jiménez-Casas, and Mario Castro. Asymptotic behavior of a viscoelastic fluid in a closed loop thermosyphon: physical derivation, asymptotic analysis and numerical experiments. submitted, 2011.
3.J.B. Keller. Periodic oscillations in a model of thermal convection. *J. Fluid Mech.*, 26:599–606, 1966.
4.P. Welander. On the oscillatory instability of a differentially heated fluid loop. *J. Fluid Mech.*, 29:17–30, 1967.
5.J.J.L. Velázquez. On the dynamics of a closed thermosyphon. *SIAM J. Appl. Math.*, 54:1561–1593, 1994.
6.F. Morrison. Understanding rheology. *Oxford University Press, USA*, 2001.
7.A. Jiménez-Casas, and A.M-L. Ovejero. Numerical analysis of a closed-loop thermosyphon including the Soret effect. *Appl. Math. Comput.*, 124:289-318, 2001.
8.A. Rodríguez-Bernal, and E.S. Van Vleck. Diffusion Induced Chaos in a Closed Loop Thermosyphon. *SIAM J. Appl Math.*, 58:1072-1093, 1998.

THE PRINCIPLES OF FUNCTIONING OF THE "PERIPHERAL HEART"

I.V. Zapuskalov, O.I. Krivosheina, Y.I Khoroshikh, O.B.Zapuskalova
Siberian State Medical University, Tomsk, Russia
E-mail: izapuskalov@yandex.ru

Abstract: on the base of theoretical research using the laws of physics and cybermathematics there was suggested the mechanism of regulation and functional system of peripheral bloodstream - "peripheral heart".

Keywords: the peripheral bloodstream, the Laplace's law, the mechanisms of myogenic autoregulation, "peripheral heart".

The term "peripheral heart," proposed by the Russian scientist M.V. Yanovskii, has gained the widest popularity in the early 20th century. Its meaning is the following: contracting, the left ventricle forces blood into the largest vessel – aorta. Using peristaltic pulsations, aorta pumps blood further to all organs and tissues, thus helping to the heart and playing the active role in the circulation.

The peripheral bloodstream looks like a branching network of pliable tubules. In adults at rest, the heart pumps blood into this network in the amount of 4–5 L/min at a pressure of about 100 mm Hg. During every systole, the heart ejects about 70 ml of blood into the aorta and ostia of major arteries, which serve as a reservoir for the following parts of the arterial system. During diastole, the elastic walls of this reservoir relax and this provides for the inflow of blood at the corresponding pressure to peripheral parts of the arterial bloodstream. However, not only large elastic, but also small muscular arteries are subject to stretching upon the passage of the pulse wave. This is illustrated, for example, by the results of investigation of the eye hemodynamics with the aid of ophtalmodynamography, determination of the eye-orbital pulsation on the basis of the nuclear gamma-resonance effect, plethysmography, and rheorgaphy. The healthy pulse volume of the eye ranges within 23–27 mm^3. If we compare the eye pulse

volume with the systolic volume of the heart relative to the tissue mass (eye weight of about 5 g, body weight of 70 kg, systolic discharge of 70 см^3 – 100 %), then the eye pulse volume makes up as high as 245%! Certainly, the eye should not be compared with other tissues, in which the blood flow intensity is much lower, but it can be concluded that the nearly whole pulse wave goes into the peripheral muscular vessels.

The viscoelastic properties of the walls of muscular arteries differ widely from those of arteries of the elastic type. The point is that the small muscular arteries (500–140 μm in diameter) and arterioles (140–10 μm) are analogous in their structure to stretchable elastic tubules, and therefore the processes, proceeding in them, can be described, with some assumption, by the Laplace's law:

$$F = P \cdot R,$$

where F is the stretching force, P is the transmural pressure, and R is the tubule radius. It follows from this law that the pressure needed to stretch the tubule against the hoopential stress is inversely proportional to the tubule radius.

The elastic properties of the vessel walls are determined by the elastin and collagen fibers and depend on the activity of smooth muscular cells. Elastin is a rubber-like material, whose modulus of elasticity is roughly equal to $3 \cdot 10^5$ N·m^{-2}. Collagen is much more rigid than elastin, and its modulus of elasticity is roughly equal to 10^8 M·m^{-2}. At small deformations, the most part of collagen fibers is relaxed and not stretched along a straight line, while the stress is created by the elastin fibers. As the radius increases, the collagen fibers become straight and take the growing part in the creation of the stress. Since they are much more rigid than the elastin fibers, the wall becomes more rigid as well.

The arteries of the muscular type, pulsations of the blood pressure serve as the correcting force acting from the inside, while the myogenic autoregulation serves as the correcting force from the outside. The modulus of elasticity of smooth muscles is nearly identical to that of elastin. Its experimentally determined values depend on the level of physicological activity and can vary from

$1 \cdot 10^5$ N·m^{-2} to $2 \cdot 10^6$ N·m^{-2} in the active state. In small arteries and arterioles, the percentage of smooth muscles in the walls achieves 60%, and this allows them to adjust easily to various oscillations of the transmural pressure.

It was W. M. Bayllis, who put forward the hypothesis of myogenic autoregulation for the first time in 1902. There are many proofs that the tone of the smooth vascular muscles varies as the intravascular pressure changes. First, very short-time arterial occlusion (shorter than 2 s) leads to significant vasodilatation. Second, the pressure drop on the outer side of an organ leads to pronounced vasocontraction. Third, the increase of the venous pressure causes the increase of the precapillary resistance in some organs (closing of precapillary sphincters and metarterioles). Fourth, the increase of the static intravascular pressure in arterioles in the absence of blood flow leads to the marked contraction of arterioles. Vessels remain narrow as long as the pressure increases. The return of the pressure to the initial level causes dilatation of arterioles.

There exist two hypotheses, explaining the mechanisms of myogenic autoregulation. B. Folkov supposed that the passive stretching leads to the increase in the spontaneous frequency of discharges of smooth muscles. As the intravascular pressure rises, the smooth muscular cell stretches, and this hastens the beginning of the next contraction. If the cell is constricted or contracted, its length no longer exceeds the normal length, there is no stimulus for contraction, and the muscular cell relaxes. However, as soon as the cell relaxes, the increased pressure again forces the cell stretching to the length exceeding the initial length, due to which the second contraction occurs earlier than in norm. Since the frequency of discharges in the smooth muscular cell increases, it is in the state of contraction for longer time. This contraction becomes from the precapillary arterioles and then spread to the larger arterial vessels of the muscular type.

The second hypothesis assumes that the smooth muscular cells have stress receptors, rather than length receptors, as is assumed in the above hypothesis. According to the Laplace equation, the hoopential stress of a vessel depends on both the intravascular pressure and the vessel radius. The growth of the

pressure causes the increase of the wall stress, which leads to the contraction of the smooth muscles of the vessel. As the contraction develops and the radius decreases, the wall releases from the stress. This supposed mechanism includes the negative feedback, which restricts the contraction, arising upon the increase of the transmural pressure.

On the basis of the literature data presented and the results of our investigations, we have put forward the following hypothesis: for every pulse wave in arteries of the muscular type, the myogenic contraction of smooth muscular cells arises in response to the stretching, and this contraction forces the vessel to return to the initial state. As soon as the vessel radius decreases to the equilibrium state, that is, the contracting force becomes balanced with the transmural pressure (taking into account the Laplace law), the smooth muscular fibers relax and the vessel is ready to perception of a new pulse wave.

The refractory period of muscular cells amounts to about 0.1 s. As a result, the muscular cells favors the propagation of the pulse wave to the periphery in large arteries and cumulate this wave in small arteries.

Thus, the systolic wave is almost completely absorbed in the free-stretching peripheral arteries, and the following active contraction of muscular cells creates the diastolic blood pressure.

Myogenic autoregulation in arterioles

As muscular arteries branch and become smaller, transforming into arterioles, their walls become thinner and the lumen becomes narrower. The ratio of the wall thickness to the lumen diameter, however, keeps nearly constant. This ratio, along with the approximately estimated number of layers of smooth-muscular cells in the middle tunic is a criterion widely used for identification of arterioles. In small arterioles, the inner and outer elastic membranes become very thin and even absent in smallest arterioles (smaller than 35 μm in diameter). The outer tunic of small arterioles is very thin and consisting mostly of collagen fibers. The smooth-muscle cells of the middle tunic of small arterioles have, correspondingly, the smaller size.

One can see from Fig. 1 that the diameter of arterioles can vary significantly. Since the state of arterioles is described by the Laplace law, only the myogenic effect can play the leading role here.

The myogenic autoregulation of arterioles performs their basic function – preservation of the capillary pressure at a constant level. The factors, determining the capillary pressure, can be expressed as follows:

$$P_c = P_v + P \cdot R_v ,$$

where P_c is the capillary pressure, P_v is the venous pressure, P is the blood flow, R_v is the venous resistance.

The diameter of arterioles, as well as muscular arteries, is highly dynamic and depending on the intravascular pressure. The higher is the pressure in arterioles, the narrower are they (up to the complete blockage of the blood flow). To the contrary, the decrease of the pressure leads to the widening of arterioles until the smooth-muscular cells relax completely and only the viscoelastic forces of elastic fibers resist to the transmural pressure. This state corresponds to the critical positive value of the arterial pressure, below which the contracting force of the elastic fibers exceeds the stretching pressure and the vessel collapses. As this takes place, some lumen still exists in large arterioles, while smaller ones are fully blocked and the blood flow in them ceases.

As was already mentioned, the maximal diameter is determined by the collagen skeleton, whose modulus of elasticity is many times higher than that of elastin and muscular fibers. As to the minimal diameter, it depends on the thickness of the inner and outer elastic membranes of the vascular wall, and if these membranes are absent, then the vessel can be fully blocked.

One can see from Fig. 1 that the minimal diameter of arterioles, capillaries, and venules is nearly equal to zero. In the literature, this state is often described as “emptiness” of a vessel. We believe that this term is not adequate to the reality. Emptiness means some capacity free of its content, for example, an empty bottle. However, blood vessels in norm cannot be empty (except for the case of gas embolism). If they become invisible, this means that their lumen has approached a diameter, insufficient for an erythrocyte to pass through, that is, nearly zero. In capillary and

venules, the diameter becomes equal to zero, as the transmural blood pressure drops down below the critical positive pressure. Such a "collapse" is possible either when the studied vessel is pinched from the outside or when the inflow arteriole is blocked. The collapse usually starts from the arterial end of a capillary, because it is the narrowest part of the vascular bed and the stretching force hear is lower (according to the Laplace law), and spreads toward venous vessels.

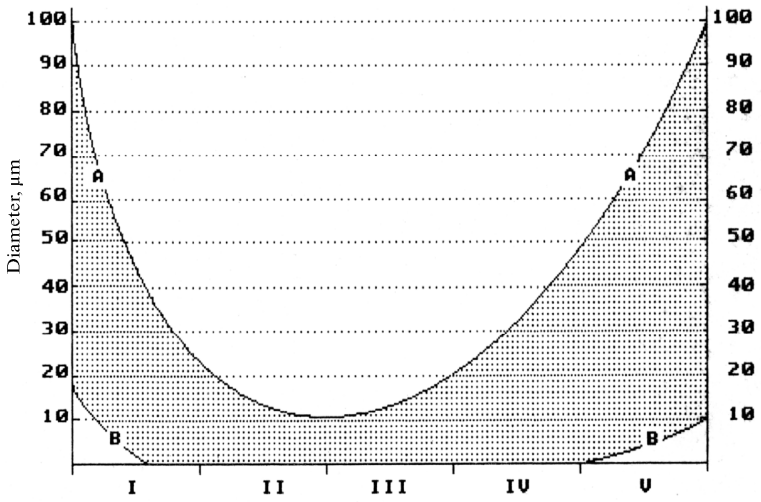

Fig. 1 Schematic of vessels of the eye conjunctiva (according to the results of vasotonometry): (A) maximal vessel diameter; (B) minimal vessel diameter; (I) muscular arteries; (II) arterioles; (III) capillaries; (IV) venules; (V) small veins.

In an arteriole, in contrast to capillary and venules, the blood flow can be blocked due to both the collapse (for example, at obstruction of the central retinal artery) and the active myogenic narrowing, which, to the contrary, arises at the increased transmural pressure.

In the biomicrospcopic investigations of the microcirculatory bed of the bulbar conjunctiva, the blood flow in

the form of isolated blood portions can be often observed. Some authors explain this character of the blood flow as a result of the inertial propagation of the pulse wave. However, this treatment, in our opinion, has little force. In microvessels, the character of the blood flow is mostly determined by the viscous forces, rather than inertial ones, because the Reynolds numbers here are very low: typically, about 0.5 for arteries 100 μm in diameter and lower than 0.05 for capillaries 10 μm in diameter. The pressure and blood flow in these vessels may remain pulsating, but at any point and at any time the character of the flow is determined only by the balance between the pressure and the viscous forces. The inertial forces, that is, forces associated with local and convective accelerations, are negligibly weak in this case. Consequently, the blood flow by portions can be caused only by the wavy contraction of the muscular wall of arterioles, which can also be considered as an element of the "peripheral heart."


Proceedings, 5th Chaotic Modeling and Simulation International Conference, 12 – 15 June 2012, Athens Greece

Complex Dynamics of Multiparticle System Governed by Bounded Rationality

Arkady Zgonnikov[1] and Ihor Lubashevsky[2]

[1] University of Aizu, Fukushima, Japan
(E-mail: arkadiy.zgonnikov@gmail.com)
[2] University of Aizu, Fukushima, Japan
(E-mail: i-lubash@u-aizu.ac.jp)

Abstract. We consider a system of interacting elements that mimic certain properties of human perception, namely, the bounded capacity of ordering events, actions, etc. according to their preference. Previously this feature was described by the notion of dynamical traps, which is modified in the present work in order to take into account the imperfectness of human perception of their own actions. Numerically we demonstrate that the considered system under the presence of dynamical traps of a new type exhibits complex dynamics, including highly irregular motion.
Keywords: Complex dynamics, multiparticle systems, dynamical traps.

1 Introduction

The employment of various physical models in social sciences could be observed during last decades. Among the models that are used widely in studying cooperative phenomena in social systems are multi-particle dynamical models (see, e.g., Helbing and Mólnar[1], Ohnishi[2]). Advances in this field, though, face the fact that human beings indeed differ in their basic properties from the objects of the inanimate world described by Newtonian mechanics. This fact may lead one to the problem of development of new physical notions that should be introduced in addition to the well-studied ones of the modern physics in order to reflect the essential aspects of human behavior in social systems.

Mathematical notion of equilibrium points is one of the cornerstones of the modern physics; it is also widely used in social psychology (see, e.g., Vallacher[3]). However, human as a key acting element of the dynamical systems is often not capable to clearly recognize the desired equilibrium position among a certain set of its neighboring points in the corresponding phase space. This feature of human cognition is referred to as bounded or fuzzy rationality (Dompere[4]). The application of the dynamical traps notion as a mathematical formalism for describing human fuzzy rationality was investigated by Lubashevsky[5]. To briefly review this concept, let us appeal to the car following theory and consider hypothetical dynamical system controlled by an operator whose purpose is to maintain the system near the equilibrium point set to the origin. The system of equations describing the system

dynamics under the control of the operator take the following form

$$\begin{aligned} \dot{x} &= v, \\ \dot{v} &= \Omega(x,v)F(x,v,a_{opt}(x,v)). \end{aligned} \tag{1}$$

Here x and v are the system coordinate and velocity, respectively; a_{opt} is optimal in some sense control strategy chosen by the operator. The cofactor $\Omega(x,v)$ equals unity for all values of (x,v) that are far enough from the equilibrium point and $\Omega(x,v) \ll 1$ in a certain neighborhood $\mathbb{Q}_{tr}$ of the equilibrium point. In order to explain the meaning of the cofactor $\Omega(x,v)$ we consider the behavior of the operator who is approaching desired phase space position $(x=0, v=0)$. Let us assume that if the current position is far from the origin, the operator perfectly follows the optimal control strategy. If the current position is recognized by the operator as "good enough" ($(x,y) \in \mathbb{Q}_{tr}$) (though it may be not strictly optimal) due to her fuzzy rationality, she halts active control over the system so that the system dynamics is stagnated in a certain vicinity of the desired position (in case of stable equilibrium). Therefore, $\mathbb{Q}_{tr}$ is called the area of dynamical traps.

Previous studies on the dynamical trap effect in chains of particles governed by equations of form (1) have shown that it may cause complex cooperative phenomena to arise in the systems under the presence of white noise (Lubashevsky *et al.*[6]), as well as in the systems without the influence of stochastic factors (Lubashevsky[5]). However, it should be taken into account that in the real world the operator cannot usually affect the system velocity directly as prescribed by equations (1), e.g., in the car following the operator is not able to directly affect the speed of the car and in fact controls only the acceleration (Lubashevsky[7]).

It should also be noted that the operator perception of her own actions is not perfect, and could also be described in terms of fuzzy rationality. Namely, the value of the actual control effort could be treated as an acceptable by the operator if its deviation from the optimal strategy is of low magnitude. Therefore, in order to take into account the issues discussed above, in present work we introduce the dynamical trap model of a new type. While previously the dynamical trap region was referred to as two-dimensional region in the "coordinate-velocity" phase space, we propose the concept of the dynamical trap in the "space" of behavior strategies as a certain neighborhood of the optimal one.

The purpose of the current paper is to demonstrate that bounded rationality of human cognition in perceiving their own actions could be responsible for intrinsic cooperative phenomena in the systems of interacting elements under the control of human operators.

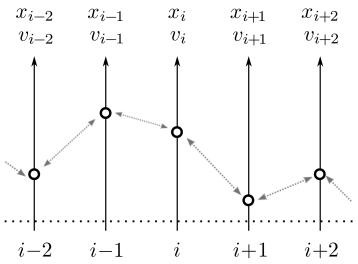

Fig. 1. The chain of N motivated particles moving along parallel axes. Terminal particles $i = 0$ and $i = N + 1$ are fixed at $x = 0$. Dotted arrows indicate the interaction between neighboring particles.

2 Model

Let us consider the chain of N motivated particles (Fig. 1) moving along parallel vertical axes; the motion of each particle is characterized by its coordinate x_i, velocity v_i and acceleration a_i. Each particle tends to minimize the absolute values of its relative coordinate and velocity with rescept to its neighbors, namely, $\eta_i = x_i - \frac{1}{2}(x_{i-1} + x_{i+1})$ and $\vartheta_i = v_i - \frac{1}{2}(v_{i-1} + v_{i+1})$. Two terminal particles are assumed to be fixed: $x_0(t) \equiv x_{N+1}(t) \equiv 0$. The dynamics of such system could be described by the following equations

$$\begin{aligned} \dot{x}_i &= v_i, \\ \dot{v}_i &= a_i, \\ \dot{a}_i &= \Omega_a(a_i, a_{opt}\big(\eta_i, \vartheta_i, v_i)\big)\big(a_{opt}(\eta_i, \vartheta_i, v_i) - a_i\big), \end{aligned} \tag{2}$$

for $i = \overline{1, N}$. Here

$$a_{opt}(\eta, \vartheta, v) = -\Omega_\vartheta(\vartheta)(\eta + \sigma\vartheta + \sigma_0 v) \tag{3}$$

is the optimal strategy of the operator behavior which is considered to depend mainly on the current values of the relative position η and velocity ϑ. σ could be treated as a relative weight of the velocity variations as a stimulus causing operator actions (with respect to the first stimulus η_i); $\sigma_0 v_i$ stands for the friction force which characterizes the physical properties of the environment where the system is placed ($\sigma_0 \ll 1$). The dynamical trap effect in system (2), (3) is modelled by cofactors Ω_ϑ and Ω_a defined as follows

$$\begin{aligned} \Omega_\vartheta(\vartheta) &= \frac{\Delta_\vartheta + \vartheta^2}{1 + \vartheta^2}, \\ \Omega_a(a, a_{opt}) &= \frac{\Delta_a + (a_{opt} - a)^2}{1 + (a_{opt} - a)^2}, \end{aligned} \tag{4}$$

where parameters $0 \le \Delta_\vartheta, \Delta_a \le 1$ determine the intensity of dynamical traps: the less these parameters, the stronger the effect of corresponding dynamical traps.

It should be pointed out that we assume the former dynamical trap cofactor Ω_ϑ not to depend on particle coordinate; it could be explained in such a manner that the control over system relative velocity ϑ is of prior importance for the operator comparing to the control over position η. Thus, if the relative velocity becomes sufficiently small, the operator prefers to retard the correction of the coordinate in order not to make the velocity variations take undesirably large values (Lubashevsky[5]).

The cofactor Ω_a in (2) stands for the dynamical trap effect of a new type which was not studied previously. Assuming $\Omega_a = 1$, one could easily see that the last equation in (2) in fact implies the equality $a_i = a_{opt}()$. However, we consider that the operator, first, is hardly able to precisely implement the strategy a_{opt} defined by (3), and, second, cannot distinguish between the strategies that are close in some sense to the optimal one. Therefore, one may think of a certain neighborhood of the optimal strategy in the space of all possible strategies, such that each strategy from this region is treated as the optimal one by the operator. So in case the operator feels that current control regime is optimal, she just keeps maintaining the current value of the control effort constant so that $\dot{a} \approx 0$. When the operator realizes that the current strategy is far from the optimal one, she starts adjusting it to the desired value which means that $\dot{a} \sim (a_{opt} - a)$.

These speculations led us to the system (2)–(4) as a model that may reflect some of mentioned properties of human bounded rationality. The rest of the paper is devoted to the analysis of anomalous cooperative phenomena that could be observed in such system for various values of system parameters.

3 Numerical simulation

In the current work we present the results of the preliminary analysis of system (2)–(4). The scope of the future work should comprise certain extensions of the proposed model; to be specific, the characteristic time scale of the system dynamics should be taken into account, as well as the thresholds of the velocity and acceleration perception. Here we consider all these parameters to take values equal to unity.

We analyze numerically the collective behavior of the particle chain by solving equations (2)–(4) using the standard $(4, 5)$-Runge-Kutta algorithm. Due to the fact that the behavior of the studied system significantly varies depending on the number of interacting particles, the below analysis is divided into three parts according to the cases $1) N = 1, 2$; $2) N = 3$; $3) N \geq 4$. We should specify that all of the following results were obtained for small values of parameters Δ_ϑ and Δ_a, namely 0.001, which correspond to the strong effect of dynamical trap. Below all phase space portraits depict projections of 3-dimensional phase trajectories on the "coordinate-velocity" plane generated by the system motion during the time interval of $T = 10^4$ given small randomly assigned initial disturbances. In case of multi-particle chains the

middle particles trajectories are represented; particle motion structure is similar for all particles in the given ensemble, however, particles in the center of the chain have slightly larger fluctuations amplitude.

The numerical simulation of the single particle oscillating between its two fixed neighbors ($N = 1$) figures out that the combination of two dynamical traps causes the limit cycle to arise in the system phase space, while without the dynamical trap effect the system has single stable fixed point ($x = 0, v = 0, a = 0$). Also it is notable that the previous studies discovered the stable behavior of the single oscillator under the presence of the single dynamical trap characterizing the fuzzy rationality in perceiving the velocity variations (Lubashevsky[5]).

First let us consider the case of the single particle oscillating between two fixed neighbors. The phase portrait and phase variables distributions of the system motion are depicted on Fig.2*a-c*. The chain of two interacting particles exhibits the similar behavior patterns (see Fig.2*d-i*), except for the phase trajectories assymetry caused by the introduction of the second oscillator. In both cases the structure of the limit cycles is stable with respect to variations of the system parameters. Namely, the found pattern remains for the following values of system parameters: $\sigma = 1,\ 3$; $\sigma_0 = 0,\ 0.01,\ 0.1$.

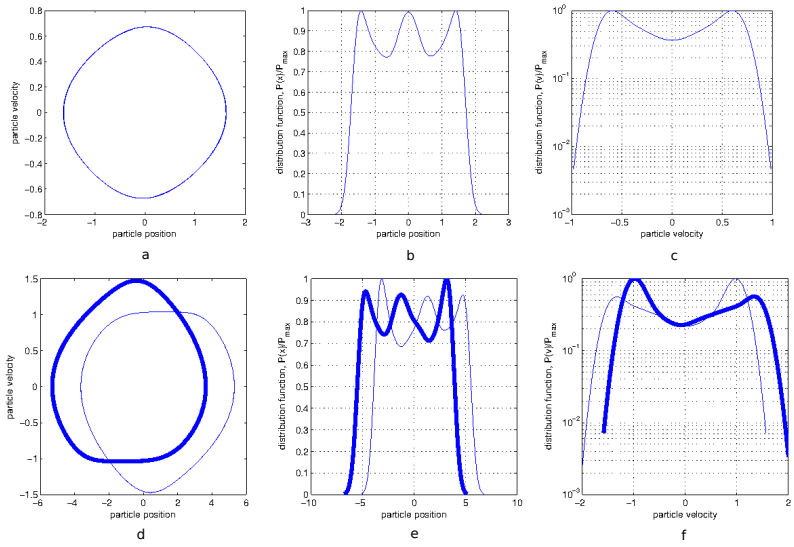

Fig. 2. The phase trajectory projections of system (2)–(4) for $N = 1$ (a) and $N = 2$ (d) on the "coordinate-velocity" plane. The right four frames show corresponding phase variables distributions. On figures (d)–(f) thin and thick lines are introduced in order for one to distinguish between two moving particles. Parameters used for simulation are $\sigma = 1$, $\sigma_0 = 0.01$.

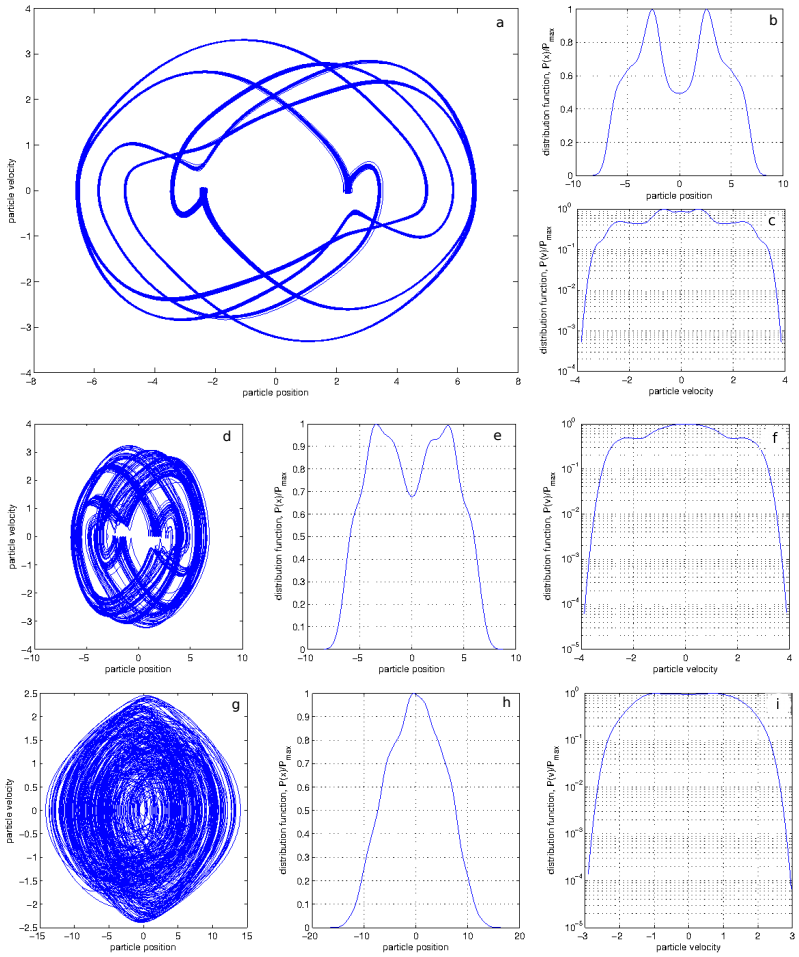

Fig. 3. The phase trajectory projections of the middle particle from the ensemble (2)–(4) and corresponding phase variables distributions for $N = 3$. Frames *a-c* illustrate the case $\sigma = 1, \sigma_0 = 0$, frames *d-f* depict the case $\sigma = 1, \sigma_0 = 0.01$, frames *g-i* are for the values of parameters $\sigma = 3, \sigma_0 = 0$

From Fig.2 it could be seen that the dynamical trap effect causes the instability of the single particle motion; the limit cycle emerges. The similar phenomena could be observed in almost the same form for each particle in the pair of coupled oscillators. The situation dramatically changes when the ensemble of three particle is taken into consideration. Adding just one more oscillator to the system causes the anomalous cooperative phenomena to emerge, particularly, complex 3-dimensional attractor arises in the system phase space (see Fig.3*a-c*).

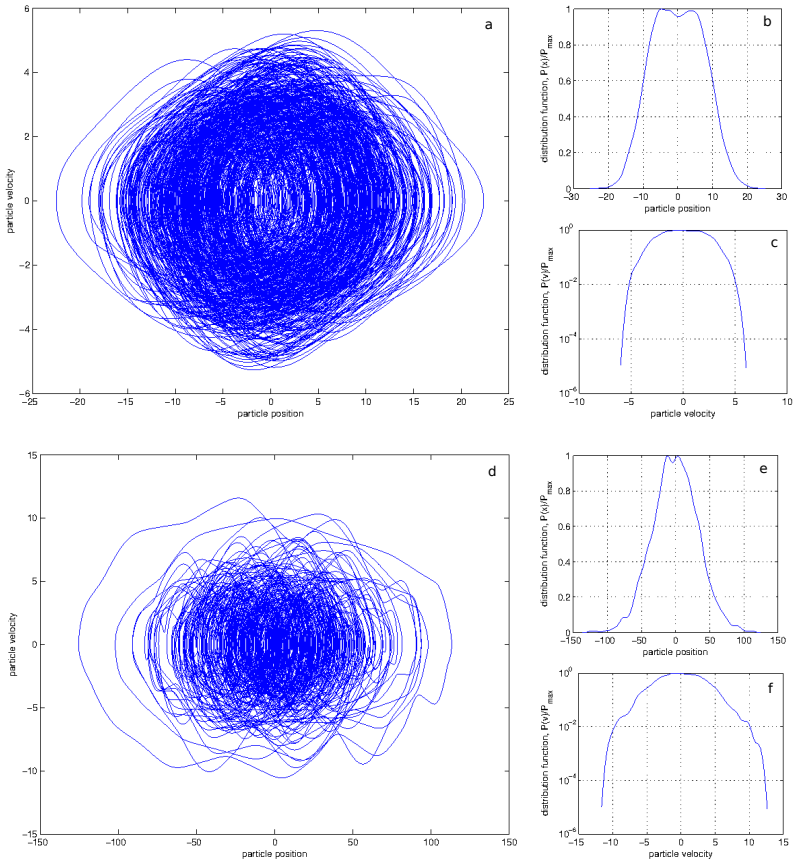

Fig. 4. The phase trajectory projections and phase variables distributions of the middle particle from the chain (2)–(4) for $N = 4$ (figures *a-c*) and $N = 15$ (figures *d-f*). Parameters used for simulation are $\sigma = 1$, $\sigma_0 = 0$.

Notably, unlike the previous cases ($N = 1, 2$), introducing the external friction force ($\sigma_0 \neq 0$) causes the attractor to become significantly blurred (see Fig.3*d-f*), while increasing the relative weight of the particle velocity as the stimulus for the operator actions makes the particle dynamics to take form of chaotic oscillations (Fig.3*g-i*).

In case of the relatively large number of interacting elements the system dynamics becomes highly irregular. The chain of four particles demonstrate the oscillatory behavior as could be seen on Fig.4*a-c*. It is worth underlining that the well-defined attractor (Fig.3*a*) could be destructed just by adding one particle to the ensemble (Fig.4*a*) without changing any of the system parameters.

The system motion trajectories for $N = 15$ (Fig.4*d-e*) are of even greater irregularity due to the increased number of particles and corresponding cooperative effect. For larger N the system motion exhibits the patterns of similar structure, but the amplitude of the fluctuations increases with N).

4 Conclusion

In the present paper we discuss the new type of the dynamical trap – a model describing human bounded rationality. The standard "coordinate-velocity" phase space inherited from the Newtonian mechanics is proposed to be extended by the acceleration variable. By analyzing the behavior of the motivated particles chain governed by bounded rationality we demonstrate that the multi-particle system under the presence of the dynamical trap of a new type exhibits intrinsic cooperative behavior. The various complex patterns of the system motion are shown to arise depending on the system parameters. First, it is demonstrated that the dynamical trap effect of a new type can cause the instability in the single oscillator dynamics which was not observed in the previous studies on the dynamical traps model. Second, the system dynamics patterns are shown to take the complex 3-dimensional structure in case of three-particle ensemble. Third, we demonstrate that with the increasing number of elements the system motion becomes significantly irregular, for large N exhibiting chaotic oscillations. The obtained results confirm that the system under consideration could exhibit anomalous behavior; however, the proposed model require more detailed analysis.

Acknoledgements: The work was supported in part by the JSPS "Grants-in-Aid for Scientific Research" Program, Grant №245404100001.

References

1.D. Helbing, P. Molnar. Social force model for pedestrian dynamics. *Phys. Rev. E*, 51:4282–4286, 1995.
2.T. Ohnishi. A multi-particle model applicable to social issues—time-evolution of Japanese public opinion on nuclear energy. *Annals of Nuclear Energy*, 29:15, 1747–1764, 2002.
3.R.R. Vallacher. Applications of Complexity to Social Psychology, in *Encyclopedia of Complexity and Systems Science*, ed. R.A. Meyers (Springer Science+Business Media, LLC., New York, 2009), pp.8420–8435.
4.K.K. Dompere. Fuzzy Rationality. Springer-Verlag, Berlin, 2009.
5.I. Lubashevsky. Dynamical traps caused by fuzzy rationality as a new emergence mechanism. *Advances in Complex Systems*, in press, 2012.
6.I.A. Lubashevsky, R. Mahnke, M. Hajimahmoodzadeh, and A. Katsnelson. Long-lived states of oscillator chains with dynamical traps. *Eur. Phys. J. B*, 44, 63–70, 2005.
7.I.A. Lubashevsky, P. Wagner, R. Mahnke. Rational-driver approximation car-following theory. *Phys. Rev. E*, 68, 056109, 2003.